REPORT DOCUMENTATION PAGE

Form Approved OMB No. 0704-0188

1. REPORT DATE *(DD-MM-YYYY)*
03 December 2008

2. REPORT TYPE
Master's Thesis

3. DATES COVERED *(From - To)*
3 December 2008 – 10 February 2015

4. TITLE AND SUBTITLE
COMPARISON BETWEEN PREDICTIONS AND MEASUREMENTS OF PERFORMANCE CHARACTERISTICS FOR AN EIGHT POCKET HYBRID (COMBINATION HYDROSTATIC AND HYDRODYNAMIC) THRUST BEARING

5a. CONTRACT NUMBER
FA9300-04-C-0016

5b. GRANT NUMBER

5c. PROGRAM ELEMENT NUMBER

6. AUTHOR(S)
FERNANDO A. RAMIREZ

5d. PROJECT NUMBER

5e. TASK NUMBER

5f. WORK UNIT NUMBER
Q0BY

7. PERFORMING ORGANIZATION NAME(S) AND ADDRESS(ES)

Air Force Research Laboratory (AFMC)
AFRL/RQRC
10 E. Saturn Blvd
Edwards AFB, CA 93524-7680

8. PERFORMING ORGANIZATION REPORT NO.

9. SPONSORING / MONITORING AGENCY NAME(S) AND ADDRESS(ES)

Air Force Research Laboratory (AFMC)
AFRL/RQR
5 Pollux Drive
Edwards AFB, CA 93524-7048

10. SPONSOR/MONITOR'S ACRONYM(S)

11. SPONSOR/MONITOR'S REPORT NUMBER(S)
AFRL-RQ-ED-OT-2015-039

12. DISTRIBUTION / AVAILABILITY STATEMENT
Approved for public release; distribution unlimited

13. SUPPLEMENTARY NOTES
PA Case Number: #15074; Clearance Date: #2/10/2015
This is a Master's Thesis based upon work subcontracted to Texas A&M University by Northrop Grumman under the USET contract. The work was completed in 2008 and the advisor is looking to have the thesis made publicly releasable.

14. ABSTRACT
A test rig was designed, produced, and used to test a hybrid thrust bearing geometry. The rig uses a hydraulic cylinder to load axially the rotor system supported by hybrid journal and thrust bearing supports. Two identical thrust bearings react the static axial load via two fluid films loaded against collars of the test rotor. The hybrid thrust bearing has an outer radius of 38.1 mm and an inner radius of 20.32 mm. The bearing has eight pockets spaced evenly at the mid-radius with a supply orifice located in the center of each pocket. The hybrid thrust bearing was tested at 3.45, 10.34, and 17.24 bar supply pressure with water operating at three rotor speeds of 7.5, 12.5, and 17.5 krpm. Each test thrust bearing inlet supply-pressure condition was tested with at least eight loads spanning the load range predicted by XLHydroTHRUST®. The report details XLHydroTHRUST® prediction validation against measurements of the performance characteristics of the turbulent hybrid thrust bearing. Predictions correlate reasonably well for flow rates especially for the 17.24 bar supply pressure condition. Additionally, measurements of flow rate through the inner radius of the test thrust evidences the onset of starvation (sub-ambient pressures) of the fluid film across the land for a high-speed (17.5 krpm) and low-load condition due to fluid centrifugal acceleration. Predictions correlate reasonably well for load capacity especially for higher loads (small film thickness). Also, measurements of the performance characteristics of the turbulent hybrid thrust bearing with rotor spinning were compared to those measured by Forsberg [1] without speed. The comparison between the two sets of static measurements show good agreement for test case average clearances equal and greater than the nominal clearance of 76.2 µm (low to mid loading). However, Forsberg's [1] measurements contain a wider load range testing at smaller average clearances under nominal clearance (higher loading) at without rotor spin.

15. SUBJECT TERMS

16. SECURITY CLASSIFICATION OF:			**17. LIMITATION OF ABSTRACT**	**18. NUMBER OF PAGES**	**19a. NAME OF RESPONSIBLE PERSON**
					G. Ruderman
a. REPORT	**b. ABSTRACT**	**c. THIS PAGE**	SAR	124	**19b. TELEPHONE NO** *(include area code)*
Unclassified	**Unclassified**	**Unclassified**			N/A

Standard Form 298 (Rev. 8-98)
Prescribed by ANSI Std. 239.18

COMPARISON BETWEEN PREDICTIONS AND MEASUREMENTS OF PERFORMANCE CHARACTERISTICS FOR AN EIGHT POCKET HYBRID (COMBINATION HYDROSTATIC AND HYDRODYNAMIC) THRUST BEARING

A Project Report

By

FERNANDO A. RAMIREZ

Submitted
In partial fulfillment of the requirements for the degree of

MASTER OF SCIENCE

December 3, 2008

Major Subject: Mechanical Engineering

ABSTRACT

Comparison between Predictions and Measurements of Performance Characteristics for an Eight Pocket Hybrid (combination Hydrostatic and Hydrodynamic) Thrust Bearing
(December 2008)
Fernando A. Ramirez, B.S.M.E., University of Texas at Austin
Chair of Advisory Committee: Dr. Dara Childs

A test rig was designed, produced, and used to test a hybrid thrust bearing geometry. The rig uses a hydraulic cylinder to load axially the rotor system supported by hybrid journal and thrust bearing supports. Two identical thrust bearings react the static axial load via two fluid films loaded against collars of the test rotor. The hybrid thrust bearing has an outer radius of 38.1 mm and an inner radius of 20.32 mm. The bearing has eight pockets spaced evenly at the mid-radius with a supply orifice located in the center of each pocket. The hybrid thrust bearing was tested at 3.45, 10.34, and 17.24 bar supply pressure with water operating at three rotor speeds of 7.5, 12.5, and 17.5 krpm. Each test thrust bearing inlet supply-pressure condition was tested with at least eight loads spanning the load range predicted by XLHydroTHRUST®.

The report details XLHydroTHRUST® prediction validation against measurements of the performance characteristics of the turbulent hybrid thrust bearing. Predictions correlate reasonably well for flow rates especially for the 17.24 bar supply pressure condition. Additionally, measurements of flow rate through the inner radius of the test thrust evidences the onset of starvation (sub-ambient pressures) of the fluid film across the land for a high-speed (17.5 krpm) and low-load condition due to fluid centrifugal acceleration. Predictions correlate reasonably well for load capacity especially for higher loads (small film thickness).

Also, measurements of the performance characteristics of the turbulent hybrid thrust bearing with rotor spinning were compared to those measured by Forsberg [1] without speed. The comparison between the two sets of static measurements show good

agreement for test case average clearances equal and greater than the nominal clearance of 76.2 μm (low to mid loading). However, Forsberg's [1] measurements contain a wider load range testing at smaller average clearances under nominal clearance (higher loading) at without rotor spin.

ACKNOWLEDGEMENT

The supervision, direction, and continuing support through my graduate research and studies have been bestowed to me by my advisor, Dr. Childs. I am grateful to him. Mike Forsberg, Paul Esser, and Scott Wilson saw me through everything described in this report. I am grateful to them, as well. I would finally like to thank Mr. Steve Phillips, Mr. Eddie Denk, and Mr. Adolfo Delgado to whom I imposed on regularly for assistance.

TABLE OF CONTENTS

LIST OF FIGURES

LIST OF TABLES

NOMENCLATURE

A_0	Area of inlet orifice (m^2), see Eq. (5)
C_d	Orifice discharge coefficient
$D_{Orifice}$	Diameter of orifice (m)
E_N	Error associated with term "N"
F	Static load on bearing face
M_1	TTB misalignment in the x direction $\left(\mathrm{mm}/\mathrm{mm}\right)$
M_2	TTB misalignment in the y direction $\left(\mathrm{mm}/\mathrm{mm}\right)$
M_{1slave}	STB misalignment in the x direction $\left(\mathrm{mm}/\mathrm{mm}\right)$
M_{2slave}	STB misalignment in the y direction $\left(\mathrm{mm}/\mathrm{mm}\right)$
$P_{Atmospheric}$	Atmospheric pressure
$P_{Exhaust}$	Pressure bearing exhausts into
P_{Pocket}	Pocket pressure
P_{Ratio}	Pressure ratio
P_R	Recess (pocket) pressure (Pa)
P_{Supply}	Supply pressure
P_S	Supply pressure (Pa)
R_{out}	Outer radius of thrust bearing (m)
$\mathrm{Re}_{CircFlow}$	Circumferential flow Reynolds number
$\mathrm{Re}_{Orifice}$	Orifice Reynolds number
$\mathrm{Re}_{OuterRadius}$	Outer radius Reynolds number
$V_{Orifice}$	Fluid velocity through orifice $\left(\mathrm{m}/\mathrm{s}\right)$
$V_{OuterRadius}$	Fluid velocity through thrust bearing outer radius $\left(\mathrm{m}/\mathrm{s}\right)$
Z_a	Gap reading from proximity probe "a"
Z, Z_c	Center clearance of TTB (m) and (mm), respectively
Z_{cslave}	Center clearance of STB (mm)
μ	Dynamic viscosity $\left(\mathrm{N{*}s}/\mathrm{m}^3\right)$
ρ	Working fluid density $\left(\mathrm{kg}/\mathrm{m}^3\right)$
Ω	Rotational shaft speed $\left(\mathrm{rad}/\mathrm{s}\right)$

Acronyms:

STB	Slave thrust bearing
TTB	Test thrust bearing
TAT	Tilt alignment testing

INTRODUCTION

Hybrid (combination hydrostatic and hydrodynamic) thrust bearings are important components for potential use in high speed rotors for cryogenic turbomachinery. Fluid film hybrid thrust bearings, proposed for cryogen lubricated turbopump retrofits, are primarily of multi-recess and orifice compensated design [2]. The hydrodynamic fluid films of a thrust bearing set provide axial support of expected large thrust. The hybrid thrust bearing offer the advantages of durability, no bearing DN life limitations, low friction, and wear [3]. Similar to the performance of hybrid radial support bearings in a rotor assembly, the hybrid thrust bearing sustains the dynamic axial stability of the rotor-bearing system with large direct stiffness and damping force coefficients. Figure 1 shows the thrust bearing geometry of a typical annular eight-pocket design.

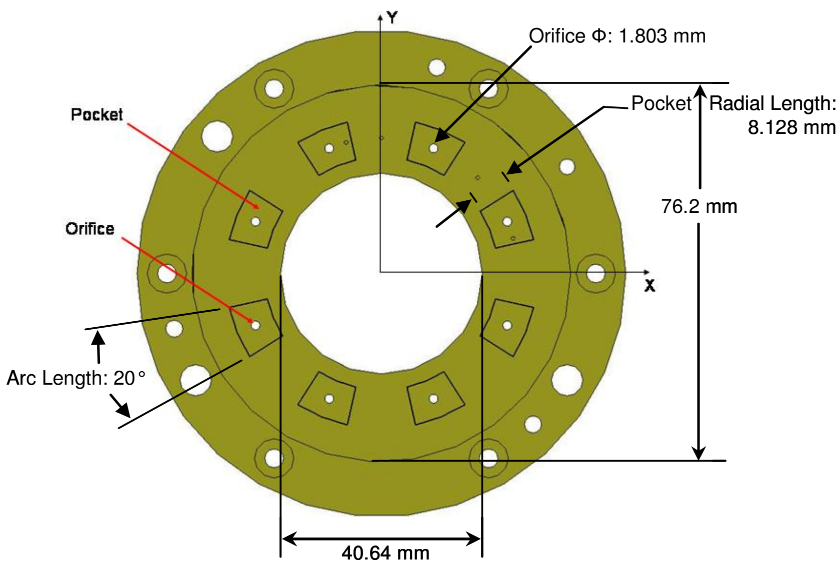

Figure 1: Front view of test thrust bearing

In hybrid thrust bearings, hydrostatic effects enable a large load capacity relying on viscous and hydrostatic effects to generate reaction forces. The bearing fluid is supplied into a pocket through an orifice or capillary feed. The fluid then flows to the sides through the lands and exits to an ambient pressure. The resulting high pressure over the bearing surface provides the necessary force to react an axial load. Viscous effects develop a pressure rise proportional to the shaft rotational speed (Ω). The bearing may

also be activated with fluid inertial effects providing load capacity at high speed operation [4]. Fluid is dragged into the film and hydrodynamic pressures are generated proportional to Ω^2. Inertia effects are developed by a pressure drop at sudden changes in film clearance at the inlet and discharge sections of the bearing pad length [5]. Hence, the viscous and inertial phenomena both contribute to the overall static and dynamic coefficients of the hybrid thrust bearing. Lastly, classical theory of lubrication asserts that a slider bearing configuration with parallel surfaces is not able to support a load. Some low misalignment of the thrust bearing face is important in generating hydrodynamic pressures.

Hybrid bearings are being considered for liquid rocket engine turbopumps. The performance of this type of bearing depends upon the size of the film lands and pockets, fluid properties, fluid inlets, clearance, and most importantly the supply pressure. Also, measuring force coefficients and other performance characteristics (such as load capacity, film thickness, leakage rates, and power loss) of the bearing is necessary to validate San Andrés analysis [6] for application into cryogenic fluid hybrid thrust bearings. Therefore, this report provides an experimental investigation of the performance of an eight-pocket fixed geometry thrust bearing serving as a benchmark for calibration of the XLHydroTHRUST® analytical tool.

San Andrés [3] presents a model for predicting hybrid thrust bearing performance that includes fluid inertia, flow turbulence, and fluid compressibility. This model uses the bulk-flow model that relates shear at the surfaces of the bearing to the average fluid-flow velocities relative to the walls. Flow equations are presented for the film lands and recesses (pockets) with the conditions calculated at the edge of the pockets providing boundary conditions for the lands equation. A first-order perturbation is implemented to calculate the bearing force coefficients. The zeroth order equations are solved using a control volume scheme. Numerical results are then provided for a hybrid bearing system. Discussions on this model are expanded in San Andrés [6] where effects of collar misalignment are discussed and predicted to noticeably affect flow rate, axial stiffness, and axial damping coefficients. San Andrés addresses theoretical and practical issues of

the performance of a hybrid thrust bearing such as turbulent flow operation dominated by inertial effects on the bearing pocket and lands, misalignment effects, and centrifugal forces at high speeds and pressures. These physical aspects, paramount to the performance of the turbulent thrust bearing, lead the development and testing of the hybrid thrust bearing test rig. The following review of technical publications also relate to the thrust bearing experimental investigation, detailing the most relevant findings.

A REVIEW OF PRIOR THRUST-BEARING TEST RIGS

An early experimental study for hydrostatic thrust bearings and comparison to predictions was presented by Elwell and Sternlight [7] for two types of circular hydrostatic thrust bearings, using incompressible lubricants. Tests produced operating characteristics of two test bearings (step and annular type, shown in Figure 2) for an array of restrictions (i.e., capillary, orifice, and constant-flow control) of flow rates, load capacity, film thickness, and stiffness. Good experimental verification was obtained for the design equations. The flow rate decreases linearly with the loading for the capillary restriction since the flow velocity is proportional to ΔP across the restriction. While the orifice restriction flow rate shows a decrease with the load, proportional to $\sqrt{\Delta P}$. Finally, the load capacity and stiffness for the step bearing, with capillary and orifice restrictors, achieve a maximum threshold load (which is a function of the supply pressure) where the bearing will no longer support the rotor. This behavior is confirmed by the stiffness which reaches a maximum for a certain clearance and then drops off with decreasing clearance. The bearing with constant flow restriction shows a greater load capacity while the pressure is available to maintain the flow, leading this configuration to have the highest stiffness of the three restrictors.

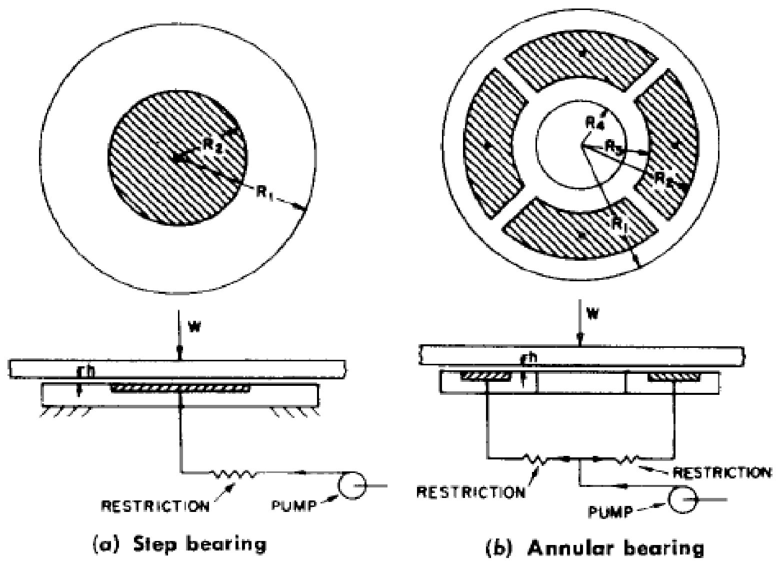

Figure 2: Hydrostatic bearings used by Elwell and Sternlight [7]

Some researchers have studied the effects of centrifugal fluid inertia on the performance of hydrodynamic thrust bearings including Pinkus and Lund [8], Hashimoto [9], and San Andrés [6]. Safar [10] studied the centrifugal effects in a misaligned hydrostatic thrust bearing. Considering the effects of tilt, and modified Reynolds number on the pressure distribution, load capacity, friction torque, and flow rate, the author solves the Reynolds equation containing the effects of centrifugal acceleration in the fluid film. A significant insight on results of pressure distribution in the radial and circumference direction for parallel or tilted bearings is that centrifugal acceleration produce subambient pressure causing a reduction in load capacity, and increase in lubricant flow rate. Safar also found, that as tilt increases, the effect of the centrifugal forces decrease. Also, the thrust bearing performance characteristics are increased with tilt. Additionally, Dowson [11] conducted a similar study of the inertial effects of a thrust bearing, and shows that centrifugal acceleration terms have a significant influence on the prediction of bearing performance and should be retained in the equations of motion.

Forsberg [1] provides a summary of relevant papers pertaining to the design of a thrust bearing test facilities. These test rigs fall into two categories: (1) single thrust

bearing test rigs where the load is applied by moving the rotor to apply load to a stationary thrust bearing, and (2) multiple-thrust-bearing test rigs where load is applied through a thrust bearing and transmitted to a separate thrust bearing where the load is reacted. New [12] describes a multiple-thrust-bearing test rig for use in testing hydrodynamic thrust bearings, see Figure 3.

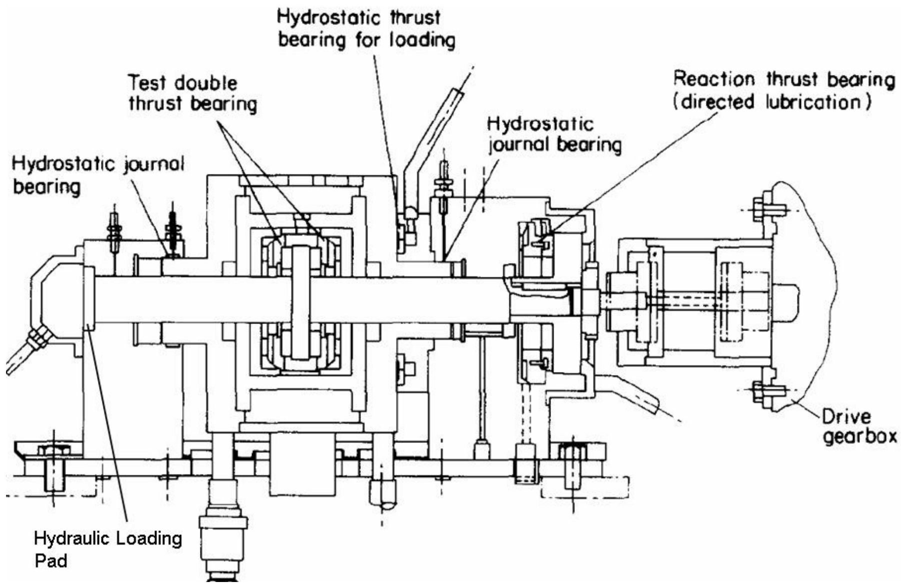

Figure 3: Orion high speed test rig, New [12]

In this test rig the load is applied to the housing containing the test thrust bearing with a hydrostatic thrust bearing. The test thrust bearing then transmits the load through the rotor, which is supported on a pair of hydrostatic journal bearings, where it is reacted with a hydraulic loading pad. The load is then measured with the hydraulic loading system. To measure the torque exerted on the thrust bearings, as well as to allow free axial movement for loading, the housing containing the thrust bearings is mounted on hydrostatic bearings. This design allows the housing to rotate freely to load a spring balance, which measures the torque. Additionally, the test bearings are instrumented to measure the clearance and temperatures while flow rates are measured outside of the test rig. Gregory [13], Neal [14], and Horner et al. [15] describe similar test rigs.

Harada et al. [16] uses the multiple thrust bearing test rig in Figure 4.

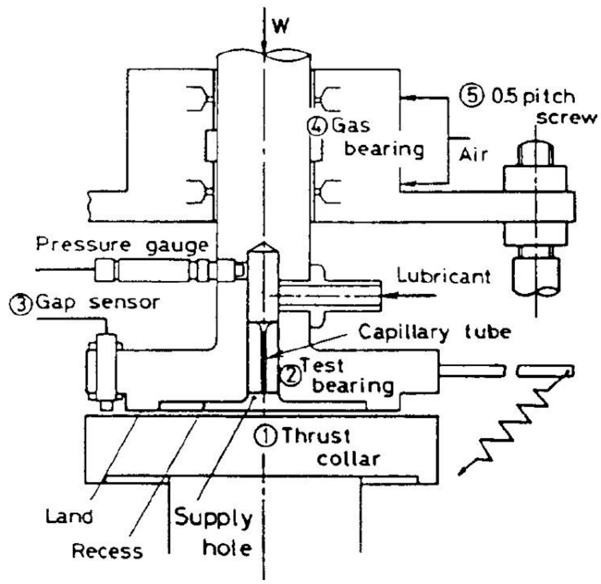

Figure 4: Harada test rig for hydrostatic thrust bearing testing [16]

The Harada test rig uses a piston floated on gas bearings to support and load the test thrust bearing. This load is then transmitted through the rotor to a set of ball bearings which react it. The thrust bearing clearance is measured by three eddy current proximity probes located 120^{o} from each other, which provides more detailed information about the clearance profile. Finally, temperature is measured at the inlet and outlet, and flow rate is measured into the bearing. They found that fluid flow in transition to turbulence on the land yields a decrease in flow rate causing the load capacity to increase. The shaft rotational speed influences the load capacity less in the turbulent regime than in the laminar regime. Furthermore, the thrust bearing clearance in the turbulent regime is larger than in the laminar regime.

Glavatskih [17] describes a rig for testing double thrust bearings, as shown in Figure 5.

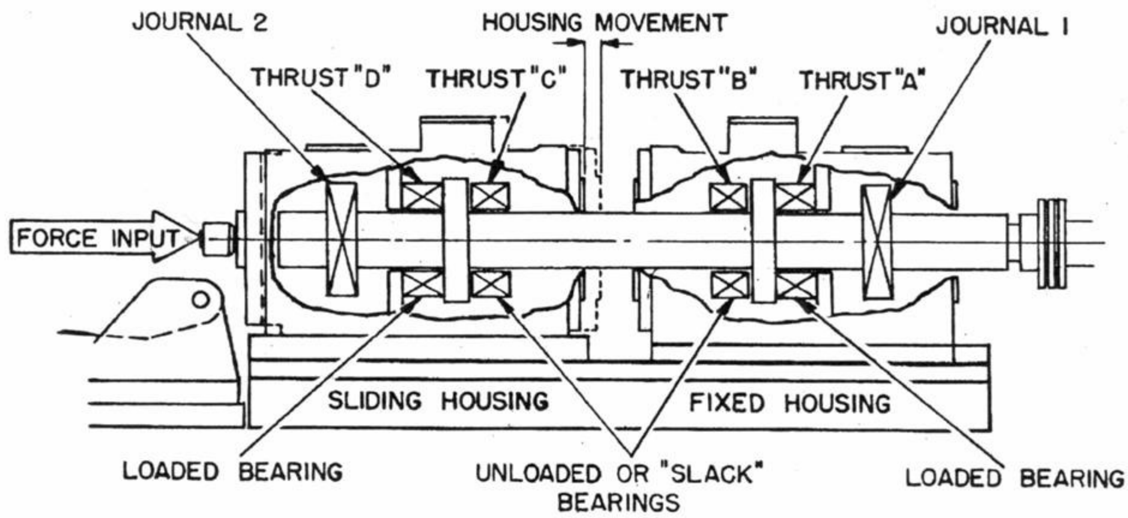

Figure 5: Test rig used for testing of double hydrodynamic thrust bearings [17]

The test rig has two similar sections each containing a thrust bearing set and a journal bearing. One section is allowed to move freely in the axial direction to apply load to the rotor. The other section is secured and reacts the applied force from the sliding section. They tested a tilting pad thrust bearing, best quantified in terms of developed power loss, operating temperature and oil film thickness.

TEST RIG DESCRIPTION

A test rig was constructed to study the performance characteristics of a hybrid (hydrostatic and hydrodynamic) thrust bearing. Figure 6 shows the final assembled test thrust bearing configuration. The rotor rotation is supported by two hybrid flexure tilt pad journal bearings. The face-to-face thrust bearing configuration, which provides axial support of the test rotor, has the following two sections: the hydraulic cylinder load end, and motor drive end. The hydraulic cylinder load end consists of the stinger connecting the hydraulic cylinder to the test thrust bearing and load shaft, affixed rigidly to the air bearing mount. The motor drive end consists of the slave thrust bearing, facing the opposing rotor collar side, and connected to the electric motor through the FLEXXOR© coupling. The following discussion includes details on the predominant components of the test rig.

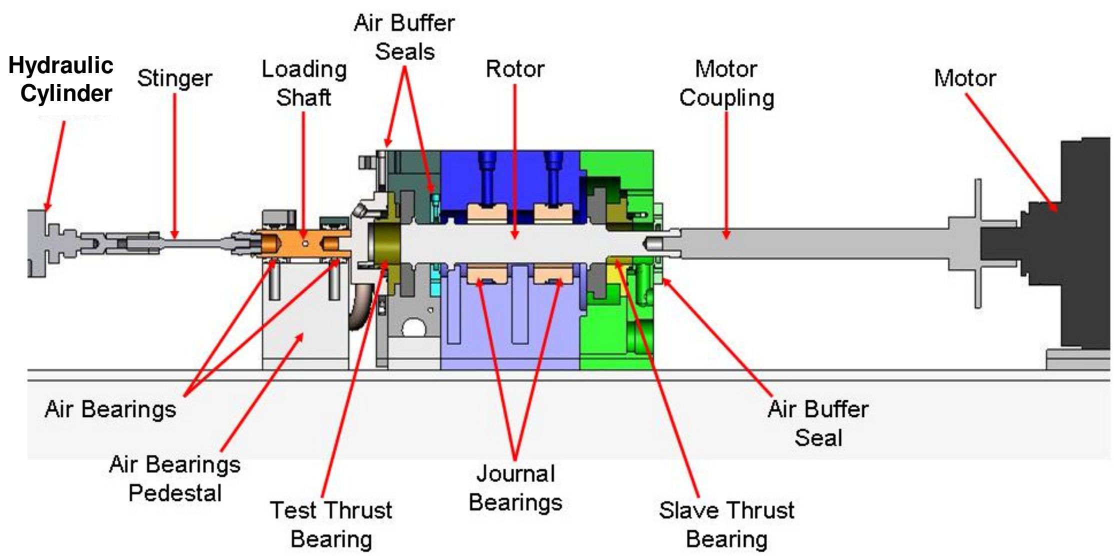

Figure 6: Schematic of hybrid thrust bearing test rig, designed configuration [1]

TEST THRUST BEARING

The test thrust bearing (TTB) section of the test rig is isolated from the other bearings by an air buffer seal to enable measurement of the TTB exhaust flow without in-flow from the other bearing exhaust flow, as shown in Figure 7.

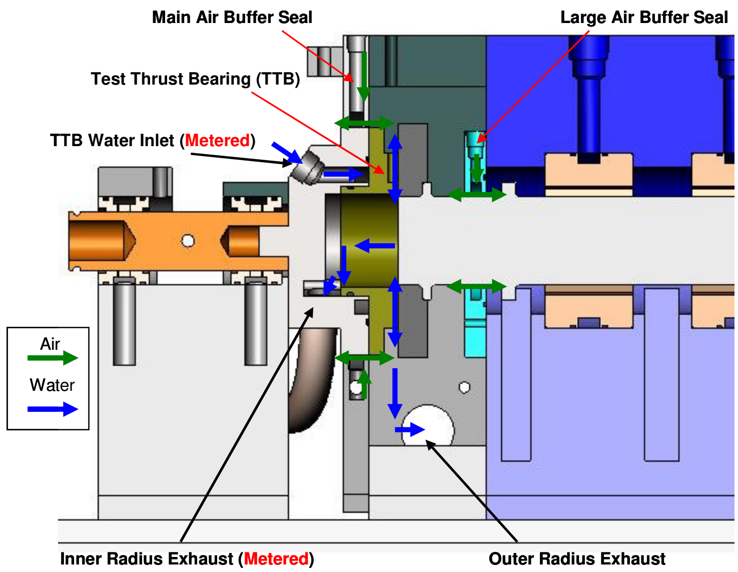

Figure 7: TTB and TTB air seal flow path

The pressure actuation of the TTB is depicted by the water flow path (blue arrow indicators) in the figure. The water enters a port/groove system that directs flow through inlet orifices into the eight bearing pockets. The water is discharged radially from the inner and outer radius of the TTB exiting through the bearing film lands. The bearing film lands provide a circular-disk flow path composed of the bearing and thrust collar face. The combination of flow resistance (hydrostatic) effects through the orifice restrictors and shear flow (hydrodynamic) effects within the bearing film lands develop the TTB load capacity [18]. TTB flow control was established via a pneumatic control valve.

Turbine flow meters monitor the inlet flow and inner radius discharge flow of the test thrust bearing depicted in Figure 7. Three thermocouples are utilized to measure temperature of the upstream inlet flow, inner-radius discharge flow, and outer-radius discharge flow of the test thrust bearing. A detailed description of the full array of instrumentation and calibration procedures of this experimental test rig is provided from Forsberg [1] in Appendix D.

Figure 7 also depicts the TTB housing containing the large air buffer seal and exit/entry ports. The large air buffer seal around the test rotor shaft prevents axial

leakage into the test thrust bearing housing from the journal bearings. Furthermore, the main air seal prevents leakage from around the outer diameter edge of the test thrust bearing support.

Additionally, the test thrust bearing is free to translate (due to axial loading), and rotate due to torque effects of viscous shear acting on the bearing face. The rotation of the test bearing is limited by a torque arm, which contains a load cell for torque measurement.

Thrust collars on the drive end and free end of the rotor are depicted in Figure 8. Figure 8 shows the geometry of the test rotor composed of drive end collar, free end collar, and rotor shaft.

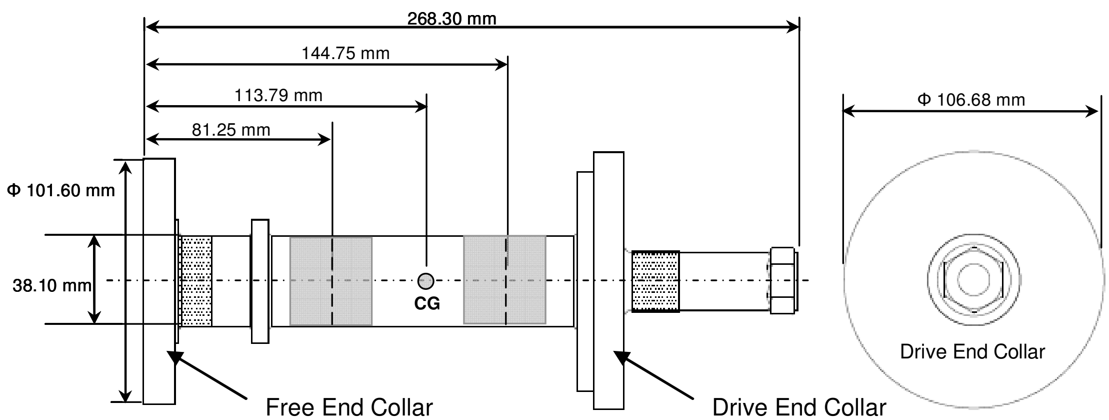

Figure 8: Geometry of test rotor (3.88 kg)

The thrust bearing geometry shown in Figure 1 is typical for an eight-pocket design. This annular bearing design consists of a central bore for passage of a shaft or drainage of discharge fluid. Annular pockets divided into a number of segmental pockets and land regions make up the bearing face. The thrust bearings have an outer diameter of 76.2 mm (3 in) and an inner diameter of 40.64 mm (1.6 in.) as shown in Figure 1.

The test thrust bearing features a single annular disk design. Also, the bearing is designed to mount in the thrust bearing support of the test rig. The test thrust bearing characteristics are given in Table 1.

Table 1: Dimensions of test thrust bearing

Parameters	***SI Units***	***English Units***
Bearing inner diameter	40.64 mm	1.60 in
Bearing outer diameter	76.2 mm	3.00 in
Number of pockets	*8, Equally spaced*	
Pocket arc length	0.349 rad	20°
Pocket inner radius	23.47 mm	0.924 in
Pocket outer radius	31.47 mm	1.239 in
Pocket depth	5.08 mm	0.020 in
Orifice location	*Location at mid-radius and mid-arc of pocket*	
Orifice diameter	1.80 mm	0.071 in

The TTB is fully instrumented, for static measurements, with fluid film thickness, pressure, flow, and thermocouple sensors. Three eddy-current proximity probes are rigidly attached to the TTB measuring the distance to the thrust collar face. Five pressure sensors are used to measure inlet supply pressure, two pocket pressures, and two land pressures. Also, these pressure transducers are not flush mounted and only measure static pressure. Figure 9 shows the pocket and land tap positions set on the first quadrant of the bearing face to avoid the target areas of the proximity probes.

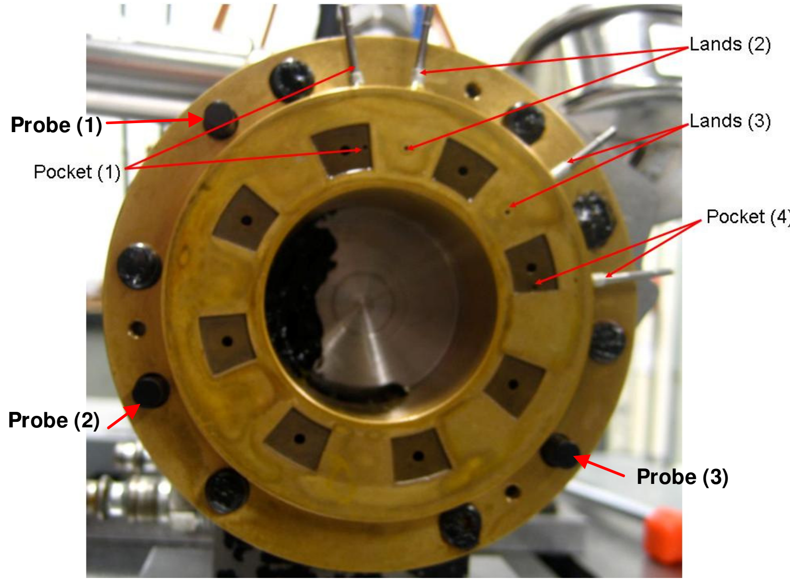

Figure 9: Location of pressure taps and proximity probes for bearing pressure measurement [1]

The TTB incorporates the air bearing support section shown in Figure 6. TTB is rigidly supported by the axial loading shaft. The axial shaft is supported on the air bearing pedestal mount by two air bearing, supplied with filtered 10.34 bar (shop) air. The air bearings allow axial translation of the test thrust bearing with little friction; also providing tilt resistance of the vertical face of the bearing. In addition, pitch and yaw adjustments of the air bearing pedestal mount are undertaken to achieve relative parallelism between the bearing face and collar. Figure 10 shows the tilt adjustment bracket and micrometer screw used to make adjustment about the vertical axis of the test thrust bearing face. Adjustment about the horizontal axis is made using a shim set either at the front of the air bearing pedestal and/or back of the adjustment assembly along the axial length.

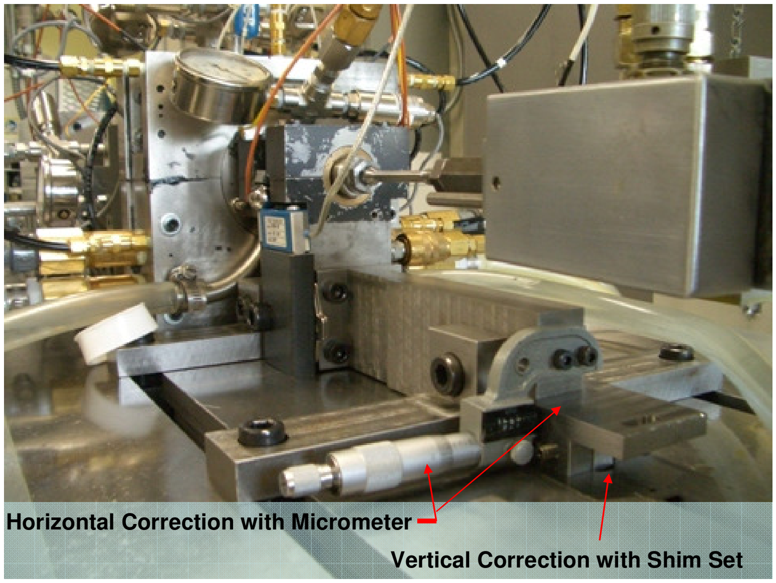

Figure 10: View of the air bearing pedestal tilt adjustment bracket

WATER LUBRICATED RADIAL JOURNAL BEARINGS

The hybrid radial bearings are flexure pivot-tilting pad designs oriented with load between pads. A pad is supported by a beam element "web", which has sufficiently low rotational stiffness to provide load support of the test rotor in the radial direction resulting in high stability (low cross-coupled stiffness) [19]. The journal bearings provide radial support of the rotor and are mounted with interference fits within the journal bearing housing shown in Figure 11. The influence of the hybrid journal bearings on the thrust bearing is minimized by low eccentricity (center position) at a high inlet pressure of approximately 17.24 bar and increases to 20.68 bar due to rotation. The water supply pressure is controlled through the inlet ports to the recess of the four tilt pads of the journal bearing using a pneumatically actuated control valve. The water travels from a radial annulus to each recess through an orifice restrictor of the journal bearings. The journal bearings are instrumented with pressure and flow sensors. A pair of pressure sensors measures inlet supply pressures into each bearing. A turbine flow meter measures the combined total inlet flow into the two journal bearings. Again, further details of the description of the full array of instrumentation and calibration procedures of this experimental test rig are provided from Forsberg [1] in Appendix D.

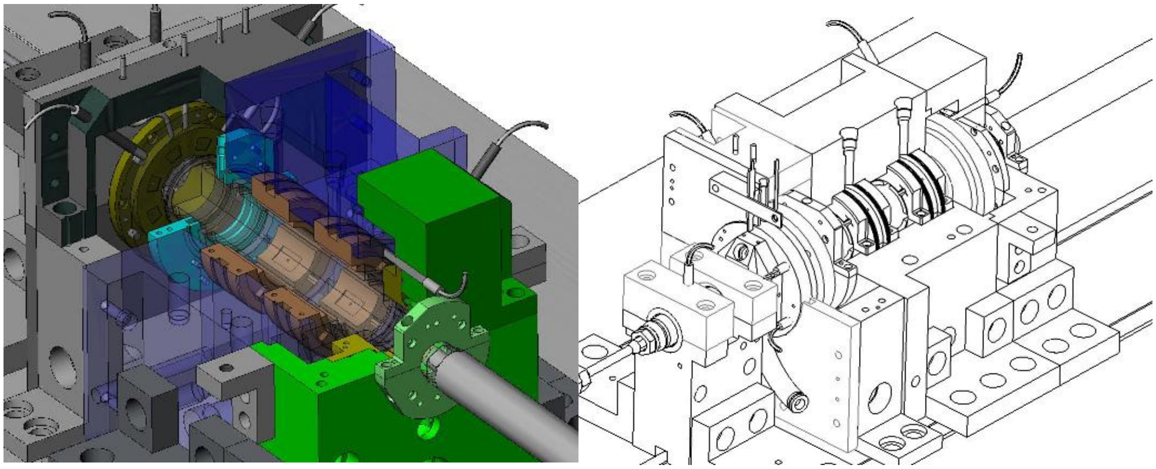

Figure 11: Diametric view (90 degree cross-section) of the test thrust bearing rig. From left to right are the test thrust bearing, large air buffer seal, two journal bearings, slave thrust bearing, and small air buffer seal.

The test rotor is contained within the journal bearing housing, and is made of 718 Inconel for its properties of high temperature strength and corrosion resistance. Table 2 shows the geometry and inertial properties of the test rotor. The test shaft may be driven up to 30,600 rpm using an adjustable frequency AC drive. The radial position of the test rotor is monitored using two pairs of radial eddy current proximity probes positioned orthogonally on the thrust collars.

Table 2: Summary of test rotor geometry characteristics and inertial properties

Parameters	*SI Unit*	*Measured Value*	*Uncertainty (±)*
Modulus of elasticity	$208x10^3$ Mpa		
Material density	8220 kg/m^3		
Total mass		3.88 kg	$2.27x10^{-3}$ kg
Diameter of shaft at bearing locations		38.10 mm	1.27e-2 mm
Total length		268.30 mm	"
Distance between the rotor CG to the free end		113.79 mm	"
Distance between journal bearing 1 to the free end		81.25 mm	"
Distance between journal bearing 2 to the free end		144.75 mm	"
Diameter of free end thrust collar		101.60 mm	"
Diameter of drive end thrust collar		106.68 mm	"
Transverse moment of inertia		254.74 $kg\text{-}cm^2$	3.80 $kg\text{-}cm^2$
Polar moment of inertia		25.58 $kg\text{-}cm^2$	1.23 $kg\text{-}cm^2$

SLAVE THRUST BEARING SECTION

The slave thrust bearing (STB) parameters are identical to the test thrust bearing (TTB) parameters listed in Table 1. The STB features a different flange of greater axial thickness due to a split design shown in Figure 11. The bearing is directly mounted to the STB stainless steel housing.

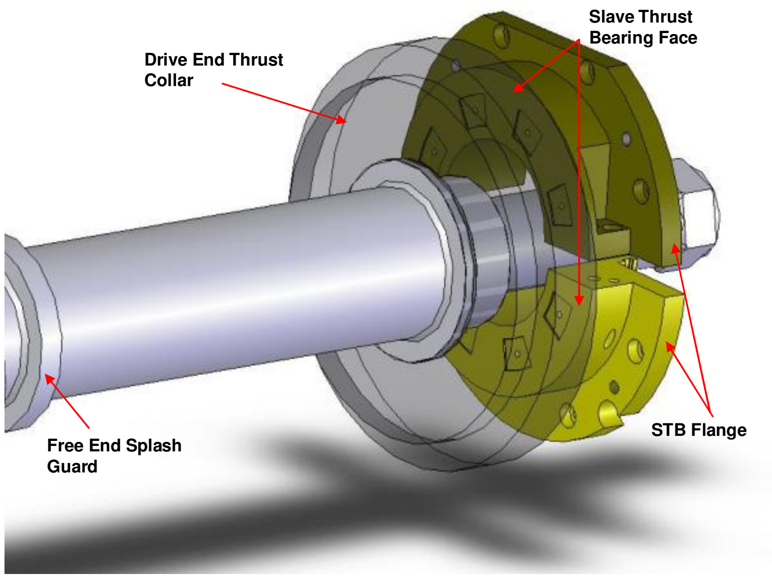

Figure 12: Exploded view of slave thrust bearing (depicted split) and drive end thrust collar (depicted transparent) on the rotor shaft

The STB housing provides rigid attachment of three eddy current proximity probes for measurement of axial clearance change between the collar and face. Also, the housing consists of inlet ports to provide pressurization of the STB. An air buffer seal is rigidly attached to the external side of the bearing housing to prevent inner radius discharge of the STB from leaking out around the circumferential surface of the drive shaft. Specifically, the STB housing functions as a container to collect leakage from the journal bearing axial discharge, and from the STB outer and inner radii discharge. Discharge ports allow for re-circulation to the water tank.

AXIAL DRIVELINE AND LOAD PATH

The entire driveline is oriented axially, as shown in Figure 13, on a test stand specified to a surface finish flatness of 5.08 µm. A hydraulic cylinder applies axial static loads via a stinger to the thrust bearing. The stinger isolates the test structure from the dynamics of the hydraulic cylinder [20]. The applied static load is reacted though the test rotor by the STB. The static load applied to the TTB is measured with a load cell connecting the stinger to the hydraulic cylinder head. The motor and coupling hardly develop a reaction force in the axial direction due to the softness of the FLEXXOR© coupling and quill shaft unit.

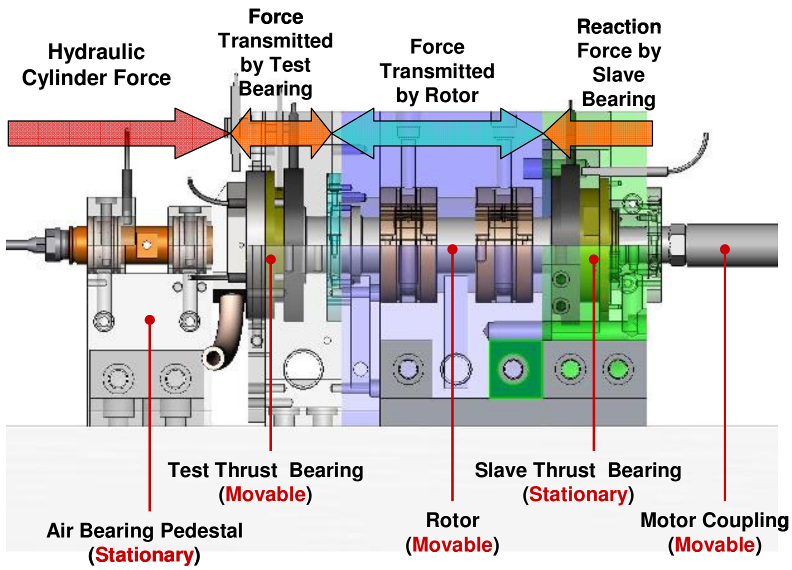

Figure 13: Static configuration load path

As shown in Figure 6, the drive end section includes an electric motor that turns the test rotor attached by a coupling that allows axial displacement of ±0.635 mm (25 mils). An infra-red tachometer is oriented on the coupling quill shaft for rotational speed measurement. The test rotor extends through the inner bore of the slave thrust bearing within the slave thrust bearing housing.

PROCEDURE OF TESTING THRUST BEARING WITH ROTOR SPINNING

The following sections include the basic test procedure for testing the hybrid thrust bearing test rig. The test matrix includes the supply pressure of the thrust bearing range at 3.45, 10.34, and 17.24 bar. For each supply pressure, static measurements are taken at three speeds (7.5, 12.5, and 17.5 krpm) and eight to ten clearances (over a certain load range) for a total of 86 test conditions.

ALIGNMENT CORRECTION

Before a typical test, a tilt assessment test (TAT) is conducted to achieve baseline measurements of axial clearance and assess the misalignment of the test and slave thrust bearing between their respective thrust collars. Baseline measurements consist of measuring axial distance between the sensor and thrust collar face (for each of the six proximity probes) when the thrust bearings are pressed against the collars. Baseline readings are taken for the five static loads of 0.33, 0.56, 0.78, 1, and 1.22 kN without counteraction of the thrust bearings (inlet supply pressure at 0 bar). The applied static load is reacted to ground via the rigidly fixed STB housing. Axial load is imparted using internal force control of the hydraulic cylinder. Also, the supply pressure into the journal bearings is held at 17.24 bar to keep the shaft positions centered during subsequent rotation testing. The minimum displacement for each sensor measured from the five load tests is deemed the calibration offset value for all subsequent axial clearance measurements.

A TAT is concluded by the measurement of five test conditions over the low-load capacity range with thrust bearings pressurized at 3.45 or 10.24 bar at zero rotational speed. Axial clearance measurements from the three proximity probes on each thrust bearing may be used to evaluate the misalignment slopes about the x and y axis of the thrust bearing faces relative to the respective thrust collars. For the test thrust bearing, the formula for the misalignment slope in the horizontal x direction (M_1) is shown in Eq.

(1.1), and the misalignment slope in the vertical *y* direction (*M_2*) is shown in Eq. (1.2). The derivation for the misalignment slopes of the test thrust bearing is presented by Forsberg [1], and can be found in Appendix E.

$$M_1 = 0.0134(Z_3 - Z_2) \quad \textbf{(1.1)}$$

$$M_2 = (0.0203Z_1 - 0.0191Z_2 - 0.00118Z_3) \quad \textbf{(1.2)}$$

where

$M_1 =$ TTB Misalignment in the x direction $\left(\mathrm{mm}/\mathrm{mm}\right)$

$M_2 =$ TTB Misalignment in the y direction $\left(\mathrm{mm}/\mathrm{mm}\right)$

$Z_1, Z_2, Z_3 =$ Gap readings from probe 1,2, or 3 of the TTB (mm)

In regards to the STB, the formula for the misalignment slope in the horizontal *x* direction (*M_{1slave}*) is shown in Eq. (1.3), and the misalignment slope in the vertical *y* direction (*M_{2slave}*) is shown in Eq. (1.4). The derivation for the misalignment slopes of the STB are found in Appendix F.

$$M_{1slave} = 0.0153(Z_9 - Z_{10}) \quad \textbf{(1.3)}$$

$$M_{2slave} = (0.0117Z_4 - 0.00585Z_{10} - 0.00585Z_9) \quad \textbf{(1.4)}$$

where

$M_{1slave} =$ STB Misalignment in the x direction $\left(\mathrm{mm}/\mathrm{mm}\right)$

$M_{2slave} =$ STB Misalignment in the y direction $\left(\mathrm{mm}/\mathrm{mm}\right)$

$Z_4, Z_9, Z_{10} =$ Gap readings from probe 4,9, or 10 of the STB (mm)

The tilt adjustment bracket on the air bearing pedestal is employed to align the TTB to relative parallelism to the thrust collar, as shown on Figure 10, prior to a TAT. The alignment jig is an effective lever arm to provide prescribed translation of the air bearing pedestal rotated about its pivot keyway located at its front end centerline. Misalignment of the test thrust bearing may be corrected in two directions from the

combination of the following features of the alignment jig: (1) about the vertical axis of the bearing face via a micrometer screw accurate to 2.54 μm, and (2) about the horizontal axis via a shim set placed at rear end of the tilt adjustment bracket. The micrometer correction is determined by using the assessed misalignment about the vertical axis times 282.19±0.03 mm (the length from the micrometer to the air bearing pedestal pivot). The shim-set correction is determined by using the assessed misalignment about the horizontal axis times 307.59±0.03 mm (the length of the adjustment bracket and air bearing pedestal).

Another TAT is performed to verify the prescribed correction to the TTB. The TAT procedure may be repeated to reduce misalignment of the TTB face relative to the thrust collar to approximately 0.013 mm in both the x and y directions. According to Forsberg's test procedure [1], misalignment corrections were made prior and during testing of a thrust bearing supply pressure case at zero rpm rotational speed. Here, the misalignment corrections are only made prior to testing a series of loads within the load capacity of a supply pressure test condition with rotor spinning.

The STB single-plane misalignment about the x axis was corrected once by adding the minimal shim set thickness of 50.8 μm between the interface of the back of the bearing and the STB housing. Only one correction was necessary due to the low tolerance stack up of the bearing directly attached to the housing of the test rig.

BASIC TEST PROCEDURE

Preparation of the test sequence for a test thrust bearing supply pressure case at 3.45, 10.34, or 17.24 bars is as follows. The hydraulic cylinder control is set to displacement control. One of the three axial proximity probes on the TTB is used as a feedback sensor to artificially hold clearance during a pressure case test (the static load fluctuates ±10 N to hold the displacement set point). Displacement control (versus load control) is necessary to avoid possible collapse of the thrust bearings' fluid film at high load testing.

Journal bearings pressures are initially set to 17.24 bar, and thrust bearings inlet pressures are held to the pressure case constant. Via the hydraulic cylinder controller, the displacement set point is adjusted to a relatively large clearance (152.4 μm) where recess pressure ratios of the TTB, $P_{Ratio} = (P_{Pocket} - P_{Exhaust}) / (P_{Supply} - P_{Atmospheric})$, initiate at approximately 0.1 to ensure reacted loading of the thrust bearings. The rotational speed is then increased to a set constant speed. At this speed, the test and slave thrust bearing inlet supply pressures are adjusted to a specified constant inlet pressure. The displacement is incrementally decreased to the minimum at clearance of 50.8 μm. Ten load conditions are recorded over the displacement range at constant speed. A data capture of all sensors' analog outputs to the DAQ system are taken at a sampling rate of 30 Hz of 15 readings for each test condition at equilibrium.

Static data are displayed in real-time on a Labview virtual instrument, including the minimum and average clearance of the three proximity probes on the TTB using a single PCI-6225 DAQ board. Instantaneous measurements of all sensor measurements such as supply pressures, pocket pressure, flow rates, and center clearance of the two thrust bearings are displayed. Figure 14 shows the virtual display. Table 3 contains a summary of the specification for the static DAQ board.

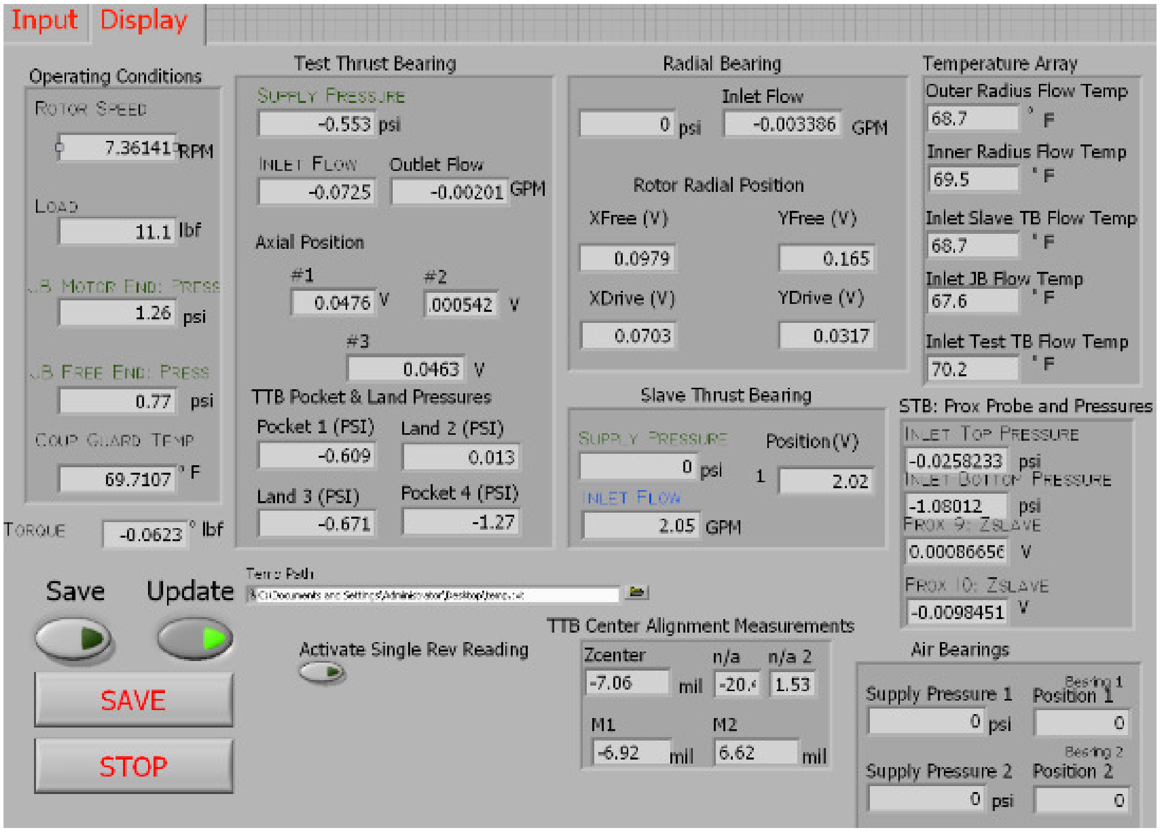

Figure 14: Real-time diagnostic Labview VI for static data logging

Table 3: Listing of DAQ board specifications [21]

Board Type	Number of Channels	Sampling Rate (Ksamples/sec)	Resolution (bits)	Signal Range (V)	Signal Type	Connection
PCI-6225	80	250 /no. of inputs	16	±10	Analog/Digital Input/Output Analog Input used	2 Pole wire through SCB-68 Connector Block

See Appendix B. for additional detail on the specification of transducers and other instrumentation.

TEST RESULTS OF THRUST BEARING PERFORMANCE

The main parameters of interest are flow rate, load capacity versus film thickness, static thrust bearing stiffness, and estimation of power loss. All test results are a function of fluid properties, supply pressure and operating speed. The following sections compare the behavior of the test thrust bearing for operation with three supply pressures.

Comparison between measured results and XLHydroTHRUST® predictions of the parameters of interest are also presented. Before proceeding, recall the principle trend for thrust bearing is: as applied load increases, the bearing operating clearance and flow rate decrease while the recess pressures increase [22]. When making comparisons between measured and predicted results, reference will be made to various operating conditions. To simplify the ensuing discussion, small center clearances of test and slave thrust bearing (Z_c and Z_{cslave}, respectively) are invariably related to large axial loads, and, vice versa.

Input for the analysis in XLHydroTHRUST® includes the bearing geometry (diameters, axial clearance, relative surface roughness, number of recesses, pad and recess dimensions, and orifice diameter), collar rotational speed, static misalignment, fluid properties, fluid temperature, fluid supply and exit pressures, recess edge and entrance loss coefficients, and solution convergence factors (iteration limits, relaxation factors). XLHydroTHRUST® requires an orifice discharge coefficient to model the pressure drop from supply pressure to pocket pressure. Equation (1.5) shows the orifice discharge coefficient calculation for flow through an orifice [6].

$$C_d = \frac{Q_0}{A_0\sqrt{\frac{2}{\rho}(P_S - P_R)}} \tag{1.5}$$

where

$A_0 =$ Area of the orifice (m^2)

$C_d =$ Orifice discharge coefficient

$P_R =$ Recess (pocket) pressure (Pa)

$P_S =$ Supply pressure (Pa)

$Q_0 =$ Flow rate through an orifice $\left(\mathrm{m}^3/\mathrm{s}\right)$

$\rho =$ Working fluid density $\left(\mathrm{kg}/\mathrm{m}^3\right)$

Calculation of C_d using this equation assumes all pocket pressures are equal to the measured average pocket pressure, and the flow through each orifice is equal. This assumption is necessary because the measurement taken cannot isolate any specific orifice [1].

Figures 15-17 show the derived orifice discharge coefficient versus center clearance for inlet supply pressures of 3.45, 10.34, and 17.24 bar, respectively. Coefficients (C_d) for orifices decrease slightly with increase in load and decrease in clearance. The calculations of orifice discharge coefficients for all test conditions are practically insensitive to rotational speed except for the 3.45 bar supply pressure and 17.5 kprm rotor speed case shown in Figure 15. The low-pressure, high-speed case (3.45 bar and 17.5 krpm, respectively) deviates from the general trend, as load increases.

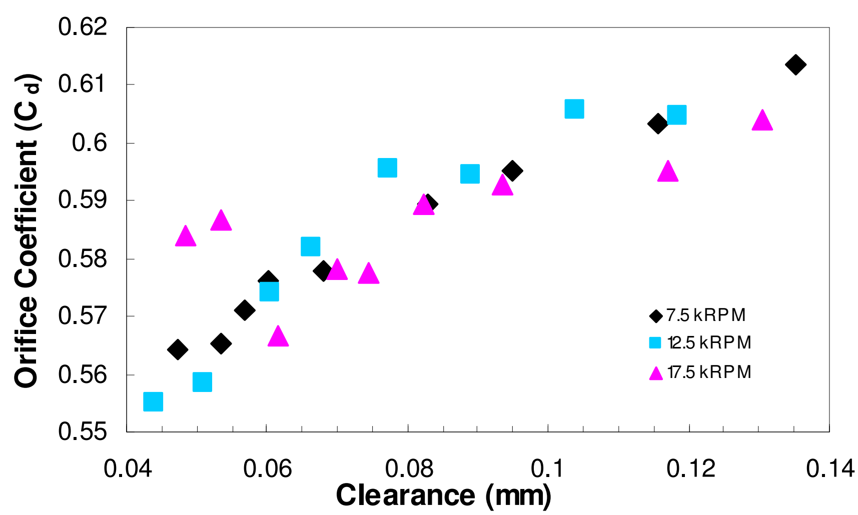

Figure 15: Orifice discharge coefficient estimations from test data for 3.45 bar test thrust bearing supply pressure at 7.5, 12.5, and 17.5 krpm

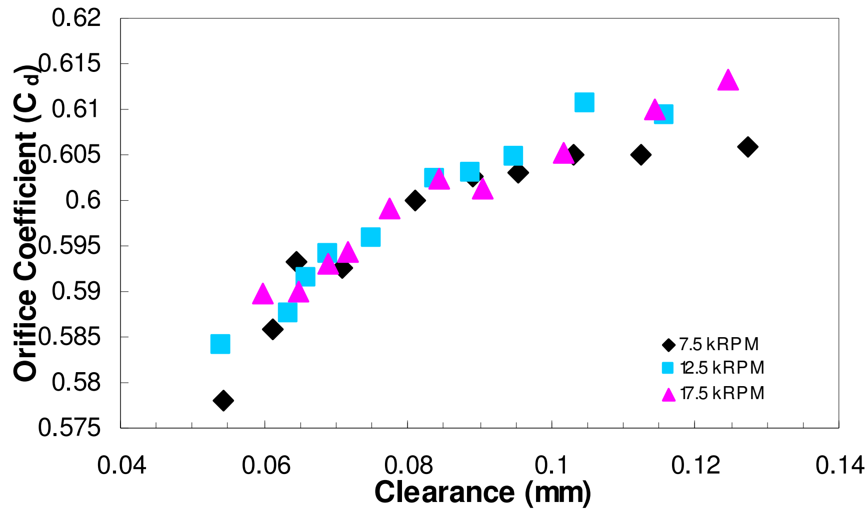

Figure 16: Orifice discharge coefficient estimations from test data for 10.34 bar test thrust bearing supply pressure at 7.5, 12.5, and 17.5 krpm

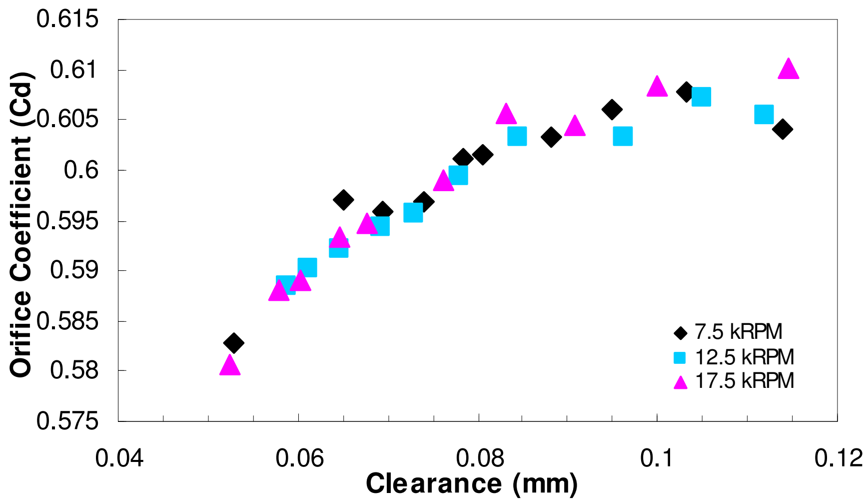

Figure 17: Orifice discharge coefficient estimations from test data for 17.24 bar test thrust bearing supply pressure at 7.5, 12.5, and 17.5 krpm

Figure 18 shows C_d versus clearance for inlet supply pressure case of 17.24 bar at 7.5, 12.5, and 17.5 rpm speed, which are relatively constant. The figure also shows the derived C_d, extracted from the static measurements of Forsberg [1], for the 17.24 bar TTB supply pressure case at 0 rpm speed for comparison. C_d's at this high bearing supply pressure and at speed test cases exhibit good correlation versus C_d's at 0 rpm speed for clearance values equal and greater than the nominal clearance of 76.2 μm. However, at zero speed test cases further decrease of clearances were achieved exhibiting lower values of C_d.

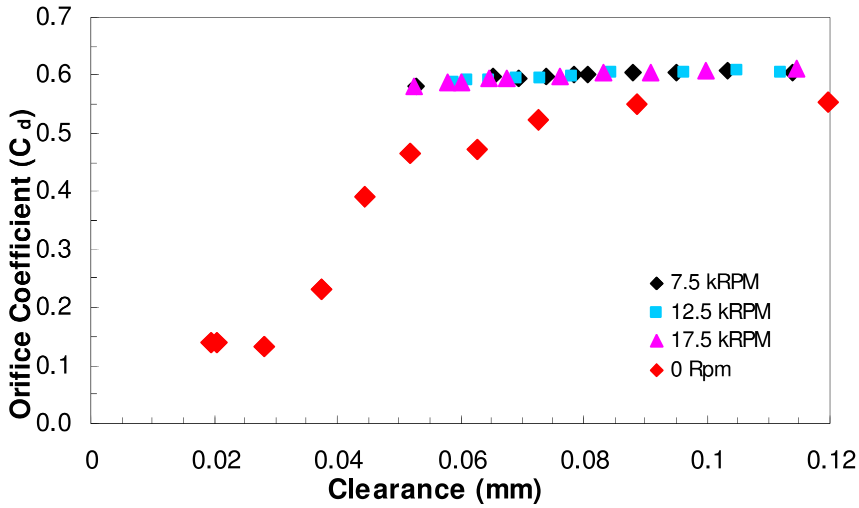

Figure 18: Comparison of orifice discharge coefficient estimations from test data for 17.24 bar TTB supply pressure at 7.5, 12.5, and 17.5 krpm versus 0 rpm case (Forsberg [1])

To examine the flow conditions at the inlet orifice, the orifice Reynolds number is calculated using Eq. (1.6).

$$\mathrm{Re}_{Orifice} = \left(\frac{\rho * V_{Orifice} * D_{Orifice}}{\mu} \right) \tag{1.6}$$

where

$\mathrm{Re}_{Orifice}$ = Orifice Reynolds number

ρ = Working fluid density $\left(\mathrm{kg}/\mathrm{m}^3 \right)$

$V_{Orifice}$ = Fluid velocity through orifice $\left(\mathrm{m}/\mathrm{s} \right)$

$D_{Orifice}$ = Diameter of the inlet orifice (m)

μ = Dynamic viscosity $\left(\mathrm{N*s}/\mathrm{m}^2 \right)$

The fluid velocity is derived from the measurement of the total inlet flow rate to the annulus of the TTB which distributes flow to its eight inlet orifices. The fluid velocity through the diameter of the inlet orifice was used to calculate $\mathrm{Re}_{\mathrm{orifice}}$. Figures 19-21 show the orifice Reynolds number versus clearance for inlet supply pressure cases of 3.45, 10.34, and 17.24 bar, respectively. Values of $\mathrm{Re}_{\mathrm{Orifice}}$ range from approximately

10,000 to 50,000 over the entire experimental test range made. Hence, the flow field is fully turbulent.

Munson et al [23] shows that the discharge coefficient can change with the Reynolds number until it is well into the turbulent regime. Orifice coefficients that increased significantly with increasing Reynolds numbers were also observed by Kurtin et al [24] during examination of flow within a hybrid journal bearing.

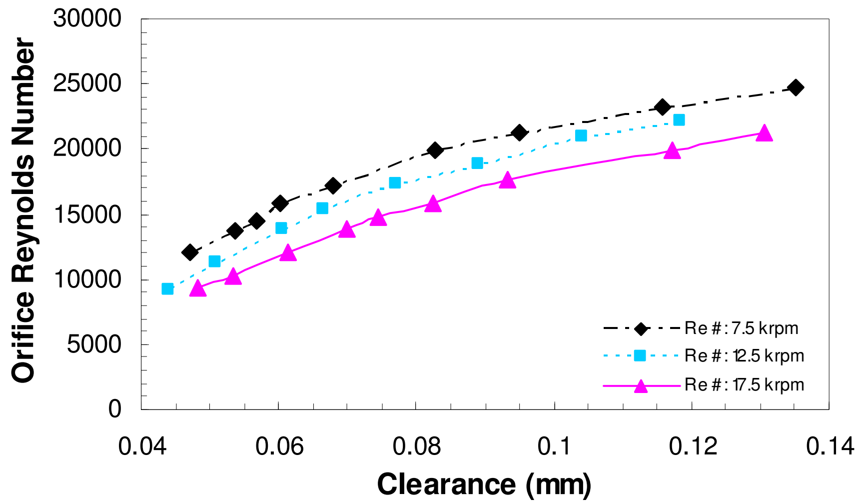

Figure 19: Orifice Reynolds number calculated from test data for 3.45 bar test thrust bearing supply pressure at 7.5, 12.5, and 17.5 krpm

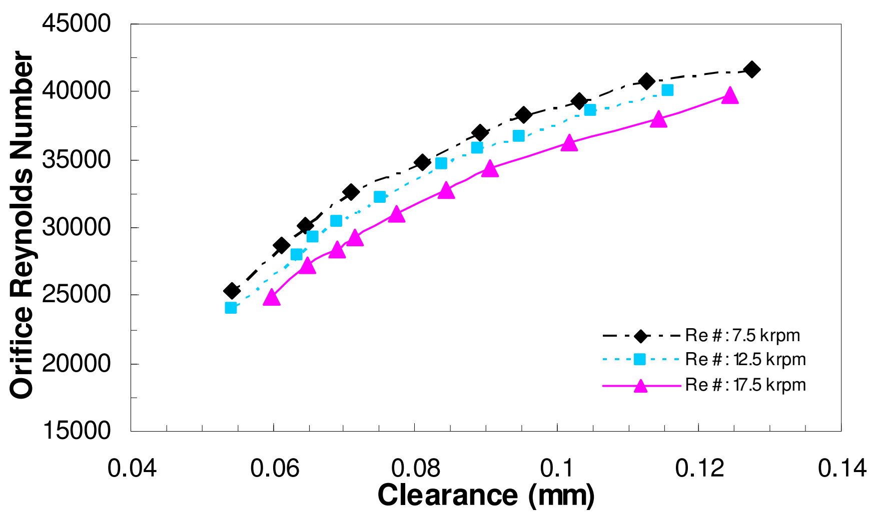

Figure 20: Orifice Reynolds number calculated from test data for 10.34 bar test thrust bearing supply pressure at 7.5, 12.5, and 17.5 krpm

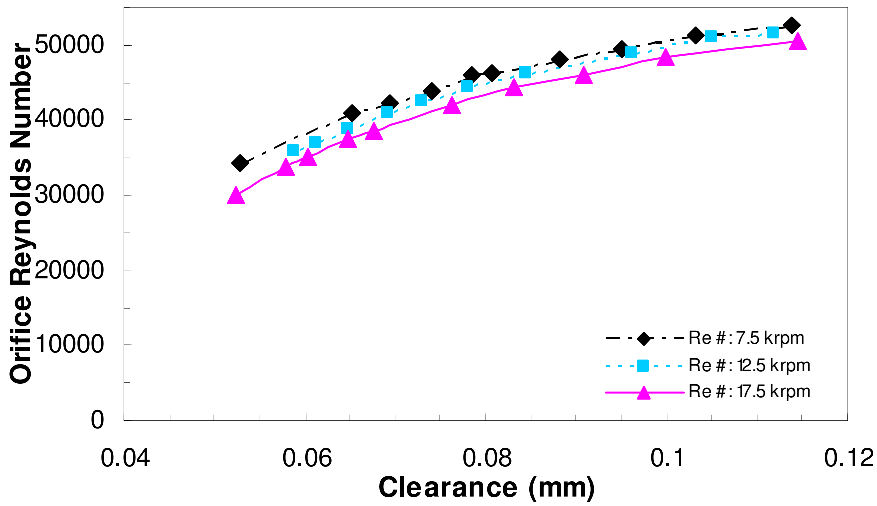

Figure 21: Orifice Reynolds number calculated from test data for 17.24 bar test thrust bearing supply pressure at 7.5, 12.5, and 17.5 krpm

A second non-dimensionless expression is used to examine the flow due to thrust collar rotation. The circumferential velocity of the thrust collar surface was used to calculate Reynolds number using Eq. (1.7).

$$\mathrm{Re}_{CircFlow} = \frac{\rho * \Omega * R_{out} * Z}{\mu} \tag{1.7}$$

where

$\mathrm{Re}_{CircFlow} =$ Circumferential flow Reynolds number

$\rho =$ Working fluid density $\left({kg}/{m^3} \right)$

$\Omega =$ Rotational collar speed $\left({rad}/{s} \right)$

$R_{out} =$ Outer radius of thrust bearing (m)

$Z =$ Center clearance of thrust bearing (m)

$\mu =$ Dynamic viscosity $\left({N * s}/{m^2} \right)$

The Reynolds number in Eq. (1.7) is not a function of feed pressure. Values of $\mathrm{Re}_{\mathrm{Circ\ Flow}}$ versus clearance are shown in Figure 22. The Reynolds number trend lines derived for the 7.5 and 12.5 krpm rotational speeds over the supply pressure range indicate flow dominated by inertial effects. The Reynolds number increases with increase in rotational speed while clearance increases (axial load decrease). Therefore, at

the high rotational speed (17.5 krpm) the derived Reynolds number ranges at greater magnitude, from approximately 3,000 to 8,500, to indicate flow increasingly dominated by fluid inertial effects as clearance increases (low loads).

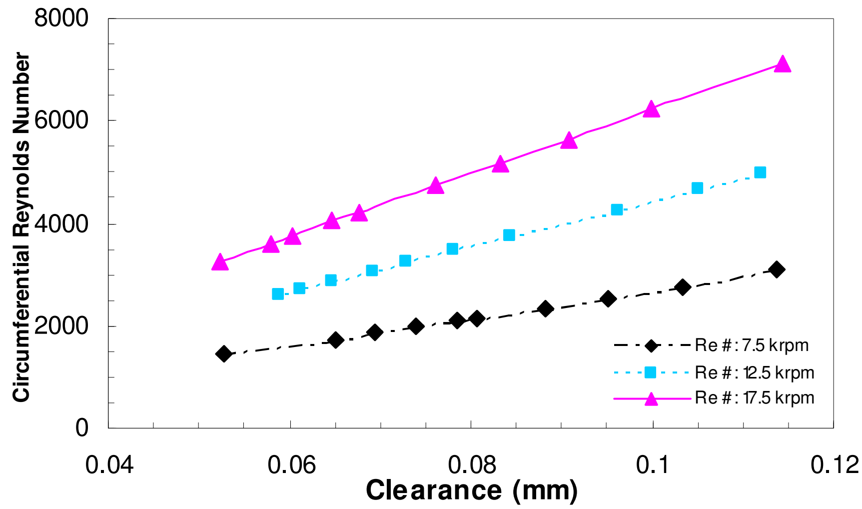

Figure 22: Circumferential flow Re # calculated from test data for 17.24 bar test thrust bearing supply pressure at 7.5, 12.5, and 17.5 krpm

For XLHydroTHRUST® predictions, a constant orifice discharge coefficient (C_d) is required. For this purpose all load ranges (of eight to ten fixed clearances) for each supply pressure and running-speed cases were divided into two groups, designated "low load" and "high loads". An average C_d value was taken for each subset of test conditions. The calculated C_d values vary between 0.56 and 0.61. Table 4 shows the subset averages.

Table 4: Average orifice discharge coefficient used for XLHydroTHRUST® predictions

Rotor Speed (krpm)	Average orifice discharge coefficient	
3.45 bar P_{supply} case		
	low load	*high load*
7.5	0.60 (4 data points)	0.57 (5 data points)
12.5	0.60 (5 data points)	0.56 (3 data points)
17.5	0.60 (4 data points)	0.58 (5 data points)
10.34 bar P_{supply} case		
7.5	0.60 (6 data points)	0.59 (4 data points)
12.5	0.60 (6 data points)	0.59 (4 data points)
17.5	0.61 (6 data points)	0.59 (4 data points)
17.24 bar P_{supply} case		
7.5	0.60 for entire load range (10 data points)	
12.5	0.60 (6 data points)	0.59 (4 data points)
17.5	0.60 (5 data points)	0.59 (5 data points)

An input for XLHydroTHRUST® includes the static misalignment about each axis, in radians, of the test thrust bearing face. An evaluation of measured misalignment was undertaken using Eqs. (1.1) and (1.2) for each test condition. Conversion from slope angle measurements to radians is accomplished by using the slope in $^{mm}/_{mm}$ and taking the inverse tangent. Due to small angles, the resulting angle is close to the slope in $^{mm}/_{mm}$ [1]. Figures 23-31 show the measured misalignments of the test and slave thrust bearings versus axial load for all supply pressure and running-speed cases. Misalignments are presented as an axial displacement (a product of outer diameter of the thrust bearing, 76.2 mm, and misalignment angle) which is an indication of clearance change around the circumference of the bearing.

The figures illustrate that measurements of the test thrust bearing were performed at low misalignment values for all test conditions evaluated. Also, misalignment was maintained within a targeted range ±0.013 mm (approximately .5 mil) over the bearing face for the majority of the test conditions, indicated by the marker lines on Figures 23-31. A few steady-state readings are outside the limit at test conditions of low load operation. Furthermore, misalignment over the STB face is equal or less than the TTB. Figures 23-25 show the largest difference of misalignment between the two bearings for

the 3.45 bar pressure case for all speeds. In general, STB misalignment measurements are equal, but 180° out of phase in comparison to TTB misalignment measurements. Furthermore, the figures depict measured misalignments of the two bearings, similar in magnitude, but mirrored about the zero-axis from each other indicating that the rotor collar disk faces may not be parallel.

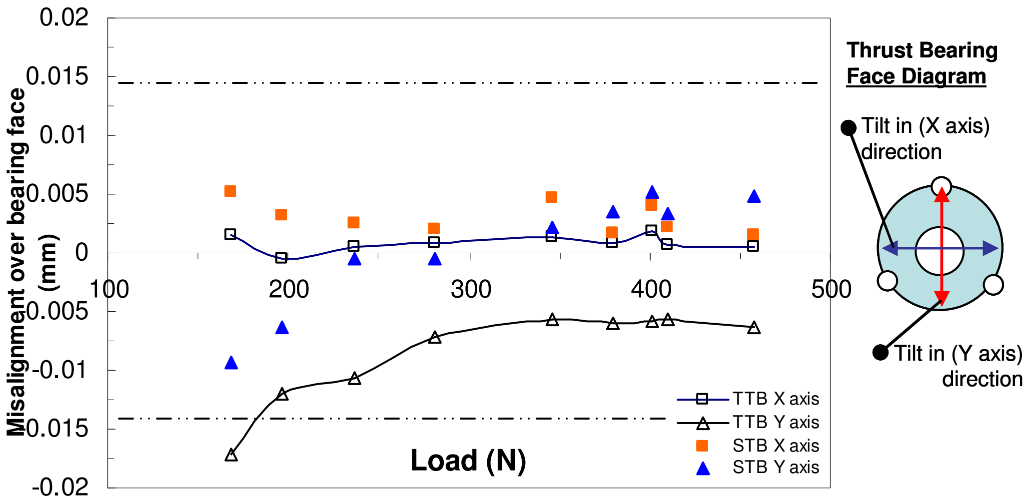

Figure 23: Test and slave thrust bearing face misalignment about the x and y axis versus load (3.45 bar, 7.5 krpm test case)

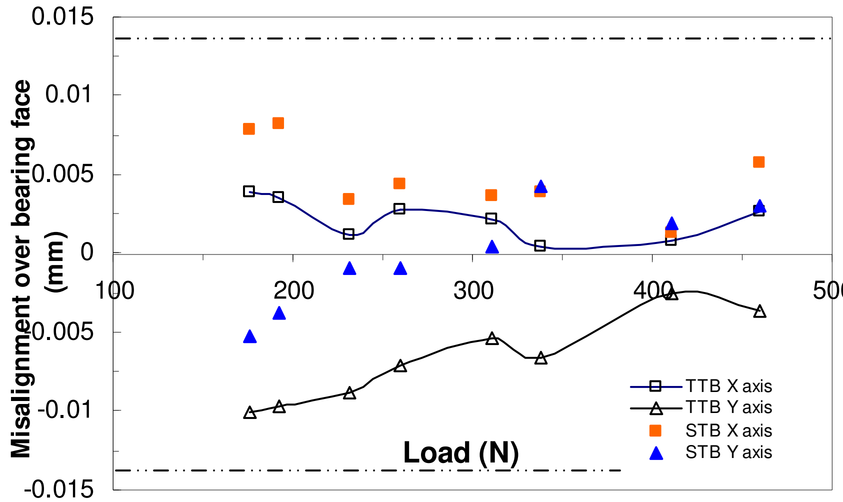

Figure 24: Test and slave thrust bearing face misalignment about the x and y axis versus load (3.45 bar, 12.5 krpm test case)

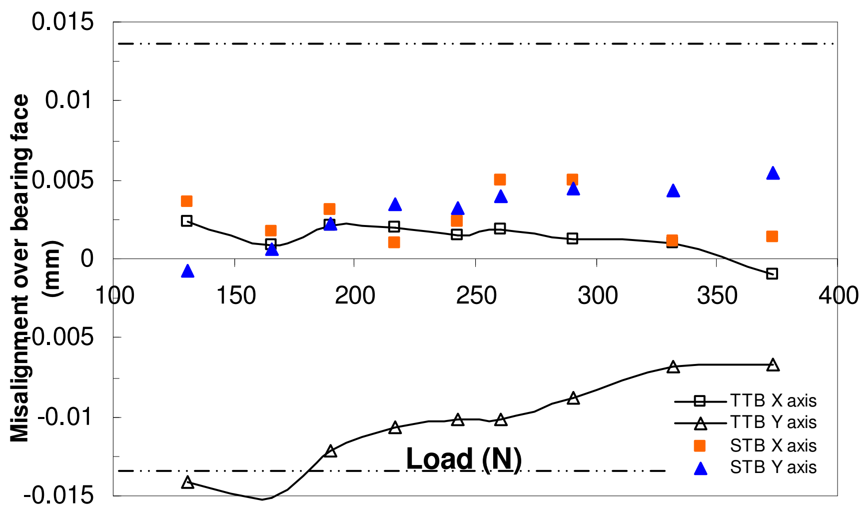

Figure 25: Test and slave thrust bearing face misalignment about the x and y axis versus load (3.45 bar, 17.5 krpm test case)

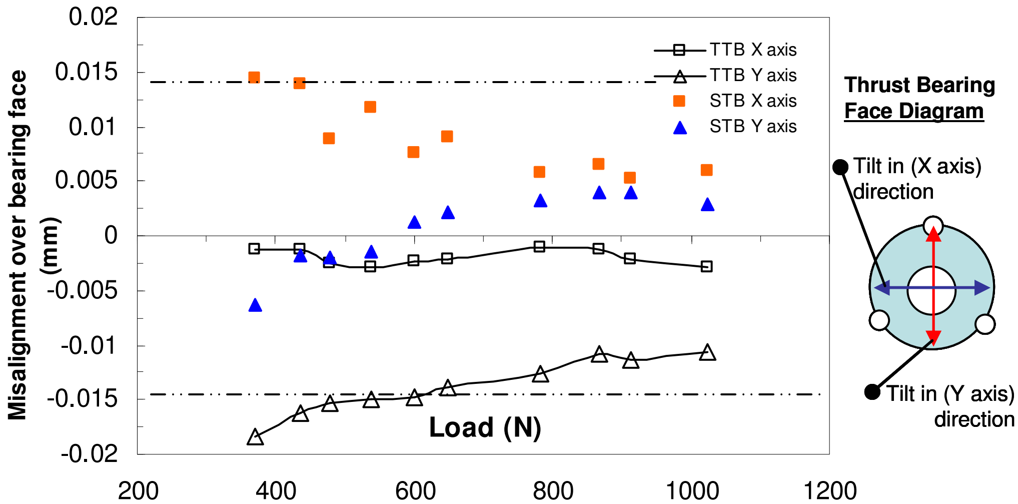

Figure 26: Test and slave thrust bearing face misalignment about the x and y axis versus load (10.34 bar, 7.5 krpm test case)

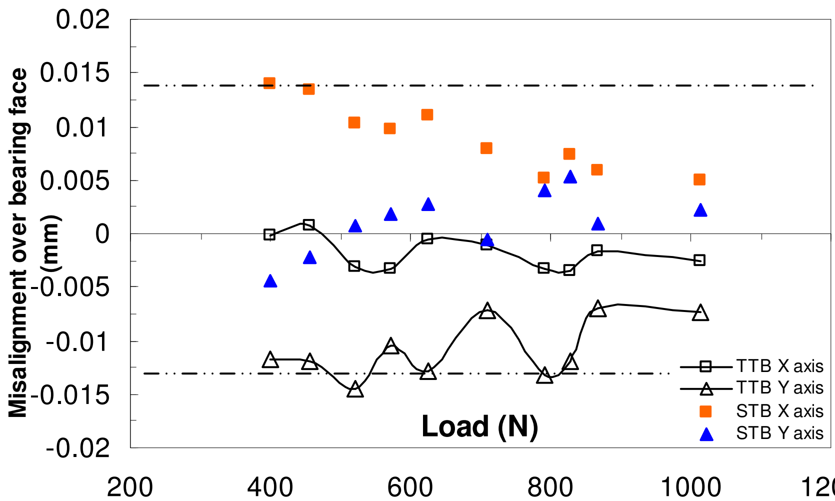

Figure 27: Test and slave thrust bearing face misalignment about the x and y axis versus load (10.34 bar, 12.5 krpm test case)

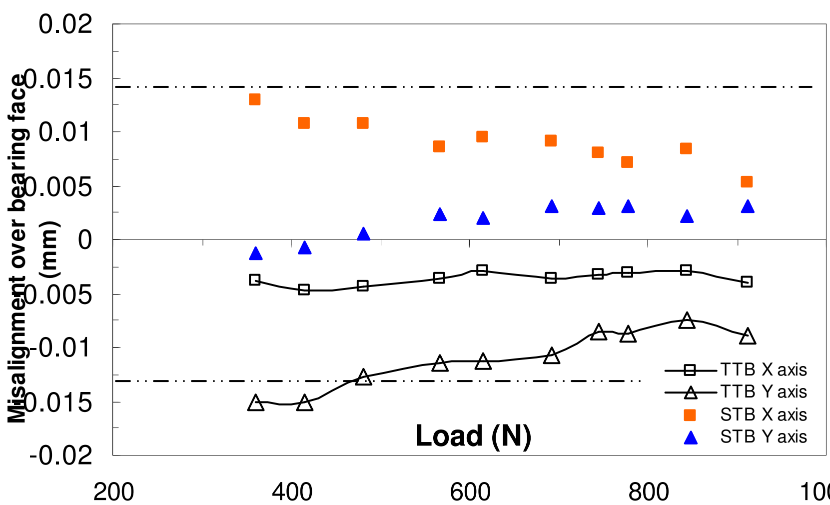

Figure 28: Test and slave thrust bearing face misalignment about the x and y axis versus load (10.34 bar, 17.5 krpm test case)

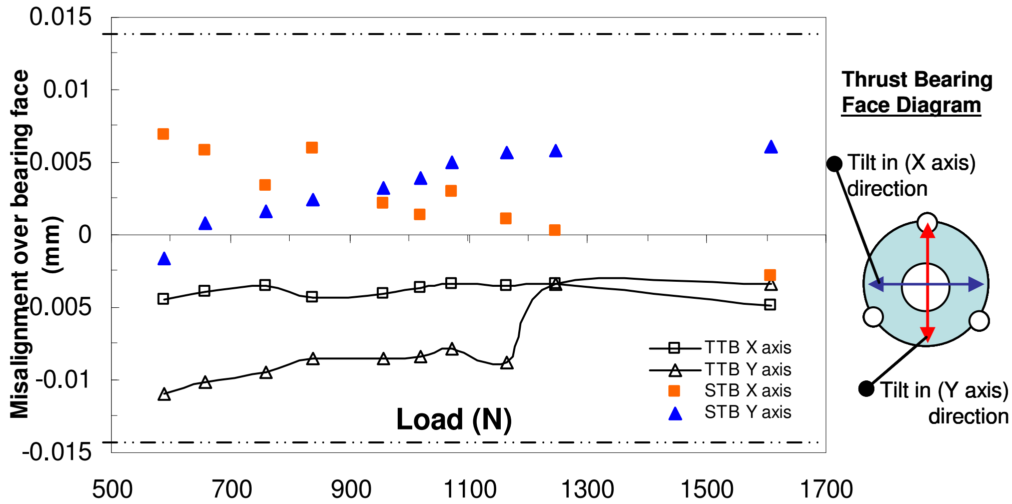

Figure 29: Test and slave thrust bearing face misalignment about the x and y axis versus load (17.24 bar, 7.5 krpm test case)

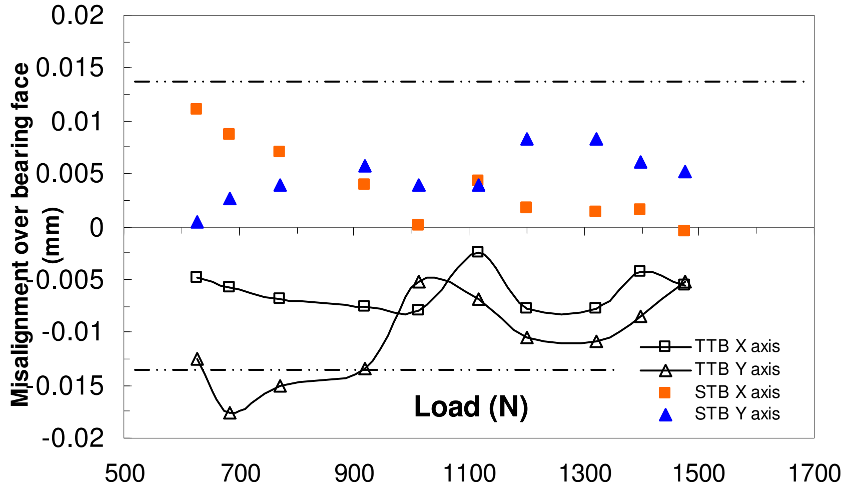

Figure 30: Test and slave thrust bearing face misalignment about the x and y axis versus load (17.24 bar, 12.5 krpm test case)

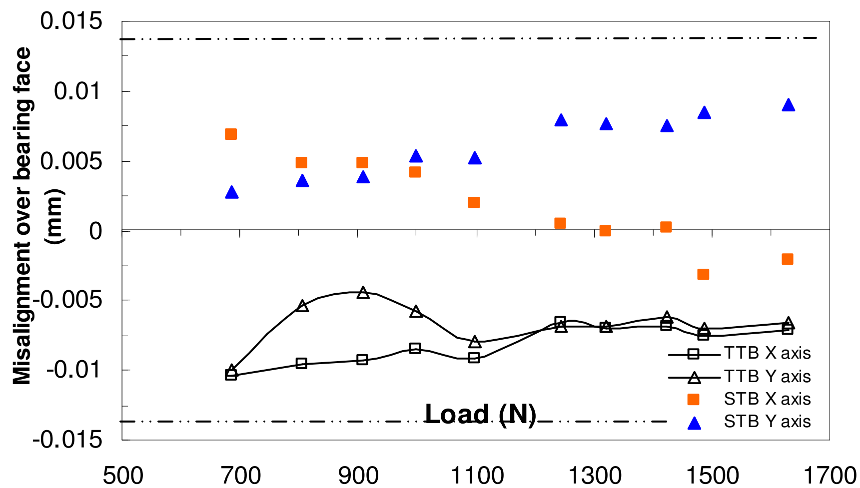

Figure 31: Test and slave thrust bearing face misalignment about the x and y axis versus load (17.24 bar, 17.5 krpm test case)

Absolute clearance readings are used to calculate the misalignment slopes about the *x* and *y* axis of the TTB and STB in relation to its thrust collar face. The uncertainties of the three small clearance reading of each thrust bearing are on average 12% of the proximity probe measurements, and are propagated through to the bearing misalignment calculations. Figure 32 show the extremely small misalignment values (in one thousandth of a degree) of the TTB 17.24 bar supply pressure case at 17.5 krpm rotational speed, which generate large average uncertainties due to the large standard deviation of the fifteen readings for a single proximity probe reading. The average uncertainty of the TTB misalignment over the bearing face (about the vertical axis) is 663% using the (M_1) slope equation, and the average uncertainty of the TTB misalignment over the bearing face (about the horizontal axis) is 175% using (M_2). STB misalignment over the bearing face was generally twice the value of the corresponding uncertainties of the TTB misalignment.

In general, the calculation of the misalignment of the bearing face plane in the M_2 direction utilizes all three proximity probe measurements yielding a lower uncertainty than the misalignment calculation in the M_1 direction, which uses only two proximity probe measurements. For the 3.45 bar supply pressure case, misalignment uncertainties improved with increase in axial loading at all tested running speeds, while the other two pressure cases exhibited constant values of uncertainties for a given load range at running speed.

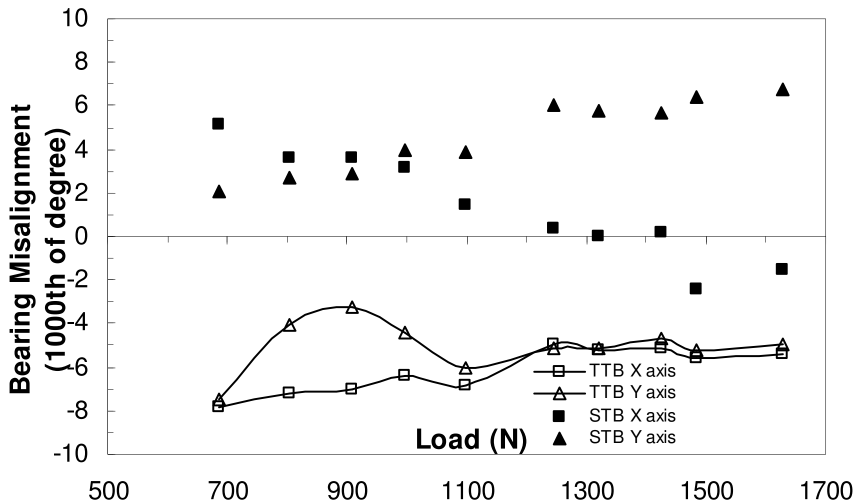

Figure 32: Test and slave thrust bearing face misalignment (in degrees) about the x and y axis versus load (17.24 bar, 17.5 krpm test case)

Finally, the temperature of the inlet water was determined from an average of the recorded water inlet temperatures. Measured average inlet temperatures are used as an input for XLHydroTHRUST® to predict the thrust bearing behavior; values are shown in Table 5.

Table 5: Test thrust bearing inlet water temperature used as input for XLHydroTHRUST® specification

Rotor Speed (krpm)	Average Inlet TTB Temperature
3.45 bar P_{supply}	33.4 ± 1.1 °C
10.34 bar P_{supply}	33.9 ± 1.1 °C
17.24 bar P_{supply}	34.8 ± 1.1 °C

The first parameter of interest for comparison between measurement and predictions are flow rates of the TTB. The pressure differential determines the volumetric flow rate across the bearing face. Since, the sum of volumetric flow rate into the inner and outer radius equals the net (inlet) flow rate across the test bearing annulus, the measured inlet flow rate and inner radius exit flow rate is sufficient for comparison to predictions Figures 33-35 show inlet and inner-radius discharge flow rates as a function of center clearance for the 3.45 bar TTB supply pressure at 7.5, 12.5, and 17.5 krpm rotational speeds, respectively. The figures show measurements and predictions for inlet flow rates decreasing as the clearances decrease with increasing load. For the low speed

case (7.5 krpm) in Figure 33, measurements and predictions of inlet flow rate correlate well (1.5% to 5% difference). Uncertainties for the inlet flow rates are barely noticeable on the figure (average of 1.2%). Figure 33, also, shows comparison of inner radius discharge flow rates slightly increasing to a certain intermediate load, and then slightly decreasing with increase in load (to small clearance). Inner radius discharge flow rate predictions show an 11% difference on average when compared to the experimental results (exclusion of a single highly erroneous data point). Uncertainties for the inner radius discharge flow rates on average are 16%. Note, the derived averaged orifice discharge coefficient used for predictions on a certain subset of data points of a given supply pressure and running-speed cases is stated in the figures' caption (refer to Table 4).

Figure 34 shows measurements and predictions of flow rates for the low pressure mid-speed case (3.45 bar and 12.5 krpm, respectively) of the TTB. The inlet flow rates decrease as the clearance decreases (due to increased load). Predictions show very good agreement with measured data (0.5 % to 6.4 % difference). Uncertainties for the inlet flow rates are barely noticeable on the figure (average of 1.2 %). Also, inner radius discharge flow rates show the same crowning trend as the low pressure low speed case. Inner radius discharge flow rate predictions show a 20% difference when compared to the experimental results; and uncertainty of measurement average 20%.

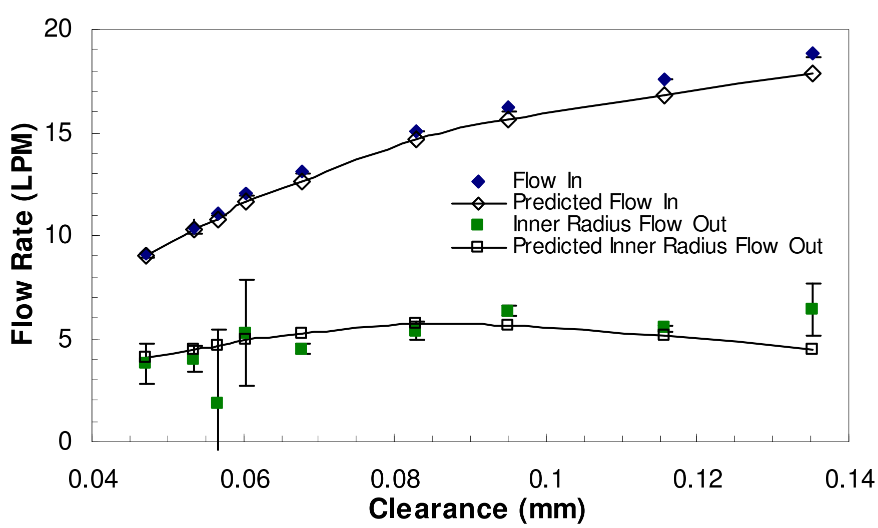

Figure 33: Measured and predicted inlet flow rate and inner radius discharge flow rate for 3.45 bar thrust bearing supply pressures at 7.5 krpm speeds, with uncertainty bars, C_d= 0.60 (low loads) and 0.57 (high loads)

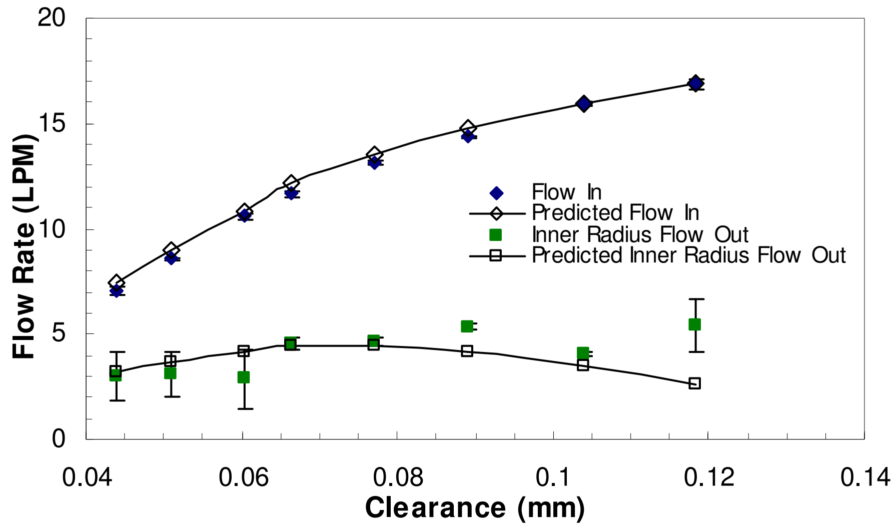

Figure 34: Measured and predicted inlet flow rate and inner radius discharge flow rate for 3.45 bar thrust bearing supply pressure at 12.5 krpm speed, with uncertainty bars, C_d= 0.60 (low loads) and 0.56 (high loads)

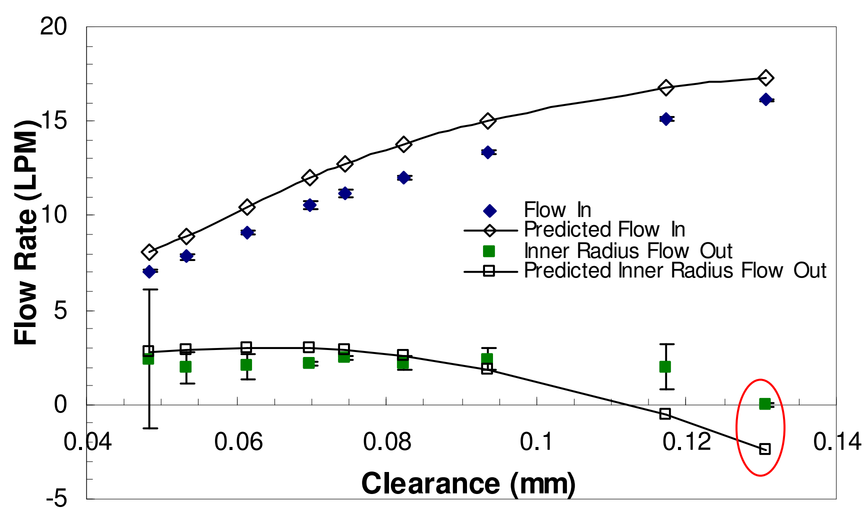

Figure 35: Measured and predicted inlet flow rate and inner radius discharge flow rate for 3.45 bar thrust bearing supply pressure at 17.5 krpm speed, with uncertainty bars, C_d= 0.60 (low loads) and 0.58 (high loads)

Figure 35 compares measurements and predictions of flow rates for the low-pressure, high-speed case (3.45 bar and 17.5 krpm, respectively) of the test thrust bearing. The inlet flow rates decrease as the clearance decreases. Predictions show satisfactory agreement with experimental data (7.5% to 14.5% difference). Predicted results are slightly over predicted at the low-pressure, high-speed test conditions. Uncertainties for

the inlet flow rates are barely noticeable on the figure (average of .1%). Inner radius discharge flow rates show the same crowning trend as the low pressure low speed case. The points, marked by a red circle, shows a predicted test condition (at low-load, high-speed) and a measured discharge flow rate at a comparable clearance. The measured discharge flow rate yielded zero flow verified by observation of no flow through see-through discharge lines and zero LPM reading on digital display. Also, pressure readings of the bearing land recorded negative DC voltage outputs; therefore starvation of the fluid film across portions of the bearing land occurred. Inner radius discharge flow rate predictions show a 28% difference when compared to the experimental results.

Please note the reduction of the inner radius discharge flow rate as speed progresses for the low pressure case. This series show centrifugal acceleration reducing inner radius flow and increasing outer radius flow leading to eventual starvation (sub-ambient pressures) at the inner radius.

Figures 36-41 compare predictions and measurements of flow rates for the mid and high TTB supply pressure (10.45 and 17.24 bar) cases over the rotational speed range. Note that, at the same thrust bearing supply pressure and load, the flow rates are decreased by increasing rotational speed. Also, flow rates increase with increase in supply pressure. Thus, Figures 36-41 repeat the flow behaviors of the low-supply-pressure case. The figures show inlet flow rates decreasing as the clearances decrease with increasing load. Also for these cases, inner radius discharge flow rates slightly decrease as the clearances decrease. Substantial inner radius discharge flow rate (approximately 5 to 15 LPM) is sustained compared to the low supply pressure case flow rate (approximately 0 to 5 LPM).

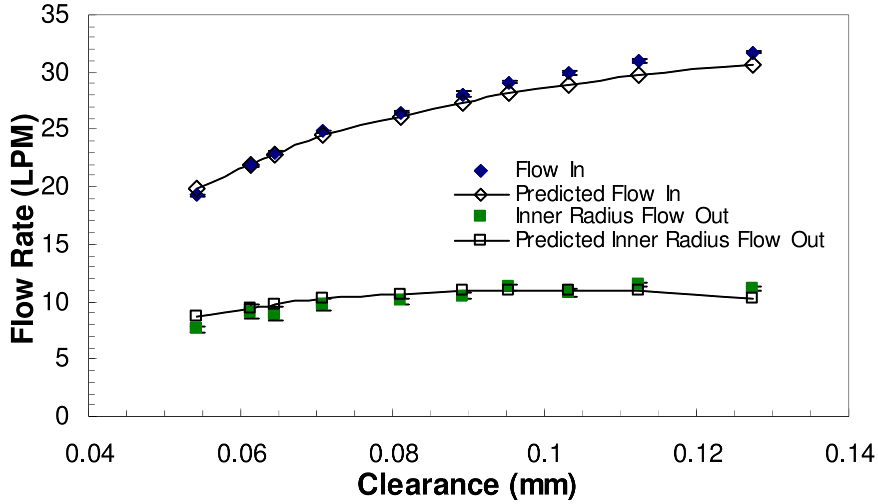

Figure 36: Measured and predicted inlet flow rate and inner radius discharge flow rate for 10.45 bar TTB supply pressure at 7.5 krpm speed, with uncertainty, C_d= 0.60 (low loads) and 0.59 (high loads)

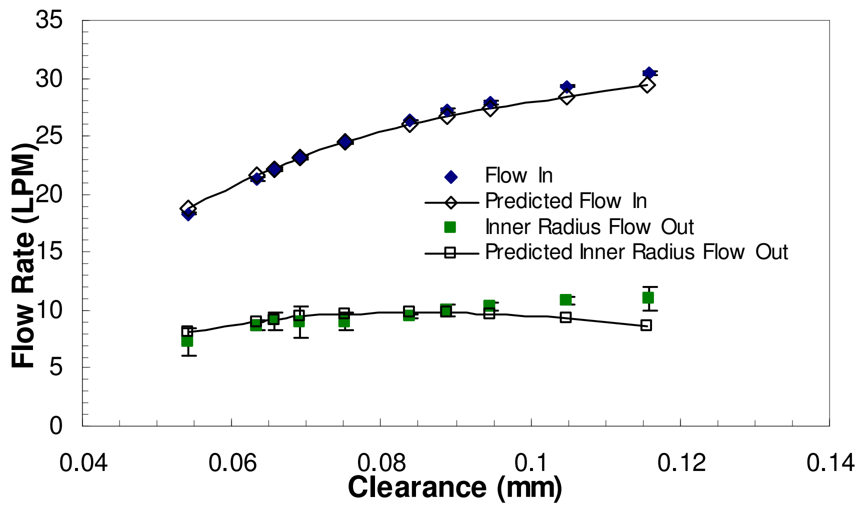

Figure 37: Measured and predicted inlet flow rate and inner radius discharge flow rate for 10.45 bar TTB supply pressure at 12.5 krpm speed, with uncertainty, C_d= 0.60 (low loads) and 0.59 (high loads)

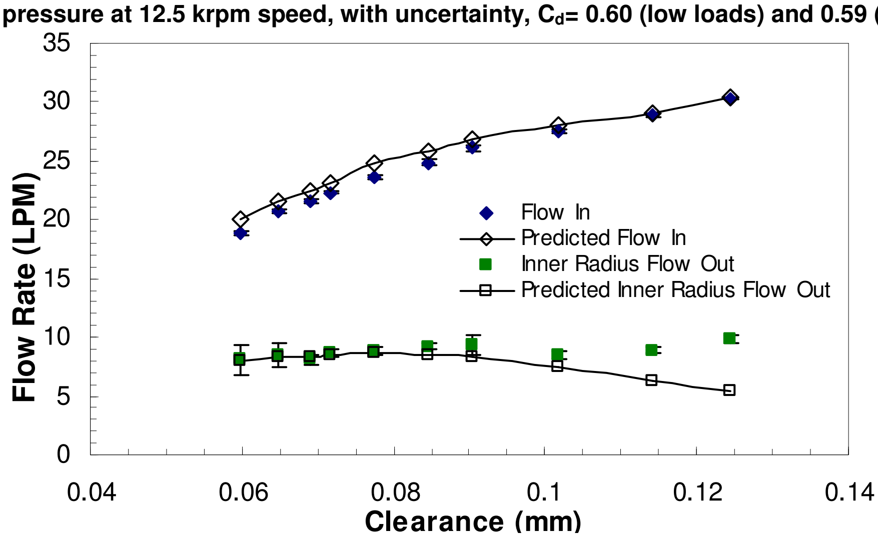

Figure 38: Measured and predicted inlet flow rate and inner radius discharge flow rate for 10.45 bar TTB supply pressure at 17.5 krpm speed, with uncertainty, C_d= 0.61 (low loads) and 0.59 (high loads)

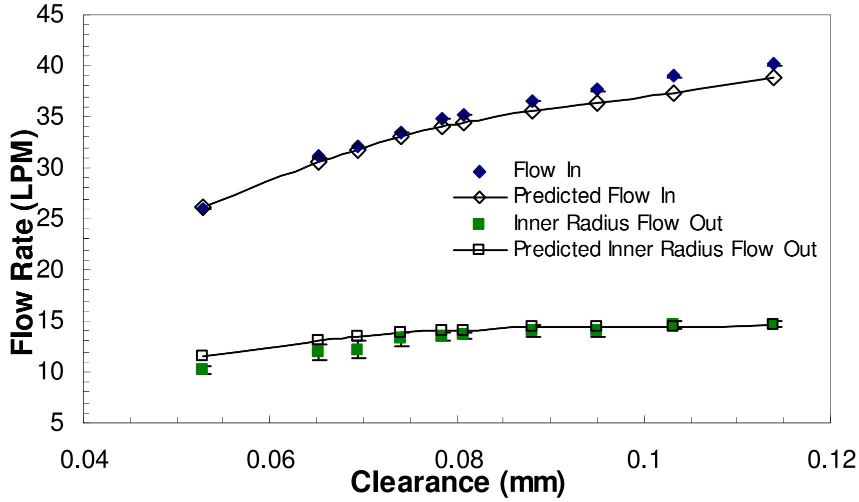

Figure 39: Measured and predicted inlet flow rate and inner radius discharge flow rate for 17.24 bar TTB supply pressure at 7.5 krpm speed, with uncertainty, C_d= 0.60 (entire load range)

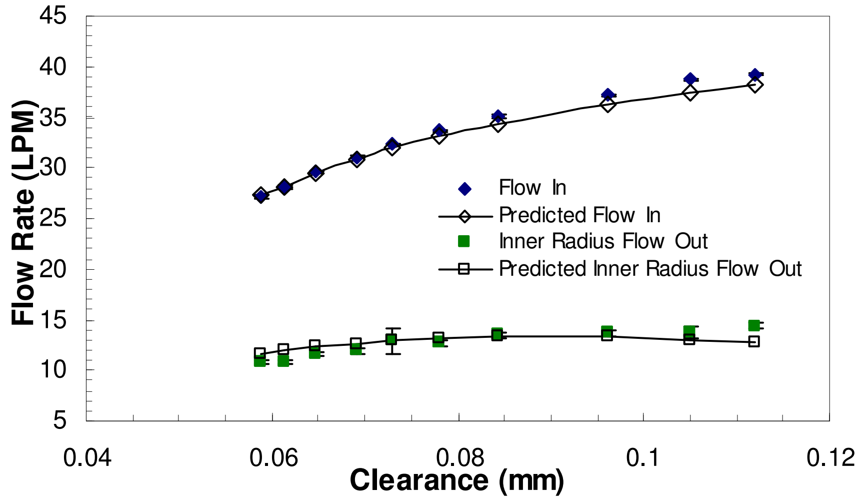

Figure 40: Measured and predicted inlet flow rate and inner radius discharge flow rate for 17.24 bar TTB supply pressure at 12.5 krpm speed, with uncertainty, C_d= 0.60 (low loads) and 0.59 (high loads)

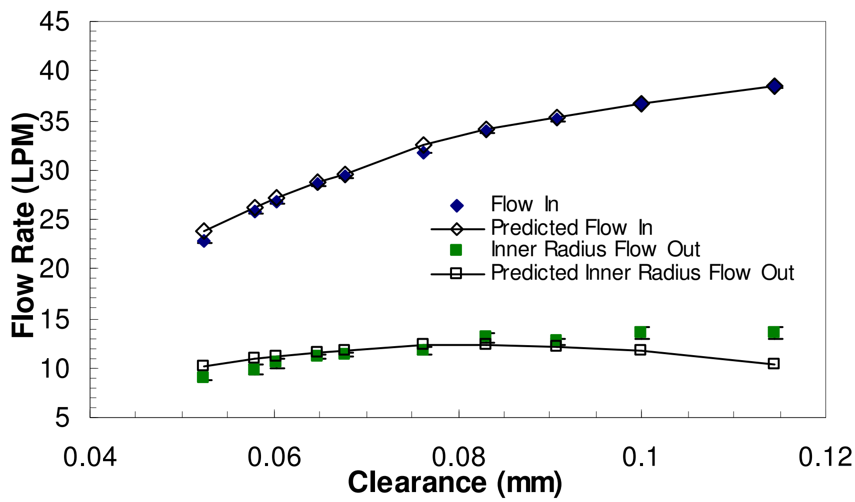

Figure 41: Measured and predicted inlet flow rate and inner radius discharge flow rate for 17.24 bar TTB supply pressure at 17.5 krpm speed, with uncertainty, C_d= 0.60 (low loads) and 0.59 (high loads)

Figures 36-38 show measurements and predictions of flow rates for 10.45 bar thrust bearing supply pressure cases at speeds. Inlet flow rate prediction results show very good agreement with measured data (2% to 3% average difference) over the speed range. Inner radius discharge flow rate predictions show a 5% to 11% average difference over the speed range. Uncertainties for the inlet and inner radius discharge flow rate measurements are 0.8% and 6% averaged, respectively.

Figures 39-41 show measurements and predictions of flow rates for 17.24 bar thrust bearing supply pressure cases at speeds. Inlet flow rate predictions show very good agreement with measured data (1% to 2% average difference) over the speed range. Inner radius discharge flow rate predictions show a 5% to 9% average difference. Uncertainties for the inlet and inner radius discharge flow rate measurements are 0.4% and 3% averaged, respectively.

The calculated differences between measurements and XLHydroTHRUST® predictions of flow rates were calculated using Eq. (1.8):

$$\%\text{ Difference}=\frac{\left|\text{Measured Value}-\text{ Predicted Value}\right|}{\text{Measured Value}}*100 \tag{1.8}$$

Subsequent comparison between measurements and predictions of the operating performance characteristics cites Eq. (1.8), as well, to quantify average difference or a range of percentage difference for a given supply pressure and running-speed case.

Figure 42 show inlet flow rates as a function of center clearance, Z_c, see Eq. (1.10) for the 17.24 bar TTB supply pressure at 17.5 krpm rotational speed. The figure also shows measurements and predictions of inlet flow rates for 17.24 bar TTB supply pressure cases at 0 rpm speed, extracted from the static measurements of Forsberg [1]. The comparison between the two sets of flow rate measurements show good agreement for test case clearance values equal and greater than the nominal clearance of 76.2 μm.

However, at zero speed test cases further decrease of clearances were achieved exhibiting low values of TTB inlet flow rate.

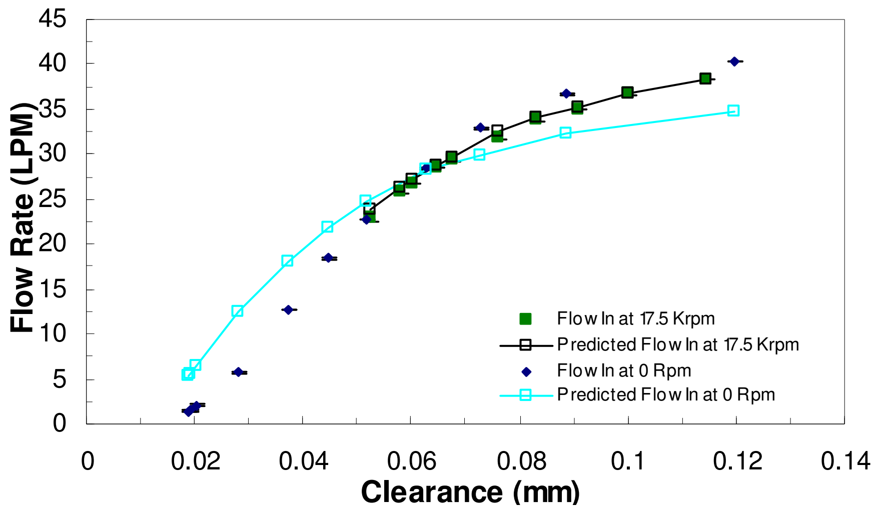

Figure 42: Comparison between measured and predicted inlet flow rate for 17.24 bar TTB supply pressure at 0 rpm (Forsberg [1]) and 17.5 krpm speeds

Figure 43 shows inner radius discharge flow rates as a function of center clearance for the 17.24 bar TTB supply pressure at 17.5 krpm rotational speed. The figure also shows measurements and predictions of inner radius discharge flow rates for 17.24 bar TTB supply pressure cases at 0 rpm speed, extracted from the static measurements of Forsberg [1]. The comparison between the two sets of flow rate measurements show good agreement for test case clearance values equal and greater than the nominal clearance of 76.2 μm. However, at zero speed test cases, further decreases of clearance were achieved exhibiting low values of TTB inlet flow rate. Also, comparison of predicted flow rates between higher clearance test cases (approximately .12 mm) at 0 rpm speed and 17.5 rpm speed show a deviation: flow rate increases with increase in clearance (low load) at 0 rpm speed, and flow rate decreases with increase in clearance (low load) at 17.5 rpm speed.

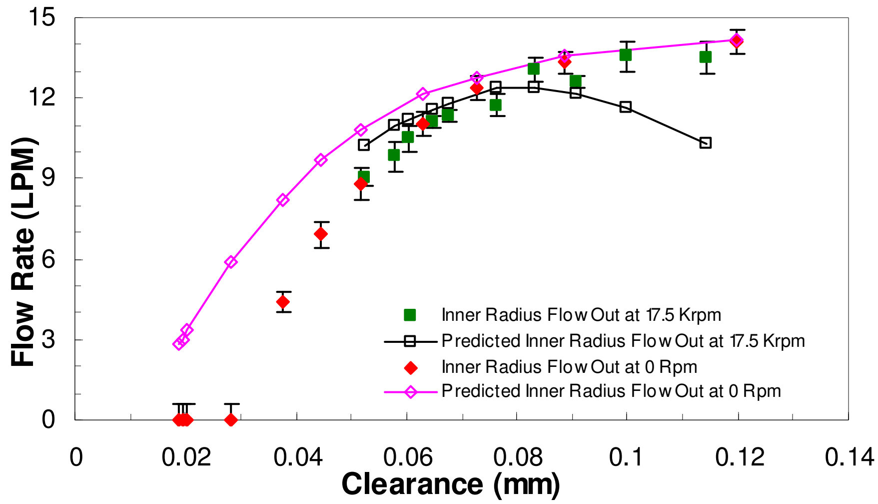

Figure 43: Comparison between measured and predicted inner radius discharge flow rate for 17.24 bar TTB supply pressure at 0 rpm (Forsberg [1]) and 17.5 krpm speeds

The next parameter of interest is the pocket pressure ratio defined in Eq. (1.9). The lubricant (water) travels from an annulus to each recess through an orifice restrictor which causes the pressure drop in lubricant (water), hence pressure ratio [25].

$$P_{Ratio} = \frac{P_{Pocket} - P_{Exhaust}}{P_{Supply} - P_{Atmospheric}} \qquad \textbf{(1.9)}$$

where

P_{Ratio} = Pressure ratio

P_{Pocket} = Pocket pressure

$P_{Exhaust}$ = Pressure bearing exhaust into

P_{Supply} = Supply pressure

$P_{Atmospheric}$ = Atmospheric pressure

Figures 44-52 show pressure ratios as a function of center clearance for the supply pressures 3.45, 10.34, and 17.24 bar at 7.5, 12.5, and 17.5 krpm rotational speeds, respectively. In general, pressure ratio increases as clearance decreases (load increases). Also, for an increase in rotational speed and/or the supply pressure, pressure ratios increase since land flow resistance and turbulence are greater [26]. Due to displacement

control during testing, supply pressures and recess pressures are increased by increasing rotational speeds at a constant clearance. A final general trend of the figures indicates that the majority of the useful load range of the thrust bearing was covered during testing. The figures also show that the pocket 1 and pocket 4 pressure ratios are nearly identical over the tested ranges, providing another check that the test thrust bearing and rotor thrust disk misalignment is low [1].

Figures 44-46 provide a comparison between measurements and predictions for the pressure ratio of the 3.45 bar supply pressure at rotational speeds of 7.5, 12.5, and 17.5 krpm. The correlation improves with decreasing clearance (increasing load). The pressure ratios are over predicted for the 3.45 bar inlet bearing pressure. Pocket 1 pressure ratio predictions (nearly identical to pocket 4) show a 23.5% to 32% average difference (over the speed range) when compared to the measured results, with the correlation improving as speed increases. Uncertainties for the pressure ratios for the 3.45 bar inlet case are larger than the uncertainties of the 10.34 and 17.24 bar cases as indicated by the error bars on figures. The source for large uncertainties for the low pressure case is larger standard deviation of recess pressure measurements for the low-pressure-drop condition.

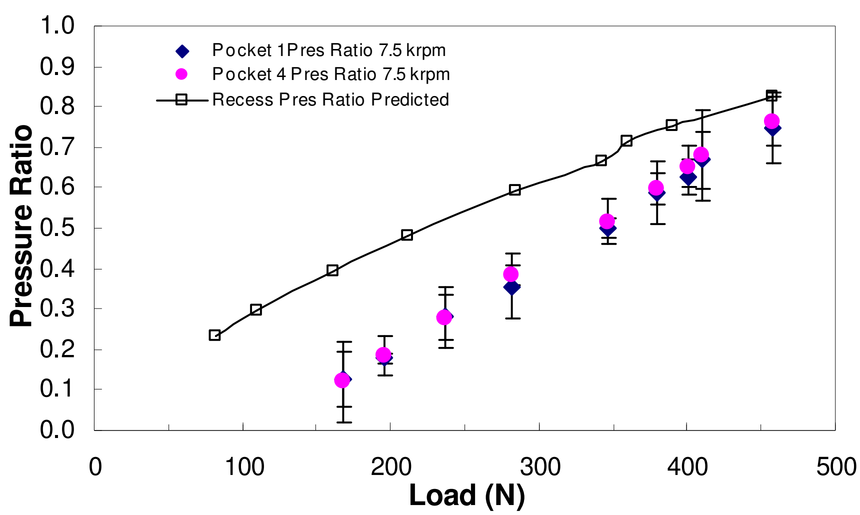

Figure 44: Pocket pressure ratios as a function of load for 3.45 bar thrust bearing supply pressure at 7.5 krpm rotor speed

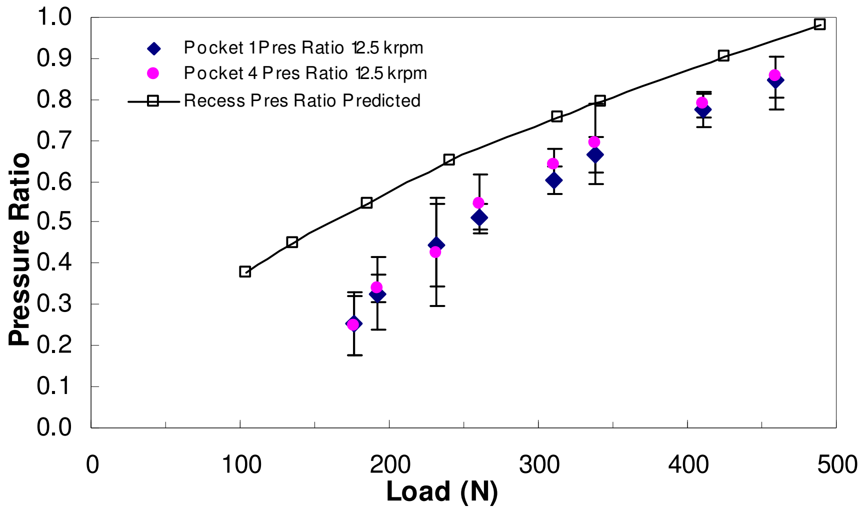

Figure 45: Pocket pressure ratios as a function of load for 3.45 bar thrust bearing supply pressure at 12.5 krpm rotor speed

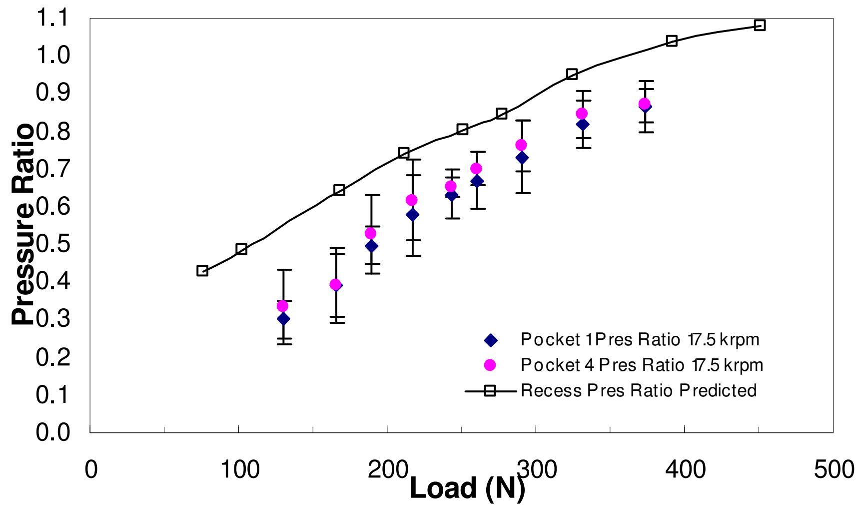

Figure 46: Pocket pressure ratios as a function of load for 3.45 bar thrust bearing supply pressure at 17.5 krpm rotor speed

Figures 47-49 show measurements and predictions of pressure ratios for the 10.45 bar supply pressure cases at test speeds. Pocket 1 pressure-ratio predictions (nearly the same for pocket 4) show satisfactory agreement with measurements [14.5 % to 17.13% average difference] over the speed range, with improvement as speed increases. Uncertainties for the pocket 1 pressure ratio measurements are 5.7% to 7.1% (average of each load range tested) over the speed range. Uncertainties decrease with increase in rotational speed as the pressure drop increased.

Figures 50-52 show measurements and predictions of pressure ratios for the 17.24 bar supply pressure cases at test speeds. Pocket 1 pressure ratio predictions results show satisfactory agreement with measurements (8.6% to 13 % average difference) over the speed range, with improvement as speed increases. Uncertainties for the pocket 1 pressure ratio measurement (nearly the same for pocket 4) are 4.7% averaged for the entire high pressure case. In contrast to the large uncertainty values of the low pressure case, the high pressure case show small uncertainties at steady-state operation during high-pressure-drop conditions.

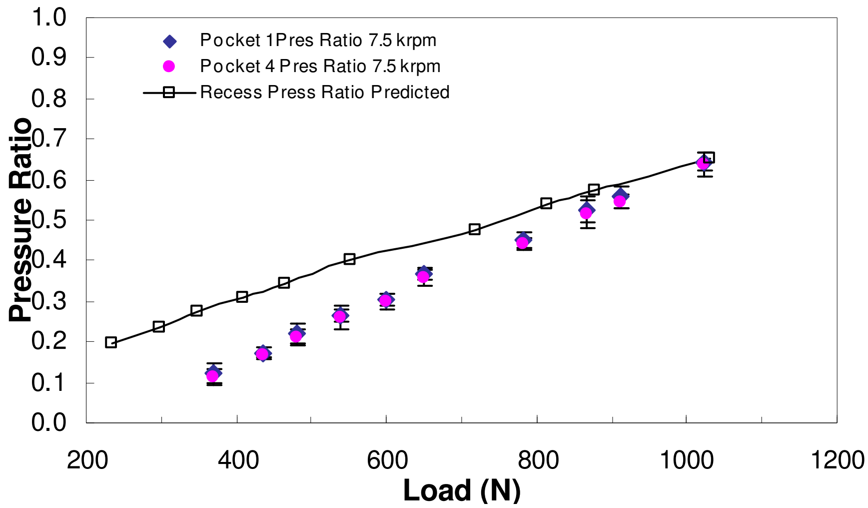

Figure 47: Pocket pressure ratios as a function of load for 10.45 bar thrust bearing supply pressure at 7.5 krpm rotor speed

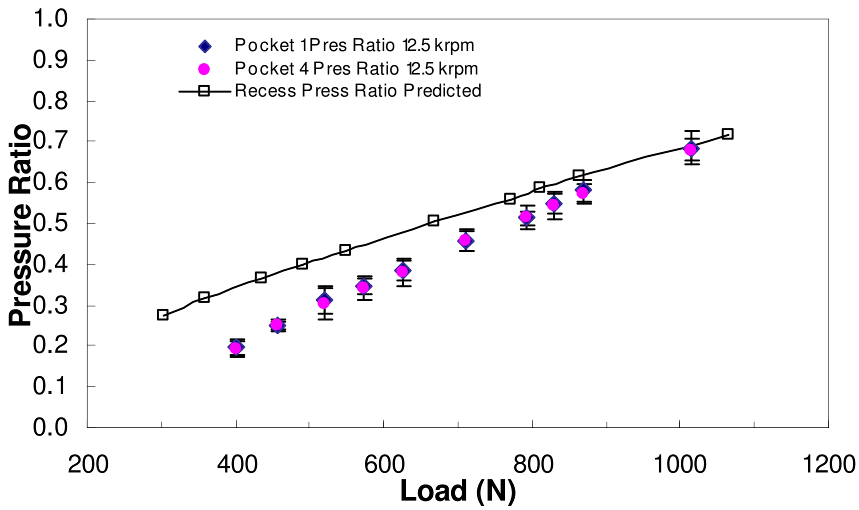

Figure 48: Pocket pressure ratios as a function of load for 10.45 bar thrust baring supply pressure at 12.5 krpm rotor speed

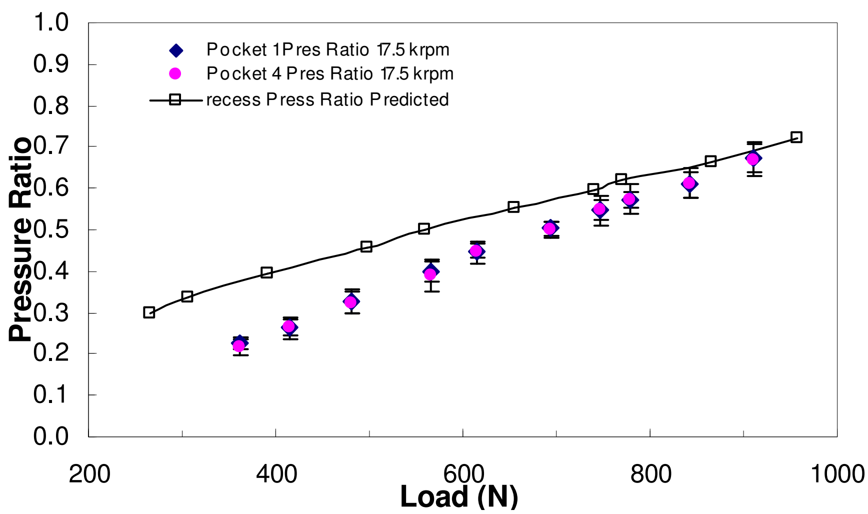

Figure 49: Pocket pressure ratios as a function of load for 10.45 bar thrust bearing supply pressure at 17.5 krpm rotor speed

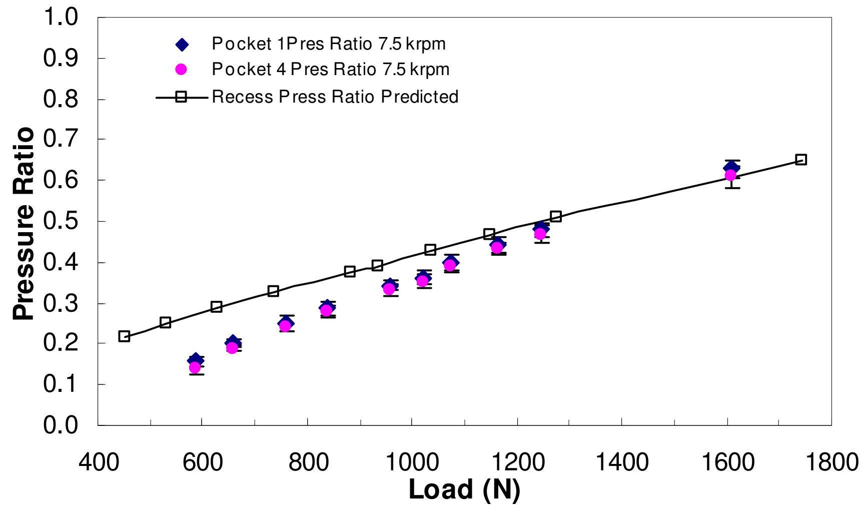

Figure 50: Pocket pressure ratios as a function of load for 17.24 bar thrust bearing supply pressure at 7.5 krpm rotor speed

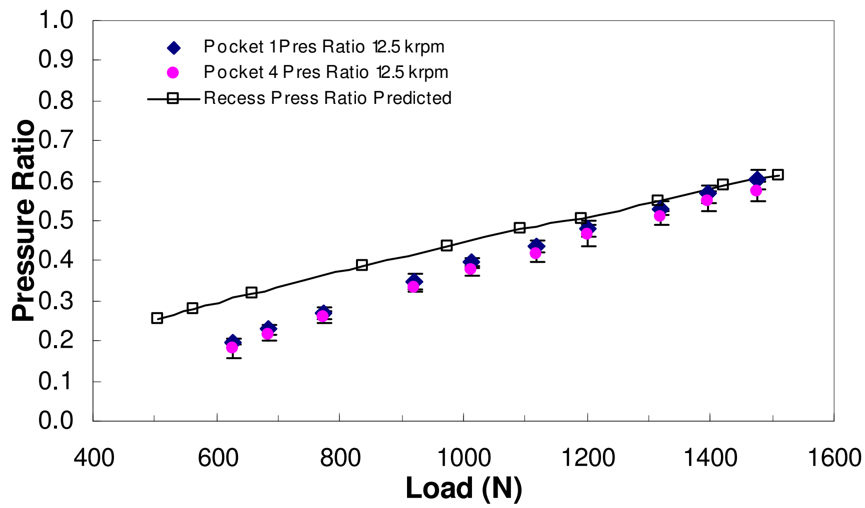

Figure 51: Pocket pressure ratios as a function of load for 17.24 bar thrust bearing supply pressure at 12.5 krpm rotor speed

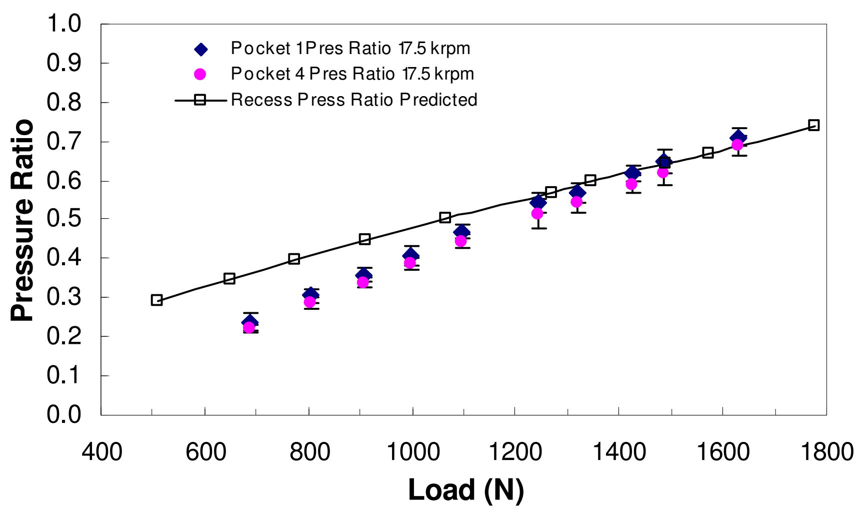

Figure 52: Pocket pressure ratios as a function of load for 17.24 bar thrust bearing supply pressure at 17.5 krpm rotor speed

Figure 53 show measured and predicted pressure ratios as function of center clearance for the supply pressure 17.24 bar at 17.5 rpm speed. The figure also show the measured Pocket 1 and Pocket 2 pressure ratios extracted from the static measurements of Forsberg [1], for the 17.24 bar TTB supply pressure case at 0 rpm speed. The comparison between the two sets of pressure ratio measurements show good agreement for test case clearance values equal and greater than the nominal clearance of 76.2 μm (low to mid loading). However, at zero speed test cases further decrease of clearances (high loading) was achieved exhibiting higher values of pressure ratios.

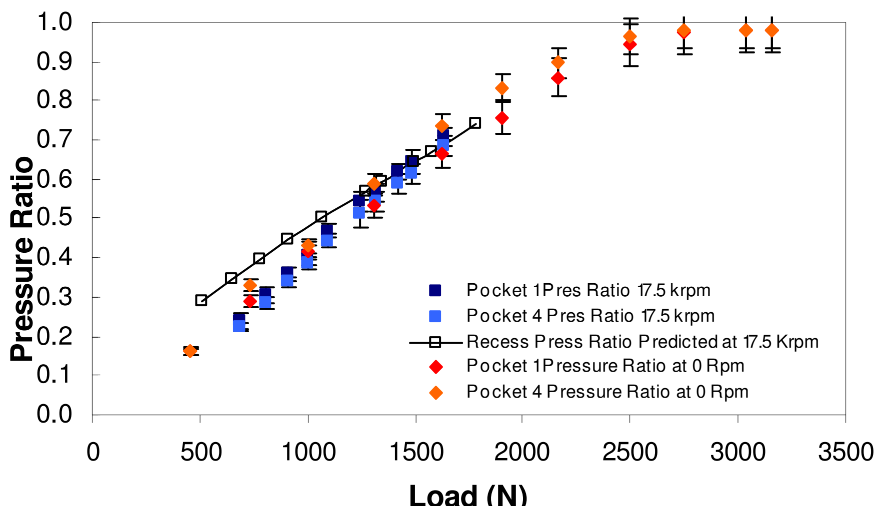

Figure 53: Comparison of pocket ratios as a function of load for 17.24 bar thrust bearing supply pressure at 17.5 krpm versus 0 Rpm rotor speed

The next parameter of interest is the loading versus clearance behavior of the TTB. Figures 54-62 show measured film center clearances of the test and slave thrust bearing as a function of axial load for the three supply pressures (3.45, 10.34, and 17.24 bar) at 7.5, 12.5, and 17.24 krpm rotational speeds, respectively. In general, the figures show load capacity increasing as clearance decreases. Also, the load capacity increases due to increase in pressure drop and rotational speed. All the clearance-versus-load figures show similar trends to those in San Andrés [3] as well as in Harada et al. [16].

Axial clearance measurements from the three proximity probes on each thrust bearing were used to derive the center clearance. For the TTB, the formula for the clearance at the center Z_c is shown in Eq. (1.10), and for the STB, the clearance at the

center, Z_{cslave} is shown in Eq. (1.11). The derivation for the thrust bearing centers can be found in Appendix E and F, respectively.

$$Z_c = (11.1Z_1 + 2.2Z_2 + 12.1Z_3) \qquad \textbf{(1.10)}$$

$$Z_{cslave} = (35.11Z_4 - 4.87Z_{10} - 4.86Z_9) \qquad \textbf{(1.11)}$$

where

Z_c = Clearance at the center of the TTB (mm)

Z_{cslave} = Clearance at the center of the STB (mm)

Z_1, Z_2, Z_3 = Gap readings from probe 1,2, or 3 of the TTB (mm)

Z_4, Z_9, Z_{10} = Gap readings from probe 4,9, or 10 of the TTB (mm)

Clearance uncertainties are also shown in the figures. The load uncertainties (of ~±10 N) are small and do not significantly alter the TTB load data. The average uncertainty for the measured TTB clearance for the entire test matrix is 5.85%. The minimum average uncertainty over a test load range is for the high-pressure/low-speed case (17.24 bar and 7.5 krpm, respectively) of 2.72%. The maximum average uncertainty over the test load range is for the high-pressure/high-speed case (17.24 bar and 17.5 krpm, respectively) of 7.21%. The measured STB clearance uncertainties are approximately 2 times larger than corresponding TTB clearance uncertainties. The discrepancy is due to the hydraulic cylinder's controller holding a set clearance for the TTB, while the fluid film clearance of the STB is not referenced by a feedback sensor. Additionally, the TTB clearance is held at the prescribed displacement at high precision, while the counteracting STB experiences the fluctuation of the axial static load.

Figures 54-56 represent a comparison between measurements and prediction for the load capacity of the 3.45 bar test and slave thrust bearing supply pressure at speeds of 7.5, 12.5, and 17.5 krpm. Experimental results for this low pressure case are in closer agreement with predictions at lower test thrust bearing clearance (high load) and as speed increases. Load predictions show a 13.7% to 21.2% average difference (over the speed range) when compared to the experimental results. The slave thrust bearing clearance is

nearly identical to the test thrust bearing clearance at the low pressure/low speed case, and generally decreases as supply pressure and rotational speed increase.

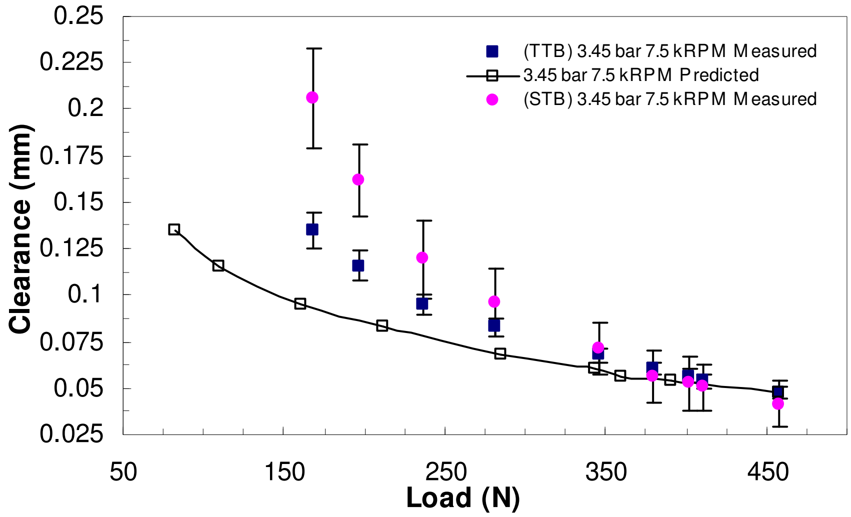

Figure 54: Comparison of measured and predicted center clearance versus load capacity for 3.45 bar thrust bearing supply pressure at 7.5 krpm rotor speed

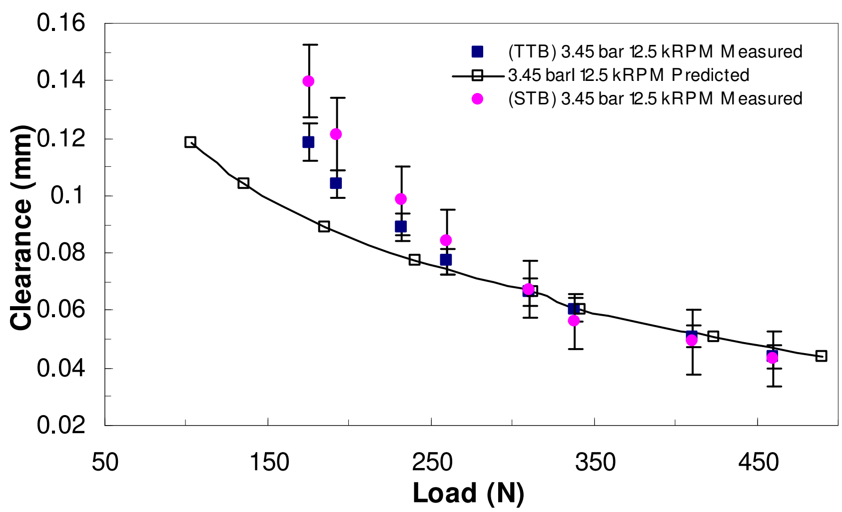

Figure 55: Comparison of measured and predicted center clearance versus load capacity for 3.45 bar thrust bearing supply pressure at 12.5 krpm rotor speed

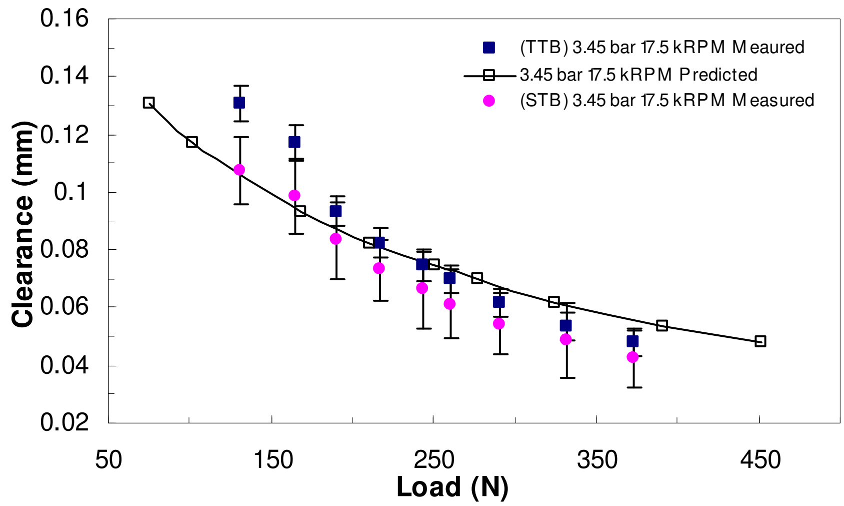

Figure 56: Comparison of measured and predicted center clearance versus load capacity for 3.45 bar thrust bearing supply pressure at 17.5 krpm rotor speed

Figures 57-59 present measurements and predictions of the load capacity for the 10.45 bar thrust bearing supply pressure cases at test speeds. Load prediction results show satisfactory agreement with experimental data (10.03% to 17.15% average difference) over the speed range, with improvement as rotational speed increases. Figures 60-62 show measurements and predictions of the load capacity for 17.24 bar TTB supply pressure cases at speeds. Load prediction results show good agreement with experimental data (6.93% to 9.98% average difference) over the speed range, with improvement as speed increases.

Overall, experimental load capacity results are in closer agreement with predictions at lower test thrust bearing clearance (high load) and as speed increases. Furthermore, at lower loads the measured clearances are larger than predicted, a similar trend to those noted by Etsion et al. [27].

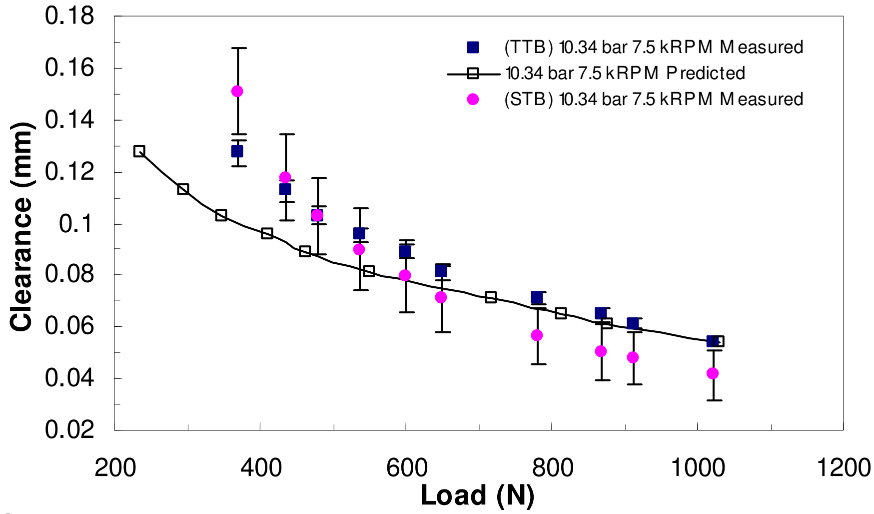

Figure 57: Comparison of measured and predicted center clearance versus load capacity for 10.45 bar thrust bearing supply pressure at 7.5 krpm rotor speed

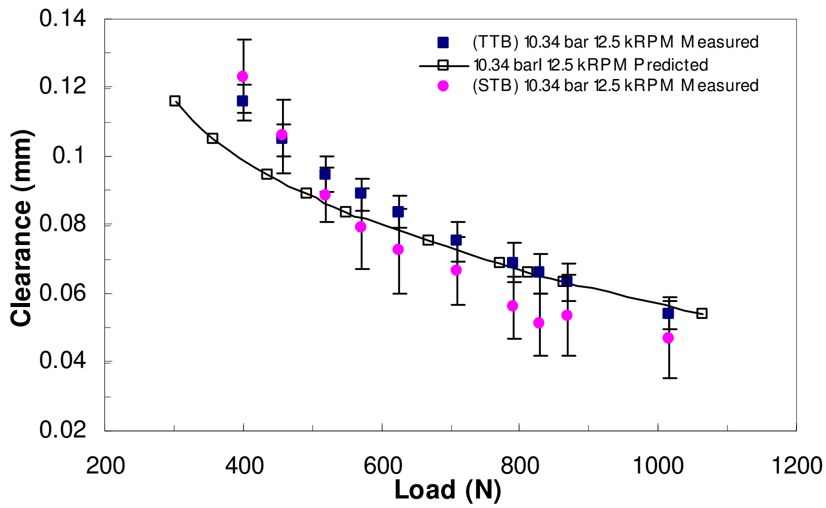

Figure 58: Comparison of measured and predicted center clearance versus load capacity for 10.45 bar thrust bearing supply pressure at 12.5 krpm rotor speed

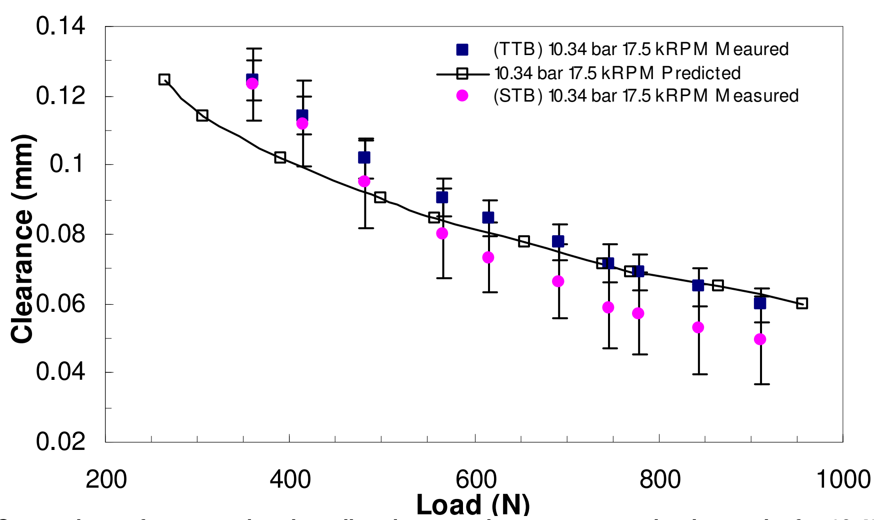

Figure 59: Comparison of measured and predicted center clearance versus load capacity for 10.45 bar thrust bearing supply pressure at 17.5 krpm rotor speed

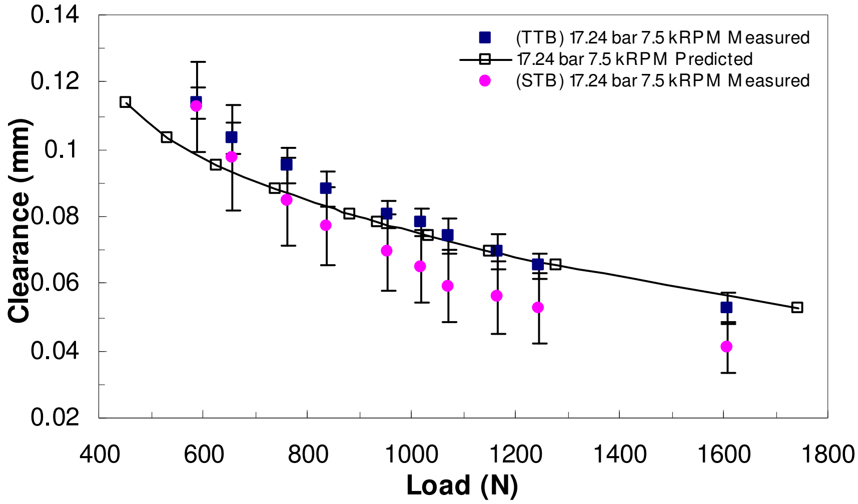

Figure 60: Comparison of measured and predicted center clearance versus load capacity for 17.24 bar thrust bearing supply pressure at 7.5 krpm rotor speed

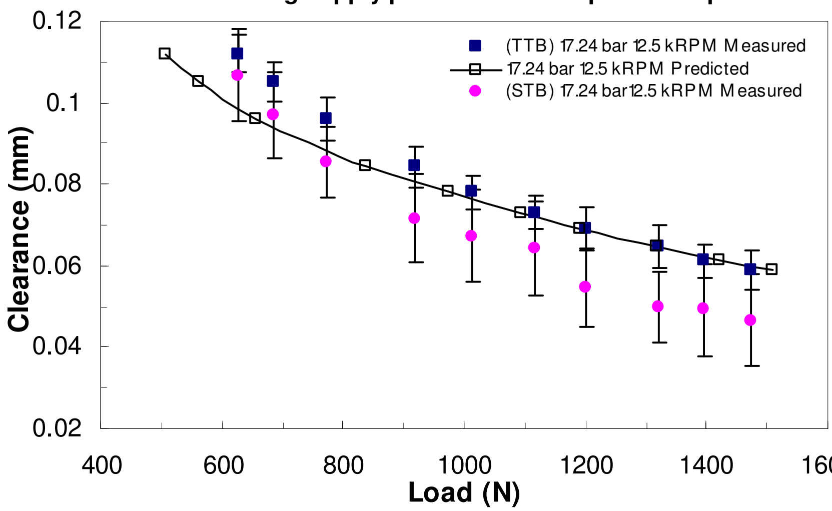

Figure 61: Comparison of measured and predicted center clearance versus load capacity for 17.24 bar thrust bearing supply pressure at 12.5 krpm rotor speed

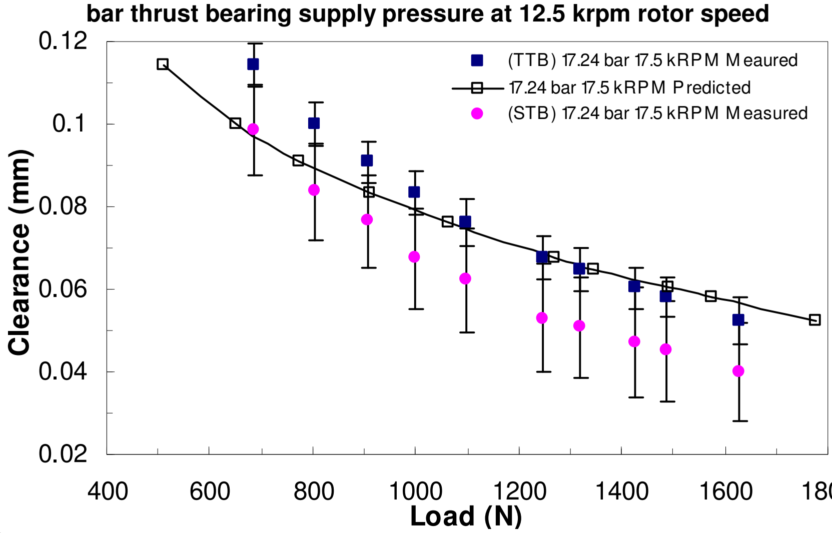

Figure 62: Comparison of measured and predicted center clearance versus load capacity for 17.24 bar thrust bearing supply pressure at 17.5 krpm rotor speed

Figure 63 show measurements and predictions of the load capacity for 17.24 bar TTB supply pressure at 17.5 rpm speed. The figure also show the measured and predicted load capacity, extracted from the static measurements of Forsberg [1], for the 17.24 bar TTB supply pressure case at 0 rpm speed. The comparison between the two sets of load capacity measurements show good agreement for test case clearance values equal and greater than the nominal clearance of 76.2 µm (low to mid loading). However, at zero speed test cases further decrease of clearances (high loading) was achieved.

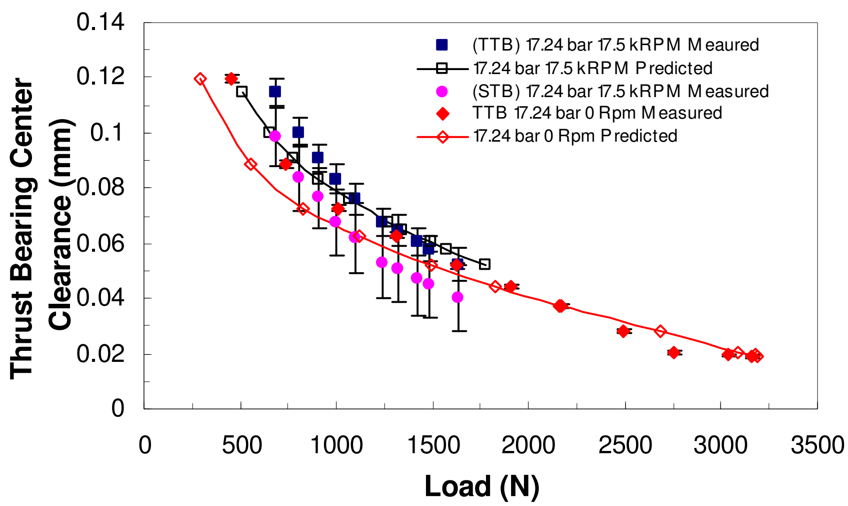

Figure 63: Comparison of measured and predicted center clearance versus load capacity for 17.24 bar TTB supply pressure at 0 Rpm (Forsberg [1]) and 17.5 krpm

The estimation of the overall stiffness (dF_z/dZ) is determined by differentiating the load-versus-clearance curves; due to the axial force (F_z) a function of axial center clearance (Z) and misalignment angles (δ_x, δ_y) of the test thrust bearing. Equation (1.12) shows the effective stiffness estimation equation.

$$\frac{dF_z}{dZ} = \left\{ \left(\frac{\partial F_z}{\partial Z} \right) + \left(\frac{\partial F_z}{\partial \delta_x} \right) \frac{\Delta \delta_x}{\Delta Z} + \left(\frac{\partial F_z}{\partial \delta_y} \right) \frac{\Delta \delta_y}{\Delta Z} \right\} \qquad \textbf{(1.12)}$$

where

F_z = Load on bearing face

δ_x, δ_y = Misalignment angles about x and y axis

Z = TTB center clearance

Figures 64-66 show curve fits of the load-versus-clearance data for the three pressure cases (3.45, 10.34, and 17.24 bar) over the speed range (7.5, 12.5, 17.5 krpm). A third-order polynomial is used to fit the data for each load series and was the lowest order to successfully capture the behavior of the clearance-versus-load curve with the smallest uncertainty. The figures show that the third-order curve fits the data well. Figures 65-66 show that the load capacity curve trends are nearly identical for the mid and high pressure cases over the low to high rotor speed range. Hence, these experimental results demonstrate that the static stiffness is usually insensitive to the rotational speed.

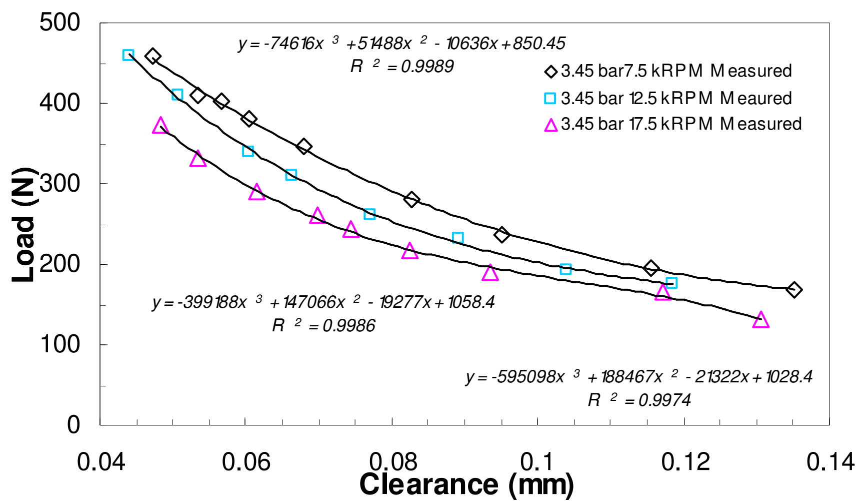

Figure 64: Clearance versus load measurements with third order polynomial curve fit for 3.45 bar test thrust bearing supply pressure. Curve fit equation shown for each speed test condition.

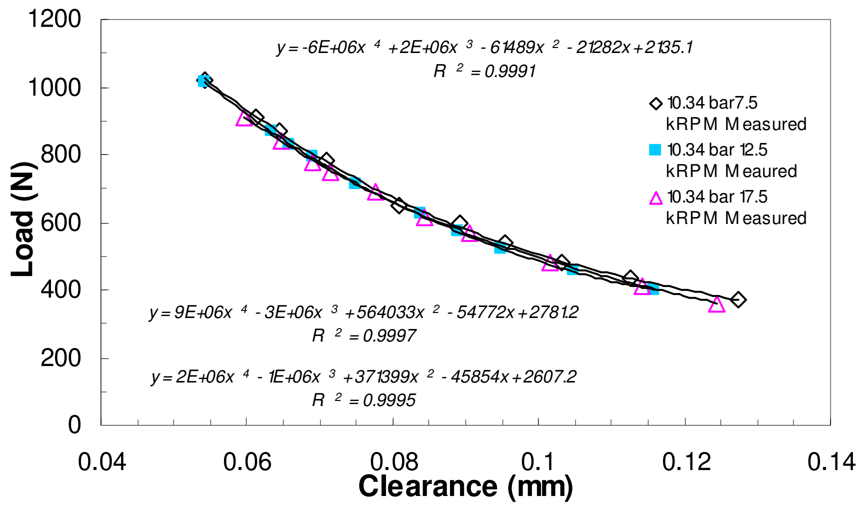

Figure 65: Clearance versus load measurements with third order polynomial curve fit for 10.45 bar test thrust bearing supply pressure. Curve fit equation shown for each speed test condition.

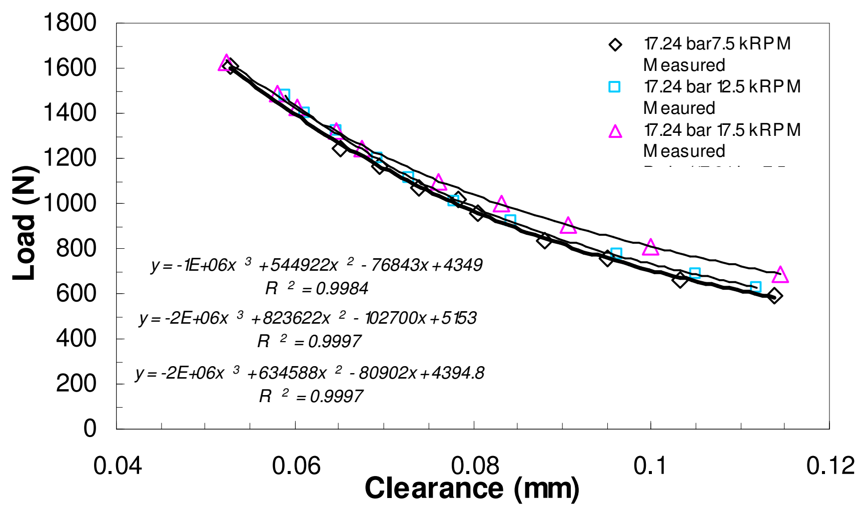

Figure 66: Clearance versus load measurements with third order polynomial curve fit for 17.24 bar test thrust bearing supply pressure. Curve fit equation shown for each speed test condition.

The thrust bearing effective axial stiffness can be estimated by differentiating the curve fit equation. The uncertainty of the stiffness estimation is also a significant parameter. The uncertainty of the curve fit was determined using Eq. (1.12) [1].

$$E_{dF/dZ} = \sqrt{E_A^2 + E_B^2 + E_C^2} \qquad \textbf{(1.12)}$$

Where

$Load = A * Z_C^3 + B * Z_C^2 + C * Z_C + D$

E_N = Uncertainty associated with term N

Z_C = Test thrust bearing center clearance

The uncertainty from each term of the curve fit was found using the TableCurve2D program. The commercial program provided a means to check the curve fits from Excel and produced an uncertainty associated with each of the terms. Please note, fifteen readings were taken for each data point shown in Figures 64-66. The standard deviation of TTB center clearance (*Z*) were the predominant uncertainty value propagated to the uncertainty of the curve-fits which is the uncertainty of the axial stiffness estimation.

Figures 67-69 show the curve-fit differentiation estimation, or overall stiffness dF_z/dZ. The estimated stiffness increases as axial load increases (decreasing clearance). Again, the measurements demonstrate that the stiffness is insensitive to the speed for the supply pressure cases of 3.45, 10.34, and 17.24 bar, respectively. Although, there is a slight trend deviation of the low-pressure/high-speed case (3.45 bar and 17.5 rpm, respectively) as shown in Figure 67.

The uncertainties, shown in Figures 67-69, are large for the estimated axial stiffness versus measured center clearance. Figure 67 shows the 3.45 bar case, and average uncertainty over the speed range is 27.1 % to 40.2 %, increasing with rotational speed. Figure 68 shows the 10.34 bar case, and the average uncertainty over the speed range is 31.6% to 46.13%, increasing with rotational speed. The largest uncertainties for the estimated axial stiffness occur for the 17.24 bar case; the discrepancy is attributed to the propagated error of calculated center clearance using large-uncertainty measurements of the three proximity probes on the TTB.

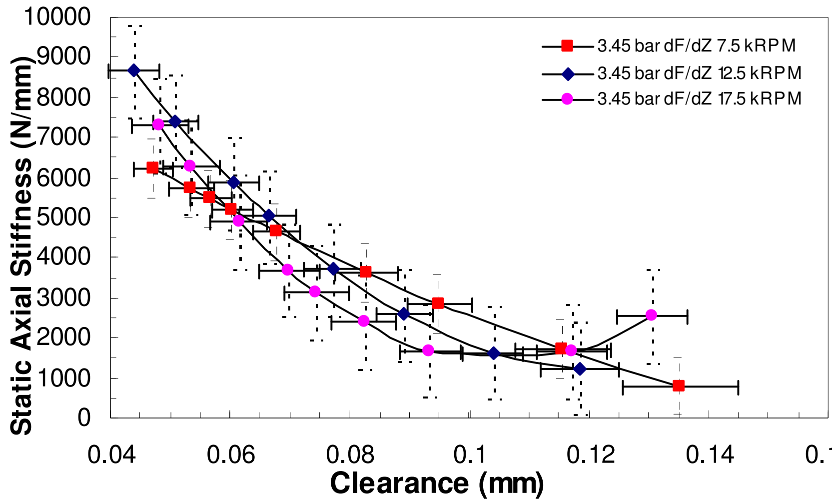

Figure 67: Derived static axial stiffness from experimental results versus clearance for 3.45 bar test thrust bearing supply pressure at 7.5, 12.5, and 17.5 rotor speeds

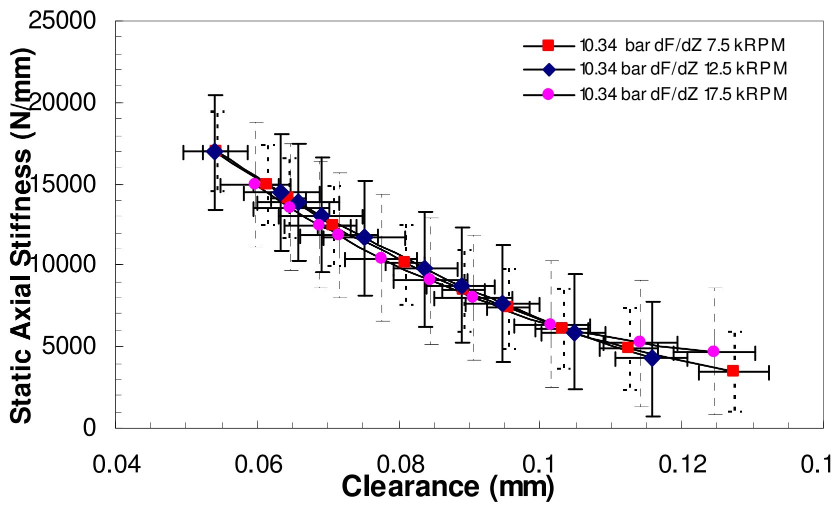

Figure 68: Derived static axial stiffness form experimental results versus clearance for 10.45 bar test thrust bearing supply pressure at 7.5, 12.5, and 17.5 rotor speeds

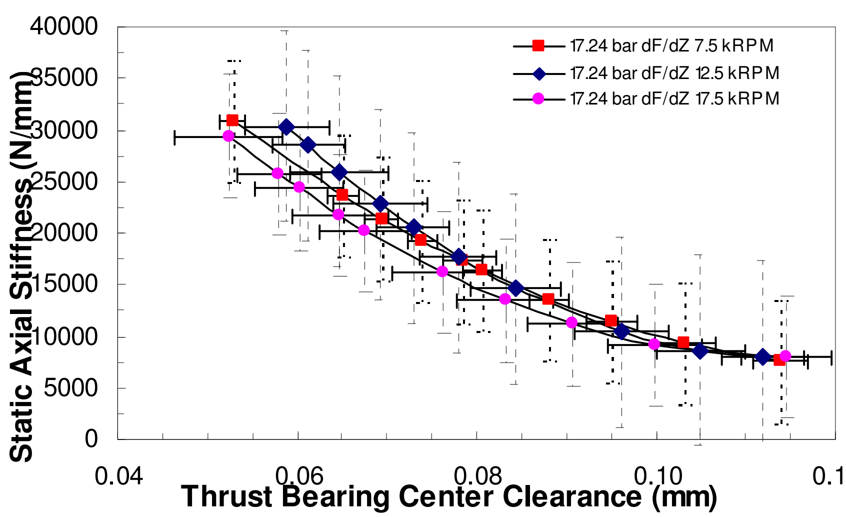

Figure 69: Derived static axial stiffness from experimental results versus clearance for 17.24 bar test thrust bearing supply pressure at 7.5, 12.5, and 17.5 rotor speeds

Figure 70 shows the curve-fit differentiation estimation, or overall axial stiffness dF_z/dZ, based on load capacity and clearance measurements, for 17.24 bar TTB supply pressure at 7.5, 12.5, and 17.5 rpm speed. The figure also shows the stiffness estimation, extracted from the static measurements of Forsberg [1], for the 17.24 bar TTB supply pressure case at 0 rpm speed. The comparison between the two sets of dF_z/dZ show good agreement for test case clearance values equal and greater than the nominal clearance of 76.2 μm (low to mid loading). However, at zero speed test cases further decrease of clearances (high loading) was achieved confirming a maximum stiffness at a certain load.

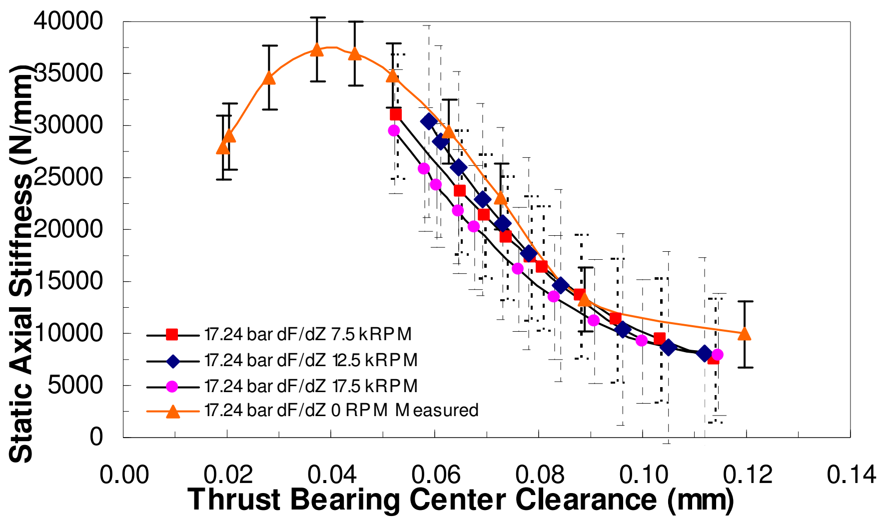

Figure 70: Comparison of derived static axial stiffness from experimental results versus clearance for 17.24 bar TTB supply pressure at 7.5, 12.5, and 17.5 krpm versus 0 rpm case (Forsberg [1])

INITIAL INVESTIGATION FOR AN AXIAL RESONANCE

High sampling rate measurements were conducted for a select number of rotating test conditions within the limitations of the Hybrid Thrust Bearing Test Rig. The dynamic axial measurements obtained were of the six axial proximity probes on the test and slave thrust bearings and two pair sets of the radial proximity probe. The following are FFT results corresponding to the measure of axial displacement of either probe 2 on the test thrust bearing (TTB) or probe 4 of the slave thrust bearing (STB). Also, the maximum rotational speed is 19krpm (drive motor is operating at 100% rated load capacity). The objective of this investigation is to look for resonance of the thrust and rotor system.

HIGH SAMPLING RATE MEASUREMENT TEST PROCEDURE

The dynamic data are displayed in real-time on a Labview virtual instrument, which includes the minimum clearance, average clearance and *x* and *y* axis misalignment slopes of the TTB and STB faces using dual PCI-4772 DAQ boards. High frequency sampling may be conducted primarily for all proximity probes, running speed, and axial load cell readings. Figure 71 shows the dynamic measurement display. Table 6 contains a summary of the specification for the dynamic DAQ boards.

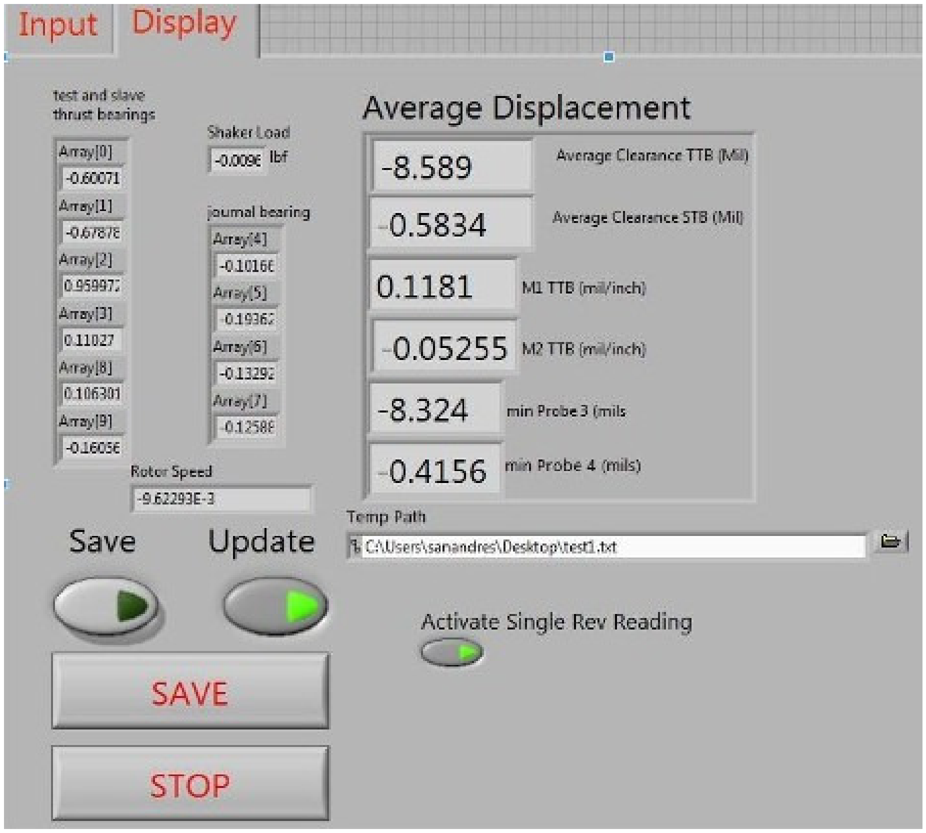

Figure 71: Real-time diagnostic Labview VI for dynamic data logging

Table 6: Listing of dynamic DAQ board specifications[28]

Board Type	Number of Channels	Sampling Rate (Ksamples/sec)	Resolution (bits)	Signal Range (V)	Signal Type	Connection
PCI-4472	16	102.4 per input	24	±10	Analog/Digital Input/Output Analog Input used	SMB-120 cable

The dynamic test sequence involves the axial measurements of the six axial proximity probes on the TTB and STB. An FFT of the results provides a frequency decomposition of axial motion at the thrust bearings. Using the two PCI-4472 DAQ board, 5k samples over a sampling rate of 33.33 kHz are taken for proximity probe measurement. Again, the objective of this test is to look for conditions of resonance of the thrust and rotor system. The test consists of two selected test conditions: (1) rotational speed is held at 19 krpm and clearance held at 76.2 μm (at increments of 0.34 bar) the thrust bearing supply pressure is decreased from 17.24 to 3.45 bar, and (2)

rotational speed is held at 19 krpm and clearance held at 127 µm (at increments of 0.34 bar) the thrust bearing supply pressure is decreased from 17.24 to 3.45 bar.

HIGH SAMPLING RATE MEASUREMENT RESULTS

Predicted damped natural frequencies were calculated using a simple 2-DOF model of the thrust and rotor system provided by San Andrés [29], and depicted in Figure 72. Inputs to the model are predicted dynamic coefficients of the thrust bearing [direct axial stiffness (Kz), damping (Cz), and mass (M)] from XLHydroTHRUST®. Also, another input for the model is mass parameters of the thrust system: thrust bearing and housing, and test rotor as shown in Appendix B and Table 2, respectively. XLHydroTHRUST® input specification are shown in Table 7. The discharge coefficient used is the average from the empirical coefficient calculated from the static result sets of the current test rig.

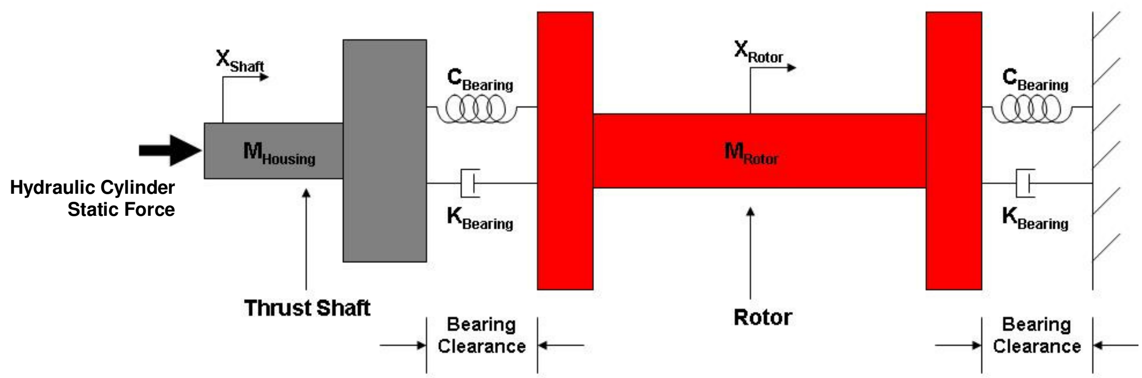

Figure 72: 2 DOF system with two translations of the thrust rotor-system (including stinger mass)

Table 7: Operating conditions of static and rotor dynamic performance using XLHydroTHRUST®

Parameter	Value (unit)
Bearing fluid	Water
Temperature	93.4 ºF (34 ºC)
Viscosity, µ	.503 cPoise (1.05e-5 lb_f-s/ft^2)
Density, ρ	984.33 kg/m^3 (61.45 lb/ft^3)
Orifice Discharge Coefficient, C_d	.585
Avg. Fixed clearance from FFT DC Offset	75.69 and 121.67 µm

Figure 73 shows the predicted damped natural frequencies as a function of thrust bearings supply pressure for two clearance cases of 76.2 and 127 μm. The figure was used to investigate resonant conditions exemplified by the FFT of experimental results. Note the high damping ratios on Figure 73 of each of the well-damped natural frequencies.

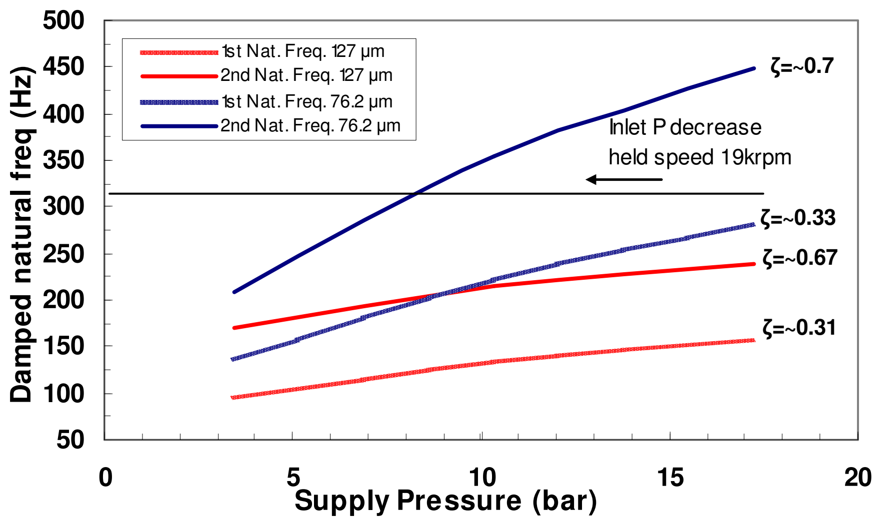

Figure 73: Predicted natural frequencies of the thrust rotor-system at two clearances (76.2 and 127 μm)

The following plots are FFT results corresponding to the measure of axial displacement of either probe 2 on the TTB or probe 4 of the STB. Figure 74 depicts the TTB FFT spectrum of amplitude versus supply pressure for the held-clearance cases of 76.2 μm and rotational speed of 19 krpm. The peaks represent the frequency decomposition amplitude at inlet pressures incremented by .34 bar over the range 3.45 to 17.24 bar. 1X (synchronous amplitudes) and higher harmonics are illustrated in the figure at a frequency of 320.1 Hz. Average approximated amplitude is 3.56 μm, with slight deviation. According to Figure 73, critical speeds crossover occurs at a single case (2^{nd} damped natural frequency) at a supply pressure of ~8.27 bar. Maximum amplitudes response was found at the 7.93 bar and 15.17 bar supply pressure case; but only a small deviation from synchronous motion at other pressure cases. Therefore, a resonance

response was not observed. Figure 75 depict the STB FFT spectrum for the aforementioned case. Amplitude response is nearly identical to that of the test bearing.

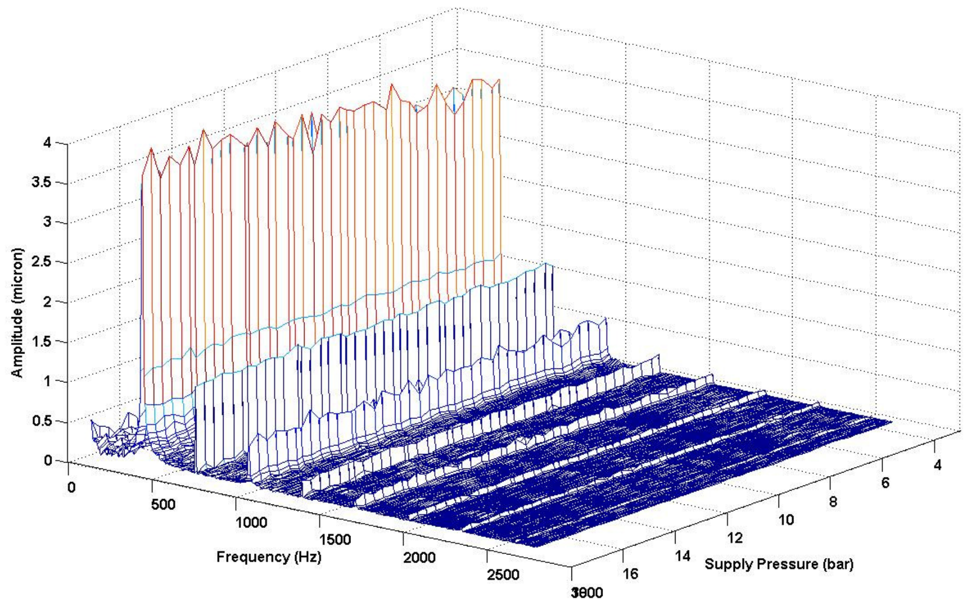

Figure 74: FFT spectrum of the test thrust bearing (probe 2): amplitude versus thrust bearing supply pressure for the 76.2 µm clearance and 19 krpm rotational speed case. (1X) amplitude shown in red at 320.1 Hz

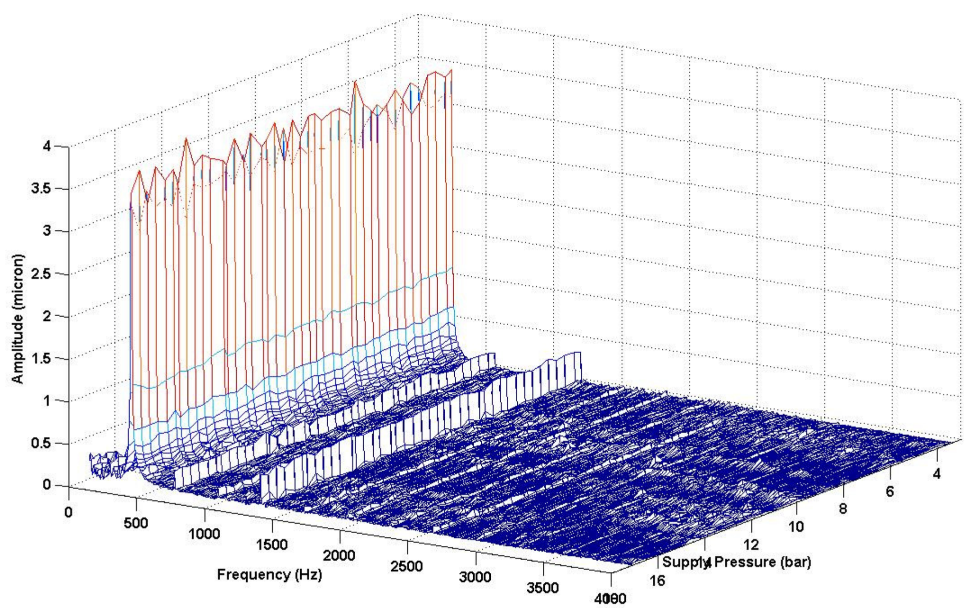

Figure 75: FFT spectrum of the slave thrust bearing (probe 4): amplitude versus thrust bearing supply pressure for the 76.2 µm clearance and 19 krpm rotational speed case. (1X) amplitude shown in red at 320.1 Hz

Figure 76 depicts the TTB FFT spectrum of amplitude versus supply pressure for the held-clearance cases of 127 μm and rotational speed of 19 krpm. The peaks represent the frequency decomposition amplitude at inlet pressures incremented by .34 bar over the range 3.45 to 17.24 bar. 1X synchronous amplitudes and higher harmonics are illustrated in the figure at a frequency of 320.1 Hz. Average approximated amplitude is 3.3 μm, with slight deviation. According to Figure 73, for this case, resonance crossover does not occur; 1st and 2nd damped natural frequencies are low and were avoided. Maximum amplitude response was found at the 10.34 bar supply pressure case; but overall synchronous amplitude are small (~3.3 μm). Therefore, a resonant response was not observed. Figure 77 depict the STB FFT spectrum for the aforementioned case. Amplitude response is nearly identical to that of the test bearing.

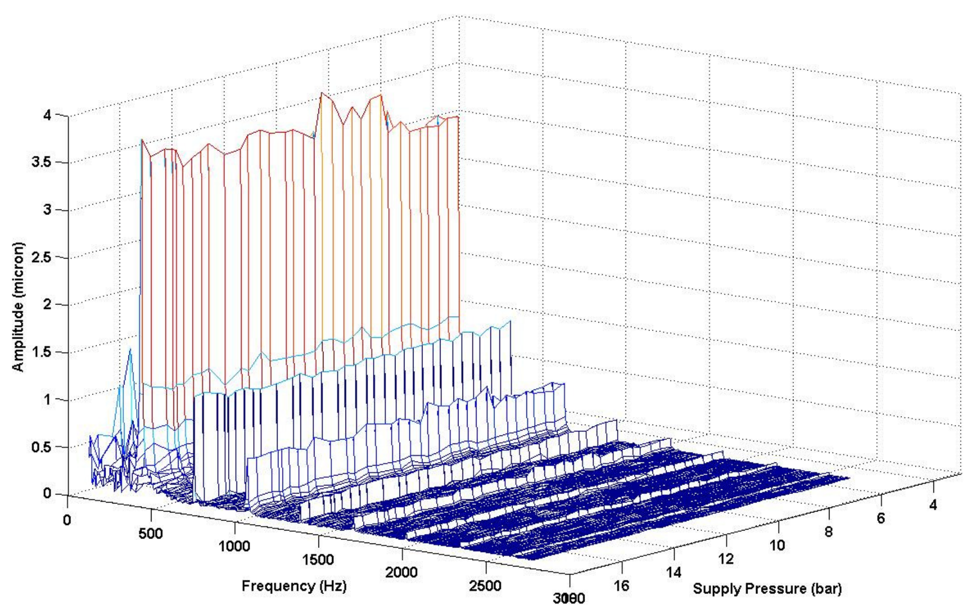

Figure 76: FFT spectrum of the test thrust bearing (probe 2): amplitude versus thrust bearing supply pressure for the 127 μm clearance and 19 krpm rotational speed case. (1X) amplitude shown in red @ 320.1 Hz

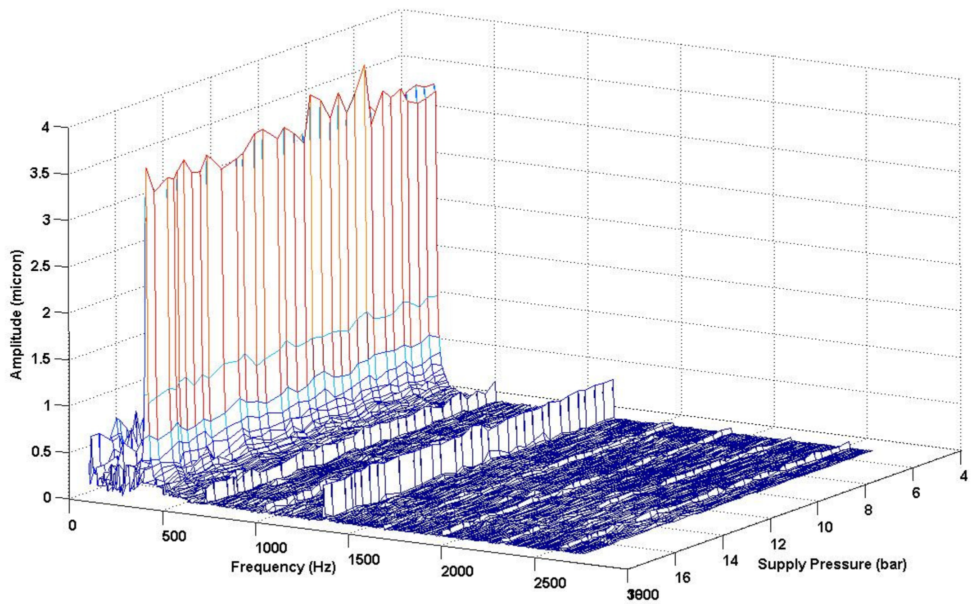

Figure 77: FFT spectrum of the slave thrust bearing (probe 4): amplitude versus thrust bearing supply pressure for the 127 m clearance and 19 krpm rotational speed case. (1X) amplitude shown in red at 320.1 Hz

CONCLUSIONS

A face-to-face style test rig was designed and built for testing hybrid thrust bearings. Using this test rig a hybrid thrust bearing was tested under rotating conditions. These test results were compared to predictions for flow rate, load, and axial stiffness from the XLHydroTHRUST® program. Predictions correlated reasonably well for flow and load. The experimental results are in closer agreement with theoretical predictions at higher supply pressures, and at lower clearances tested. For the nominal high-pressure/high-speed case of (17.24 bar and 17.5 krpm), inlet flow rate predictions show very good agreement with measured data of 1.0% average difference over the loading range. Inner-radius discharge flow rate predictions show a 5.0% average difference. Additionally, measurements of flow rate through the inner radius of the TTB evidences the onset of starvation (sub-ambient pressures) of the fluid film across the land for a high-speed and low-load condition due to centrifugal acceleration of the fluids. Also, for the nominal high-pressure/high-speed case, load versus clearance predictions show good agreement with experimental data (6.9% average difference) over the load range. Total axial stiffness was estimated by differentiating the clearance-versus-load curves yielding large uncertainty due to the propagated uncertainty of calculated center clearance (5.9% average) which used large uncertainty measurements of the three proximity probes on the test thrust bearing. For the nominal supply pressure case (17.24 bar), pocket-1 pressure ratio predictions (nearly the same as pocket 4) show good agreement with measurements (8.6% to 13% average difference) over the speed range, with improvement as speed increases.

Also, measurements of the performance characteristics of the turbulent hybrid thrust bearing with rotor spinning were compared to those measured by Forsberg [1] at 0 rpm rotational speed. The comparison between the two sets of static measurements show good agreement for test case clearance values equal and greater than the nominal clearance of 76.2 μm (low to mid loading). However, Forsberg [1] measurements

contain a wider load range testing a further decrease of clearances (high loading) at 0 rpm rotational speed.

Finally, dynamic axial measurements of the fluid film clearance of the test thrust bearing are presented. This investigation of resonant conditions of the thrust rotor-system, based on FFT spectrum of measured axial shaft motion at the free and drive end thrust collars of the test rotor, evidence no resonance. The inability to detect the resonance might be due to: (i) the large predicted damping values for the mode of interest, (ii) the position-control mode of the hydraulic cylinder that might be suppressing vibration, or (iii) the absence of misalignment of the bearings that eliminated an excitation for the mode. Shake testing of the rig would locate the resonance and eliminate the uncertainty.

REFERENCES

[1] Forsberg, M., (2008), "Comparison Between Predictions and Experimental Measurements for an Eight Pocket Annular Hydrostatic Thrust Bearing," final report, Texas A&M University, May-College Station, TX

[2] Hibbs, R., Scharrer, J.K., and Molvik, G.L., (1996), "Turbulent Hydrostatic Thrust Bearings. I – Bulk-flow Analysis for Performance and Pneumatic Hammer," AIAA Meeting Papers, July, AIAA Paper 96-2741

[3] San Andrés, L., (2000), "Bulk Flow Analysis of Hybrid Thrust Bearing for Process Fluid Applications." ASME Trans., *Journal of Tribology*, January, Vol. 122 (1), pp. 170-180

[4] Nellis, G.F., Zagarola, M.V., and Sixsmith, H., (2001), "Analysis and Test of a Robust Sector Thrust Bearing for a Cryogenic Turboalternator," *ASME Journal of Tribology*, Vol. 123**,** pp. 768-776

[5] San Andrés, L., (2006), "MEEN 626 Notes 2 Derivation of the Classical Reynolds Equation for Thin Film Flows (Continued)," pg. 15

[6] San Andrés, L., (2002), "Effects of Misalignment on Turbulent Flow Hybrid Thrust Bearings," ASME Trans., *Journal of Tribology*, January, Vol. 124, pp. 212-219

[7] Elwell, R.C. and Sternlicht, B., (1960), "Theoretical and Experimental Analysis of Hydrostatic Thrust Bearings," ASME Trans., *Journal of Basic Engineering*, September, Vol. 82, 3, pp. 505-512

[8] Pinkus, O., and Lund, J.K., (1981), "Centrifugal Effects in Thrust Bearings Under Laminar Conditions," ASME Trans., *Journal Lubrication Technology*, Vol. 103, pp.126-136

[9] Hashimoto, H., (1990), "The Effects of Fluid Inertia Forces on the Static Characteristics o Sector-Shaped High Speed Thrust Bearings in Turbulent Flow Regime," ASME Trans., *Journal of Tribology*, Vol. 111, pp. 406-411

[10] Safar, Z.S., (1983), "Centrifugal Effects in Misaligned Hydrostatic Thrust Bearings," ASME Trans., *Journal of Tribology*, October, Vol. 105, pp. 621-624

[11] Dowson, D., (1961), "Inertia Effects in Hydrostatic Bearings," ASME Trans., *Journal of Basic Engineering*, Vol. 83, pp. 227-234

[12] New, N. H., (1974), "Experimental Comparison of Flooded, Directed, and Inlet Orifice Type of Lubrication for a Tilt Pad Thrust Bearing." ASME Trans., *Journal of Lubrication Technology*, Vol. 96, No. 1, pp 22-27

[13] Gregory, R. S., (1974), "Operating Characteristics of a Fluid-Film Thrust Bearing Subjected to High Shaft Speeds." *Journal of Lubrication Technology*, Vol. 96, No. 1, pp. 7-14

[14] Neal, P. B., (1982), "Heat Transfer in Pad Thrust Bearings." *Proceedings of the Institution of Mechanical Engineers*, September, Vol. 196, pp. 217-228

[15] Horner, D., Simmons, J. E. L., and Advani, A. D., (1986), "Measurements of Maximum Temperature in Tilting-Pad Thrust Bearings." *ASLE Preprints*, pp. 1-10

[16] Harada, M., Miyaji, R., and Anada, Y., (1987), "Turbulent Lubrication for a Hydrostatic Thrust Bearing with A Circular Recess," *JSME International Journal*, Vol. 30, No. 269, pp. 1819-1825

[17] Glavatskih, S. B. and DeCamillo, S., (2004), "Influence of Oil Viscosity Grade on Thrust Pad Bearing Operation." ASME Trans., *Journal of Engineering Tribology*, Vol. 218, No. 5, pp 401-412

[18] San Andrés, L., (2006), "MEEN 626 Notes 12 Annular Seals and Hydrostatic Journal Bearings," pg. 17, <http://phn.tamu.edu/me626/Notes_pdf/Notes12_Seals_HJBs.pdf>

[19] Al-Ghasem, A. and Childs, D., (2005), "Rotordynamic Coefficients Measurements versus Predictions for a High Speed Flexure-Pivot Tilting-Pad Bearing (Load-Between-Pad Configuration)," *Proceedings of the ASME Turbo Expo*, June, Vol. 4, pp.725-736

[20] Rodriquez, L.E., and Childs, D.W., (2006), "Frequency Dependency of Measured and Predicted Rotordynamic Coefficients for a Load-on-Pad Flexible-Pivot Tilting-Pad Bearing," ASME Trans., *Journal of Tribology*, April, Vol. 128, pp. 388-395

[21] National Instruments "Low-Cost M Series Multifunction DAQ – 16-Bit, 250 kS/s, up to 80 Analog Inputs" October 20, 2007. <http://www.ni.com/pdf/products/us/20044546301101dlr.pdf>

[22] San Andrés, L., (2001), "Computational Analysis of Misaligned Hybrid Thrust Bearings for Advanced Cryogenic Turbo Pumps," final progress report to NASA MSFC, Texas A&M University, January-College Station, TX

[23] Munson, Bruce, R., Young, D.F., and Okiishi, T.H., (2002), "Fundamentals of Fluid Mechanics," John Wiley & Sons, pp. 513-516

[24] Kurtin, D.A., Childs, D.W., San Andrés, L., and Hale, K., (1993), "Experimental Versus Theoretical Characteristics of a High-Speed Hybrid (combination Hydrostatic and Hydrodynamic) Bearing," ASME Trans., *Journal of Tribology*, January, Vol. 115, pp. 160-169

[25] Mosher, P., and Childs, D.W., (1995), "Theory Versus Experiment For The Effects of Pressure Ratio On The Performance of An Orifice-Compensated Hybrid Bearing," Design Engineering Technical Conference, September, Vol. 84-2, pp. 1119-1129

[26] San Andrés, L., (1997), "Angled Injection-Hydrostatic Bearings Analysis and Comparison to Test Results," ASME Trans., *Journal of Tribology*, January, Vol. 119, pp. 179-187

[27] Etsion, I., Halperin, G., Brizmer, V., and Kligerman, Y., (2004), "Experimental Investigation of Laser Surface Textured Parallel Thrust Bearings," *Tribology Letters*, August, Vol. 17, No. 2, pp. 295-300

[28] National Instruments "NI 4472 Series – 24-Bit, 102.4 kS/s, 8- and 4-Channel Dynamic Signal Acquisition" May 12, 2008. <http://www.ni.com/pdf/products/us/3sv414-416.pdf>

[29] San Andrés, L., (2006), "2-DOF Model for Thrust Bearing Housing and Rotor Assembly," June, personnel correspondence for the USET Northrop Grumman hybrid thrust bearing test rig project

[30] SKF "Eddy Probe Systems Catalog" pg 5-8 October 20. 2007 <http://www.stiweb.com/downloadDataSheets/eddyprobe.pdf>

[31] Coleman, Hugh W. and Steele, W Glenn Jr., (1989), "Experimentation and Uncertainty Analysis for Engineers," John Wiley and Sons, pp 89-100, pp. 172-174

APPENDIX A –

Flow loop schematic with instrumentation included

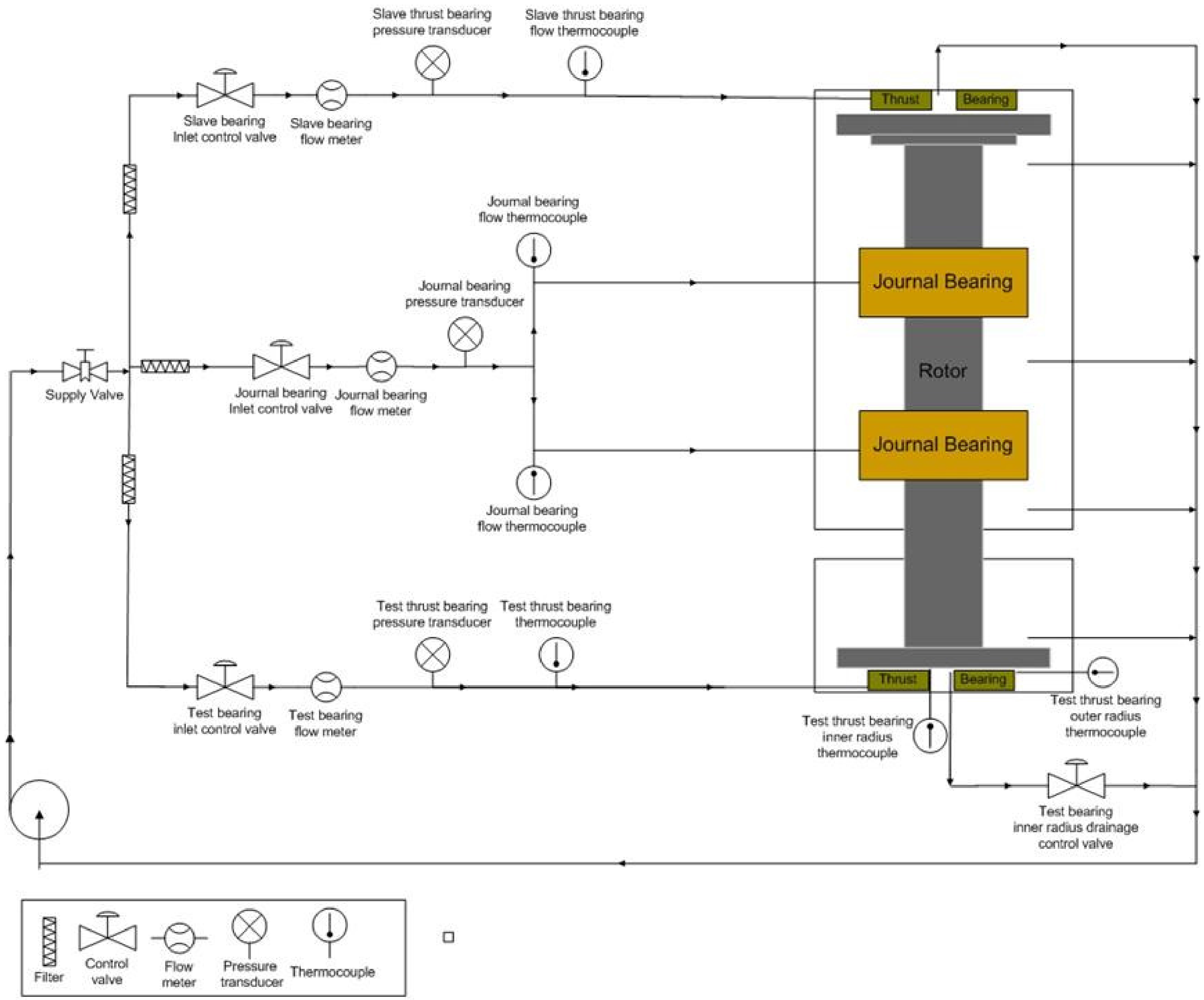

Figure 78: Hybrid thrust bearing test rig flow loop with select instrumentation locations included

APPENDIX B –

Bearing dimensions and physical parameters of hybrid thrust bearing test rig

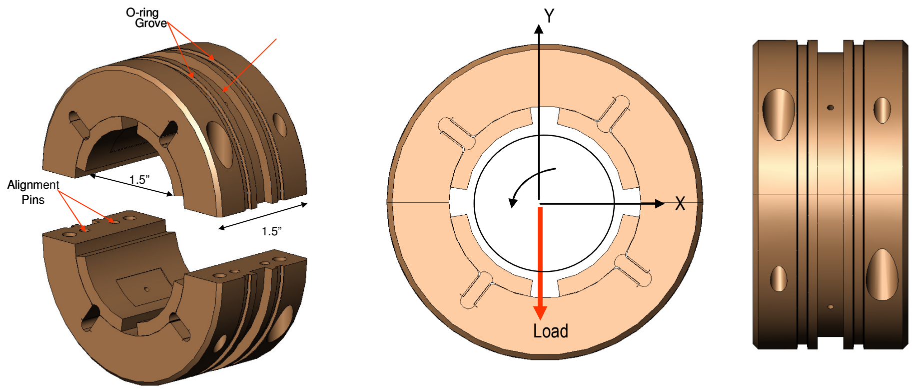

Figure 79: Depiction of radial hybrid bearings

Table 8: Dimensions and physical parameters of hybrid radial bearings (flexure pivot type and made of bearing bronze)

Nominal	Radial clearance	76.2 μm (3 mil)
Bearing	Inner Diameter	38.1 mm (1.5 inch)
	Outer Diameter	76.2 mm (3 inch)
	Length	38.1 mm (1.5 inch)
Pads	Number of pads	4
	Arc length	72 °
	Pivot offset (dim)	60% arc length
	Preload (dim)	0.20
	Flexure rotational stiffness	199.97 N-m/rad (1,770 lb_f-in/rad)
Pocket one per pad	Axial length	12.7 mm (0.50 inch)
	Arc length	24 °
	Depth	.508 mm (20 mil)
	Mean Diameter	54.864 mm (2.16 inch)
	Pocket/wetted area ratio	0.11
	Inlet coefficient from pocket to land	0.20
Orifice one per pocket	Diameter	1.702 mm (0.067 inch)
	Radial injection	50% of pocket length
	Entrance Loss Coefficient	0.80
Web	Radial width	3.56 mm (0.140 inch)
	Axial width	3.81 mm (0.150 inch)
	Length (radius-to-radius)	6.38 mm (0.251 inch)
	Radius	20.32 mm (0.80 inch)

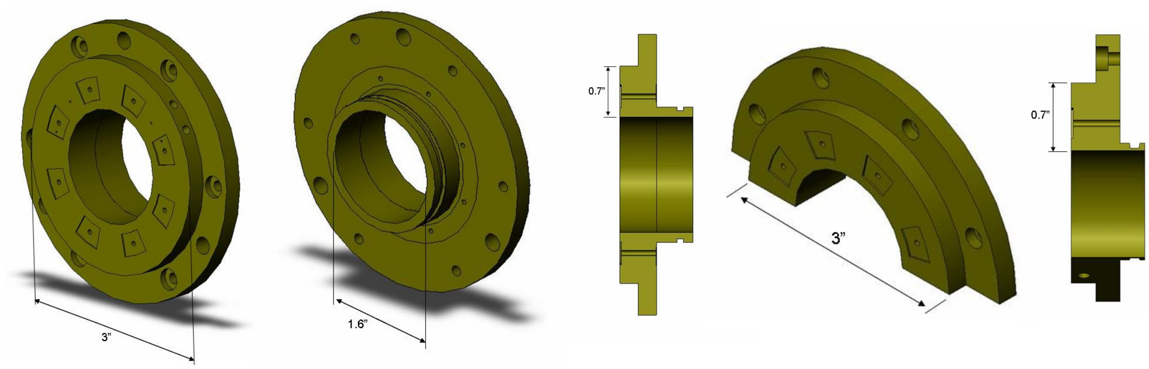

Figure 80: Depiction of test thrust bearing (front and back sides, cross-section) shown on left and of (half) slave thrust bearing show on right

Table 9: Dimensions and physical parameters of hybrid thrust bearings (made of tin bearing bronze)

Nominal	Axial clearance	76.2 μm (3 mil)
Thrust Face	Inner Diameter	40.64 mm (1.6 inch)
	Outer Diameter	76.2 mm (3 inch)
	Flange Outer Diameter	98.425 mm (3.875 inch)
Pocket	Number of Pockets	8
	Arc length	20 °
	Radial Length	8.128 mm (0.32 inch)
	Depth	.508 mm (20 mil)
	Mean Diameter	54.864 mm (2.16 inch)
	Pocket/wetted area ratio	0.21
	Inlet loss coefficient from pocket to land	0.20
Orifice	Diameter	1.803 mm (0.071 inch)
One per pocket	Radial location	27.432 mm (1.08 inch)
	Entrance Loss Coefficient	0.80

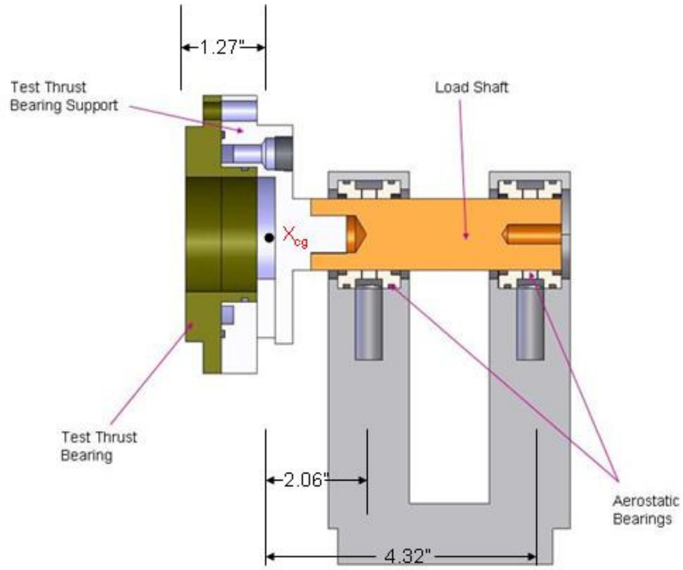

Figure 81: Cross-sectional view of load shaft, test thrust bearing and aerostatic bearings

Table 10: Physical parameters for support of test thrust bearing

Assembly (thrust bearing support and load shaft)	Mass	17.8 N (4 lb)
	Transverse Moment of Inertia	25.31 kN-m^2 (8.82 lb-in^2)
Distances	Thrust Face to CG of assembly	32.26 mm (1.27 inch)
	Left Bearing to CG	52.32 mm (2.06 inch)
	Right Bearing to CG	109.73 mm (4.32 inch)

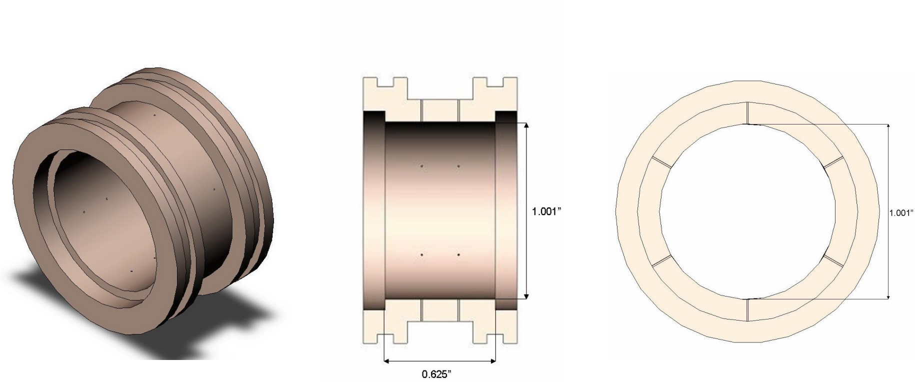

Figure 82: View of aerostatic bearing (3d, side and front cross sections)

Table 11: Dimensions of aerostatic bearings, force coefficients and lateral natural frequencies of TB section and axial load shaft (material: tin bearing bronze)

AEROSTATIC BEARINGS		**Supply Pressure: 6.89 bar (100 psig)**
Radial Clearance	12.7 µm (0.5 mil)	
Diameter	25.654 mm (1.01 inch)	
Axial Length	15.875 mm (0.625 inch)	
Number of holes	12	
Hole Diameter	.254 mm (0.010 inch)	C_d=0.86
Hole Pattern	Double Row, 6 per row	2.642 mm (0.104 inch) from midplane
	Left Bearing	**Right Bearing**
Static load	27.85 N (6.26 lb)	10.14 N (2.28 lb) (up)
Static displacement	2.794 µm (0.110 mil)	.99 µm (0.039 mil) (up)
Mass Flow	$1.25\text{x}10^{-4}$ $^{kg}/_{s}$ ($2.76\text{x}10^{-4}$ $^{lb}/_{s}$)	$1.27\text{x}10^{-4}$ $^{kg}/_{s}$ ($2.81\text{x}10^{-4}$ $^{lb}/_{s}$)
Pressure Ratio $(P_{max}-P_{atm})/(P_{supply}-P_{atm})$	0.77	0.50
Vertical motions		
Stiffness (K_{xx})	9911.7 $^{N}/_{mm}$ (56.6 $^{lb}/_{mil}$)	10139.3 $^{N}/_{mm}$ (57.9 $^{lb}/_{mil}$)
Damping (C_{xx})	518.35 $^{N*s}/_{m}$ (2.96 $^{lb*s}/_{in}$)	351.99 $^{N*s}/_{m}$ (2.01 $^{lb*s}/_{in}$)
Natural frequency & Damping ratio	196 Hz 3.1%	1,000 Hz 16 %
Horizontal motions		
Stiffness (K_{yy})	10156.84 $^{N}/_{mm}$ (58.0 $^{lb}/_{mil}$)	10191.87 $^{N}/_{mm}$ (58.2 $^{lb}/_{mil}$)
Damping (C_{yy})	374.75 $^{N}/_{m}$ (2.14 $^{lb*s}/_{in}$)	336.23 $^{N}/_{m}$ (1.92 $^{lb*s}/_{in}$)
Natural frequency & Damping ratio	199 Hz 2.3 %	1,016 Hz 11 %

XLTRC^2 used to predict lateral natural frequencies and damping ratios

APPENDIX C –

Sensor specification and analog output signal designation for DAQ of hybrid thrust bearing test rig

Table 12: DAQ analog input pin designation for the NI PCI 6225 static DAQ card with two SCB-28 terminal blocks

Analog Signals to DAQ		
AI #	**Type of Sensor**	**Signal Designation**
0	Shaker load control	Load output
1	Proximity probe	Probe 1: Test Thrust Bearing (TTB) Z1
2	Proximity probe	Probe 2: TTB Z2
3	Proximity probe	Probe 3: TTB Z3
4	Proximity probe	Probe 5: Rotor Thrust End Collar Y
5	Proximity probe	Probe 6: Rotor Thrust End Collar X
6	Proximity probe	Probe 7: Rotor Drive End Collar X
7	Proximity probe	Probe 8: Rotor Drive End Collar Y
8	Pressure transducer	Journal Bearing (JB) Drive End
9	Pressure transducer	JB Free End
10	Pressure transducer	Inlet TTB
11	Flowmeter	Inlet TTB
12	Flowmeter	Inlet Two JBs
13	Flowmeter	Inlet Slave Thrust Bearing (STB)
14	Flowmeter	Discharge TTB
15	Proximity probe	Probe 4: STB Zslave
16	Pressure transducer	TTB Pocket 1
17	Pressure transducer	TTB Land 2
18	Pressure transducer	TTB Pocket 3
19	Pressure transducer	TTB Land 4
20	Thermocouple	TTB Outer Radius Flow
21	Thermocouple	TTB Inner Radius Flow
22	Thermocouple	STB Inlet Flow
23	Thermocouple	JB Inlet Flow
24	Thermocouple	TTB Inlet Flow
25	Pressure transducer	Air Bearing 1
26	Pressure transducer	Air Bearing 2
27	Pressure transducer	Inlet Top STB
28	Pressure transducer	Inlet Bottom STB
29	Proximity probe	Probe 9: STB Zslave
30	Proximity probe	Probe 10: STB Zslave
31	Tachometer	Rotor Speed
32	Thermocouple	Coupling Temp
33	Load Cell Analog	Torque Measurement

Table 13: Instrumentation specifications and analog output signal DAQ designation

Northrop Grumman Hybrid Thrust Bearing Test Rig: Sensor Specification and Designation

Sensor Type	S/N	Designation	Manufacture Gain	Calibration Gain	Output Range	Digital Display (S/N)
	55507	Test Thrust Bearing (TTB) Pocket 1	60.06 PSIG/V	59.93 PSIG/V	0-5 VDC	6340608
Omega Pressure	57373	TTB Land 2	59.98 PSIG/V	59.97 PSIG/V	0-5 VDC	6340598
Transducer:	57369	TTB Pocket 3	60.06 PSIG/V	60.24 PSIG/V	0-5 VDC	6400512
PX209-300G5V	66409	TTB Land 4	60.06 PSIG/V	60.01 PSIG/V	0-5 VDC	6340594
"	57375	Journal Bearing (JB) Drive End	60.12 PSIG/V	59.97 PSIG/V	0-5 VDC	6340602
"	57368	JB Free End	59.95 PSIG/V	59.83 PSIG/V	0-5 VDC	6340610
"	57374	Inlet TTB	59.99 PSIG/V	60.14 PSIG/V	0-5 VDC	6400508
"	66397	Inlet Top Slave Thrust Bearing	59.91 PSIG/V	59.8 PSIG/V	0-5 VDC	n/a
"	66408	Inlet Bottom Slave Thrust Bearing	60.07 PSIG/V	60.14 PSIG/V	0-5 VDC	n/a
PX209-300G5V	55074	Air Bearing 1	n/a	41.93 PSIG/V	0-5 VDC	n/a
"	58228	Air Bearing 2	40.01 PSIG/V	40.14 PSIG/V	0-5 VDC	n/a
Flow Technology						
Flowmeters:						**(BR30-5-C-4)**
FT-12NEXW-LEG-2	12013009	Inlet TTB	5.914 GPM/V	3.16 GPM/V (2.06=b)	2.04-10 VDC	BR0610064
FT-10NEXW-LEG-2	1006280	Inlet Two JBs	7.27 GPM/V	1.84 GPM/V (2.04=b)	2.04-10 VDC	BR0610063
FT-12NEXB-LEA-2	1206544	Inlet Slave Thrust Bearing (STB)	1.59 GPM/V	n/a	2.04-10 VDC	BR07040087
FT8-8NEXW-LEG-2	8013596	Discharge TTB	2.23 GPM/V	.93 GPM/V (2.06=b)	2.04-10 VDC	BR06100162
Thermocouple						
K type wire	n/a	TTB Outer Radius Flow	n/a	18 F°/V	0-10 VDC	6300901
K type wire	n/a	TTB Inner Radius Flow	n/a	18 F°/V	0-10 VDC	6300893
K type wire	n/a	STB Inlet Flow	n/a	18 F°/V	0-10 VDC	6310211
K type wire	n/a	JB Inlet Flow	n/a	18 F°/V	0-10 VDC	6360141
K type wire	n/a	TTB Inlet Flow	n/a	18 F°/V	0-10 VDC	6360138

Sensor Type	S/N	Designation	Manufacture Gain	Calibration Gain	DC Offset	619M Encore Channel	Driver S/N
	61112 05	Probe 1: TTB Z1	.2 V/mil	0.2522 V/mil	~	1: top rack	17568
SKF Proximity Probes:	61119 15	Probe 2: TTB Z2	.2 V/mil	0.2545 V/mil	~	2: top rack	17571
CMSS65-002-00-12-10	61112 04	Probe 3: TTB Z3	.2 V/mil	0.2573 V/mil	~	3: top rack	17565
	61102 05	Probe 4: STB Zslave	.2 V/mil	0.2482 V/mil	~	4: top rack	17566
	61111 09	Probe 5: Rotor Thrust End Collar Y	.2 V/mil	0.2523 V/mil	~	1: bottom rack	17567
	61111 06	Probe 6: Rotor Thrust End Collar X	.2 V/mil	0.2546 V/mil	~	2: bottom rack	17562
	61111 10	Probe 7: Rotor Drive End Collar X	.2 V/mil	0.2422 V/mil	~	3: bottom rack	17563
	61111 01	Probe 8: Rotor Drive End Collar Y	.2 V/mil	0.2592 V/mil	~	4: bottom rack	17569
	61102 04	Probe 9: STB Z2	.2 V/mil	0.2487 V/mil	~	5: top rack	17564
	61102 01	Probe 10: STB Z3	.2 V/mil	0.249 V/mil	~	6: top rack	17570

Table 14: Instrumentation and accessories used

Item description		Manufacturer's part number		Desired range	Sensor range	Power requirements	Output	Resolution
Vendor - SKF								
Drivers	CMSS 65 5mm Probe	CMSS 65-002-00-12-10	Test thrust bearing probe system driver	1-20 mil	10-90 mil	-24V at 15mA	0 to -18V	200 mV/mil
	CMSS 65 5mm Probe	CMSS 65-002-00-25-10	Radial probe system driver	6 mil	10-90 mil	-24V at 15mA	0 to -18V	201 mV/mil
Proximity Probes	CMSS 65 sensor	CMSS 665	Sensors for the drivers					
Extension Cables	4 meter extension cable		Extension cables for proximity probe system					
Vendor - FTI								
	FT-10	FT-10NEXW-LEG-2	Radial bearing inlet flow meter	8-15 GPM	0.3-15 GPM			
	FT8-8	FT8-8NEXW-LEG-2	Test bearing inner radius discharge flow meter	0-4.75 GPM	0.16-7.5 GPM			
	FT-12	FT-12NEXW-LEG-2	Test bearing inlet flow meter	0.27-13.45 GPM	0.25-20 GPM			
Digital Indicator	FTI Linear Link	BR30-2-C-4	Linearizes and outputs flowmeter reading ****All Flowmeters require one			24V at 300mW	4-20 mA	±0.1% of reading
Vendor - Omega								
Pressure Transducer	Omega PX209 Pressure Transducer	PX209-300G5V	Test thrust bearing lands/pocket pressure tranducers	0-250psi	0-300 psi	24V at 15mA		0.75 psi
	Omega PX209 Pressure Transducer	PX209-300G5V	Test thrust bearing inlet pressure transducer	0-250psi	0-300 psi	24V at 15mA		0.75 psi
	Omega PX209 Pressure Transducer	PX209-300G5V	Journal bearing inlet pressure transducer	0-250psi	0-300 psi	24V at 15mA		0.75 psi
Transducer Displays	Signal display and output	DP25B-E-A	Displays for pressure transducers			120Vac	± 5V	0.02% of reading
	Signal display and output (Thermocouples)	DP25B-TC-A	Displays for thermocouples			120Vac	± 5V	0.5° C
Thermocouple wire	100 ft, Polyvinyl, 24 AWG, Type K	PR-K-24-100	Wire for thermocouples on outer and inner test thrust bearing radius					
Vendor - ENCORE								
Amplifier	Proximity sensor amplifier	Encore Model 619M-002				-24V to 24V		
Rack w/ Power Supply	Rack and power supply for amplifiers	Encore Model 4015-124				120Vac	-24V to 24V	

APPENDIX D –

Details of instrumentation description and calibration procedures

Forsberg [1] prepared the following excerpt:

Four types of instrumentation were required for the non-rotating tests of the hydrostatic thrust bearing: eddy current proximity probes, thermocouples, pressure sensors, and flow meters. Seven proximity probes were used in the static testing configuration. The probe locations are shown in Figure 83.

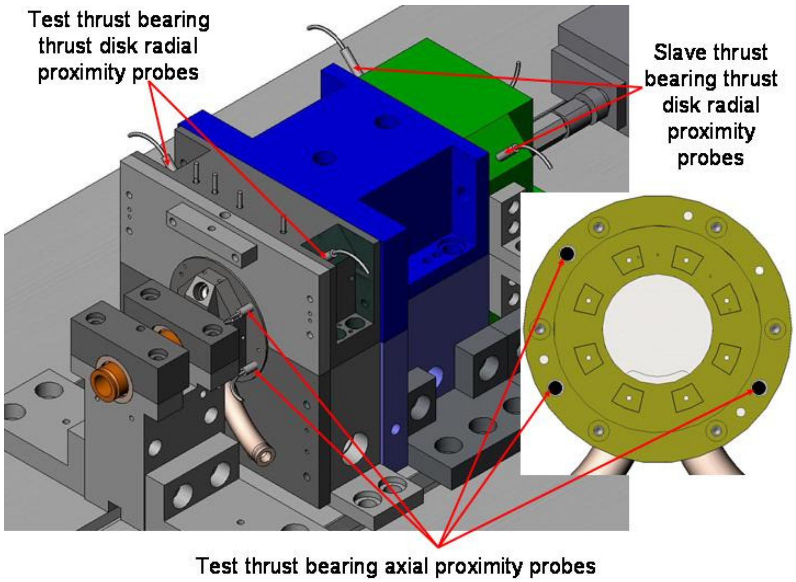

Figure 83: Locations of eddy current proximity probes during non-rotating tests

These proximity probes are used to monitor the rotor position. Two probes are dedicated to monitoring each of the rotor ends' radial position to insure rotor lift off. These probes will also be used during tests with rotor rotation to monitor the rotor radial motions. The remaining three probes are used to monitor the axial position of the test thrust bearing relative to the test bearing thrust disk. Three proximity probes in this application define the thrust bearing face's position relative to the plane of the thrust disk. This capability means that the misalignment of the thrust disk relative to the bearing can be determined.

The proximity probe selected was the SKF CMSS-65 5mm system. This system uses a five millimeter diameter probe that attaches to a driver which outputs a voltage to the DAQ. The probe system requires a -24 V power source and outputs a signal from -2 to -20 V [30]. However, the DAQ card requires a signal to be within the ±10 V range

[21]. To correct this discrepancy, Encore model 619M signal conditioners were used to offset the signal and attenuate it if necessary.

Each proximity probe was calibrated in the same configuration used during testing, including extension cable, probe, and driver. Calibration also used the rotor, the intended probe target, to develop the output curve to assure that the inconel composition did not cause measurement error. Measurements were made of the output voltage from the driver with a digital voltmeter and the probe distance from the rotor using a dial gauge. These readings were then compiled to find the linear region of the probe with the rotor target and the equation of the line through the linear region. An example curve is shown in Figure 84. With the calibration curves, the linear region of the probes with inconel was found to be from 0.4 to 1.5 mm approximately, and the best fit line was found for each probe system.

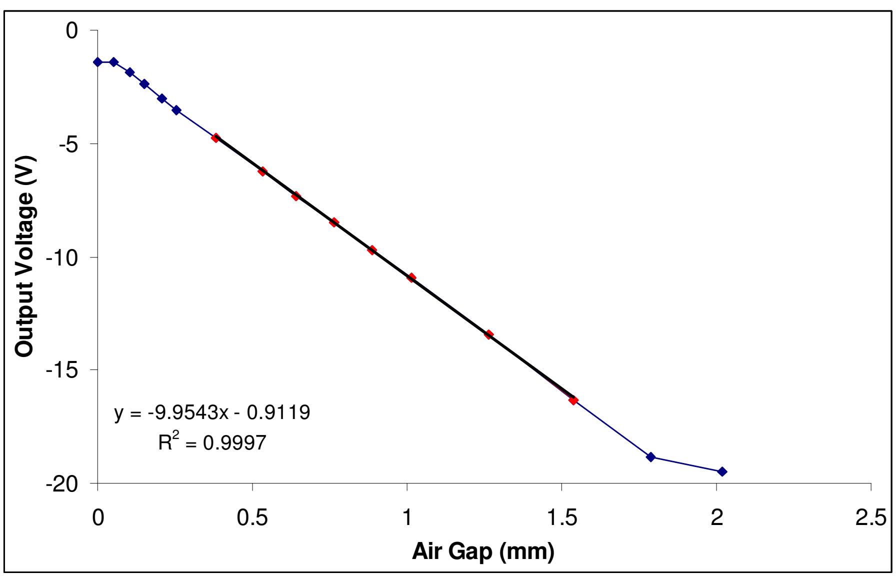

Figure 84: Example calibration curve for a proximity probe used on the hydrostatic thrust bearing test rig

Four thermocouples were also used. Two thermocouples measured the inlet flow to the test thrust bearing and the journal bearings. Plug style type K thermocouples were used to prevent failure at maximum operating pressure. The other two thermocouples were mounted to the inner and outer radius of the test thrust bearing as seen in Figure 85.

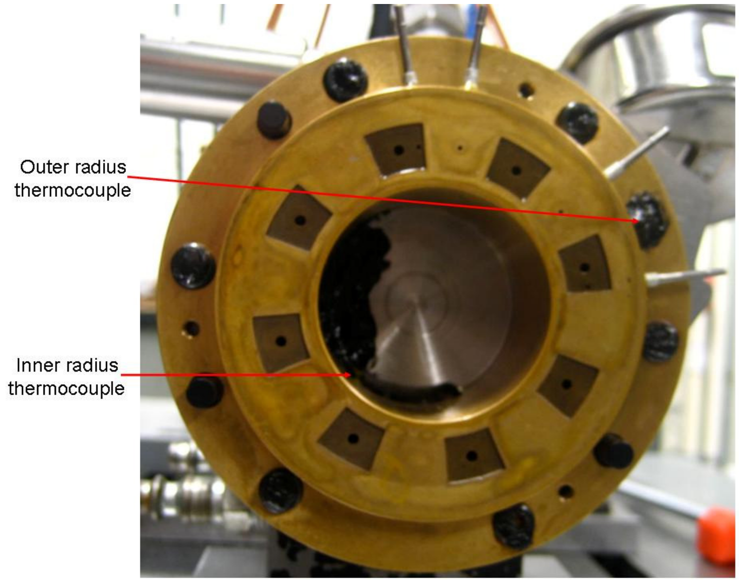

Figure 85: Locations of the inner and outer radius thermocouples on the test thrust bearing

These two thermocouples are type K and are secured in place with silicone to measure the temperature of the flow from the outer radius and inner radius of the test thrust bearing. All four thermocouples are wired to Omega DP25B displays and were calibrated with the displays using an ice-water and a boiling-water bath. The displays output a 0 to 5 V signal to the DAQ. An additional plug type thermocouple is also installed in the water supply piping to monitor the inlet supply temperature of the slave thrust bearing for testing with rotor rotation.

Seven pressure sensors were used in non-rotating testing. Figure 86 shows three of these pressure sensors used to monitor the inlet pressures to the test thrust bearing and each of the radial bearings.

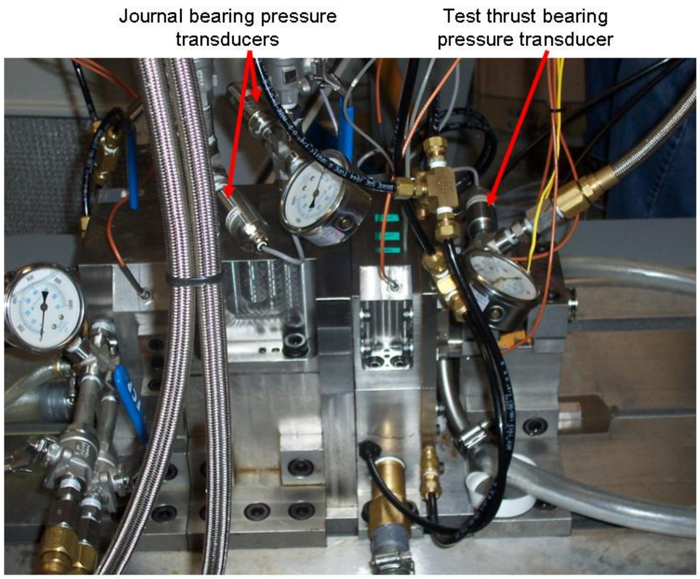

Figure 86: Inlet pressure sensors for journal bearings and test thrust bearing

As shown, the test thrust bearing supply pressure sensor was mounted as near as possible to the bearing to provide representative pressure readings. Additionally, the two journal-bearing supply-pressure sensors are used to confirm that both bearings are operating at nearly identical pressures. Two additional pressure transducers are added to monitor the slave thrust bearing for rotational testing. The remaining four pressure sensors are used to measure the pressures in two of the pockets and at two locations on the lands. Figure 87 shows the pressure tap positions.

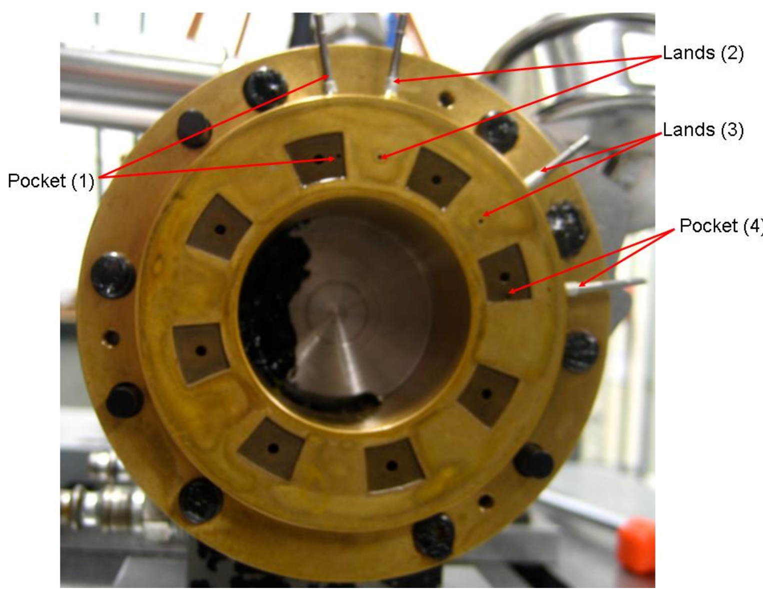

Figure 87: Location of pressure taps for on bearing pressure measurement

The taps in the bearing face intersect with a perpendicular hole which leads to the edge of the bearing. From there, the taps are hooked into their respective static pressure transducers by way of flexible tubing. Each pressure transducer was calibrated with its respective DP-25 display using a dead-weight tester over the range of 0 to 20.7 bar. The analog output from each DP-25 display was then routed to the DAQ.

Finally, three flow meters were used during testing. These flow meters were used to monitor the inlet flow to the journal bearings and the test thrust bearing in addition to the exhaust flow from the inner radius of the test thrust bearing. The location of the flow meters can be found in the flow schematic in Appendix A. All of the flow meter outputs were wired to signal linearizers with output displays. Outputs from the linearizers were then wired into the DAQ.

APPENDIX E –

Test thrust bearing rotor thrust disk plane equation derivation

The following excerpt prepared by Forsberg [1]:

Determining the position and orientation of the thrust disk relative to the test thrust bearing is critical. The output of three eddy current probes is available for this task. The layout geometry of the probes is known as seen in Figure 88.

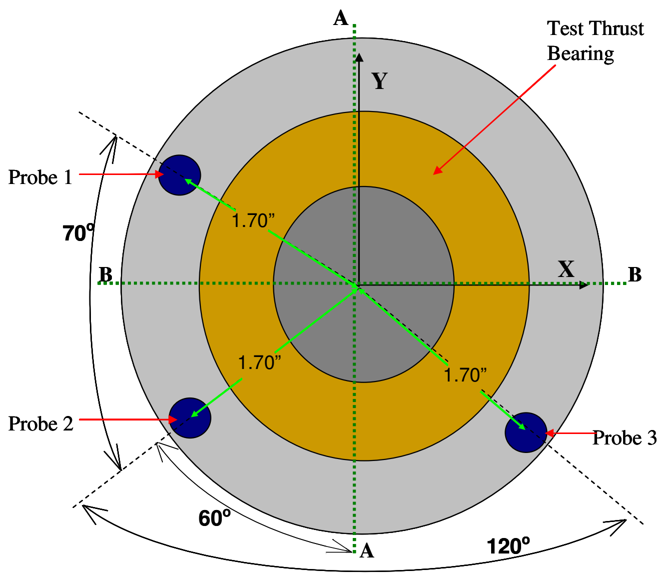

Figure 88: Layout geometry of eddy current sensors on test thrust bearing support

From this diagram, the horizontal and vertical positions of each probe relative to the center of the bearing are calculated. These positions are shown in Table 15.

Table 15: Vertical and horizontal positions of proximity probes on thrust bearing support from bearing center

	X	Y
Probe 1	-33.02 mm (-1.30 in)	27.69 mm (1.09 in)
Probe 2	-37.34 mm (-1.47 in)	-21.59 mm (-0.85 in)
Probe 3	37.34 mm (1.47 in)	-21.59 mm (-0.85 in)

The equation for the plane of the rotor thrust disk relative to the thrust bearing face can now be found. Both the thrust bearing face and the rotor thrust disk are assumed to be rigid flat planes. The three proximity probe outputs are used to identify three points on the plane of the thrust disk as shown in Figure 89.

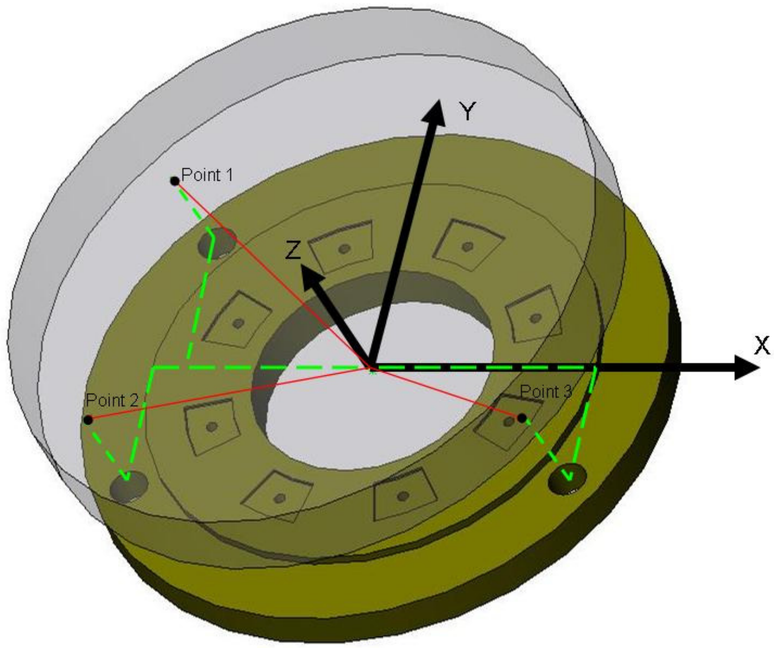

Figure 89: Depiction of the three points measured with the proximity probes on the test thrust bearing thrust disk face.

These three points on the thrust disk are further defined in Table 16.

Table 16: Coordinates of the three proximity probe points

	Point Coordinates (x,y,z)
Point 1	(-33.02, 27.69, Z_1) mm (-1.30, 1.09, Z_1) in
Point 2	(-37.34, -21.59, Z_2) mm (-1.47, -0.85, Z_2) in
Point 3	(37.34, -21.59, Z_3) mm (1.47, -0.85, Z_3) in

These three points can next be used to generate two vectors located on the surface of the plane. Equation (2.1) and (2.2) show these two vectors.

$$\vec{v}_{12} = \text{Point 2 - Point 1} = <\text{-4.32, -49.28, } Z_2 - Z_1 > \text{ mm} \qquad \textbf{(2.1)}$$

$$\vec{v}_{13} = \text{Point 3 - Point 1} = <\text{70.36, -49.28, } Z_3 - Z_1 > \text{ mm} \qquad \textbf{(2.2)}$$

Where

$\vec{\mathbf{V}}_{12}$ = Vector from point 1 to point 2 in the thrust disk plane

$\vec{\mathbf{V}}_{13}$ = Vector from point 1 to point 3 in the thrust disk plane

Z_1, Z_2, Z_3 = Z coordinate of probe 1, 2, or 3

The two generated vectors can next be used to create a vector normal to the plane by taking the cross product of the two vectors.

$$\vec{\mathbf{N}} = \vec{\mathbf{V}}_{12} \mathbf{\ x\ } \vec{\mathbf{V}}_{13}$$

$$\vec{\mathbf{N}} =< 49.28(Z_2 - Z_3),\ -74.68Z_1 + 70.36Z_2 + 4.32Z_3,\ 144.87 > \text{ mm} \qquad \textbf{(2.3)}$$

Where

$\vec{N}$ = Normal vector to the thrust disk plane

A generic vector must now be generated from the first point and a generic point located on the plane of the thrust disk (*x,y,z*). Equation (2.4) shows the formula for this point.

$$\vec{\mathbf{V}}_{\mathbf{generic}} = \text{Generic Point- Point 1} = < \text{x+33.02, y-27.69, z} - Z_1 > \text{ mm} \qquad \textbf{(2.4)}$$

Where

$\vec{\mathbf{V}}_{\mathbf{generic}}$ = Vector from point 1 to a generic point (x,y,z) in the thrust disk plane

Finally, by taking the dot product of the normal vector and the generic vector the equation of the thrust disk plane can be determined.

$$\vec{\mathbf{N}} \bullet \vec{\mathbf{V}}_{\mathbf{generic}} = 0$$

$$49.3(Z_2 - Z_3)x + (-74.7Z_1 + 70.4Z_2 + 4.3Z_1)y + 144.8z + (-63.5Z_1 - 12.7Z_2 - 68.8Z_3) = 0 \qquad \textbf{(2.5)}$$

This equation can ultimately be reduced to the more useful, final form.

$$Z(x,y) = M_1 x + M_2 y + Z_c$$

$$Z(x,y) = 8.6(Z_3 - Z_2)x + (13.1Z_1 - 12.3Z_2 - 0.76Z_3)y + (11.1Z_1 + 2.2Z_2 + 12.1Z_3) \qquad \textbf{(2.6)}$$

Where

M_1 = Slope of the thrust disk plane in the X-axis

M_2 = Slope of the thrust disk plane in the Y-axis

Z_c = Clearance at the center of the test thrust bearing

APPENDIX F –

Slave thrust bearing rotor thrust disk plane equation derivation

The position and orientation of the thrust disks relative to the test and slave thrust bearing is critical. Forsberg [1] provides an evaluation for the position and orientation of the test thrust collar relative to the test thrust bearing. The following includes the subsequent evaluation for the position and orientation of the slave thrust collar relative to the slave thrust bearing. The output of three eddy current probes for each thrust bearing is available for the position assessment. The layout geometry of the probes for the slave thrust bearing is shown in Figure 90.

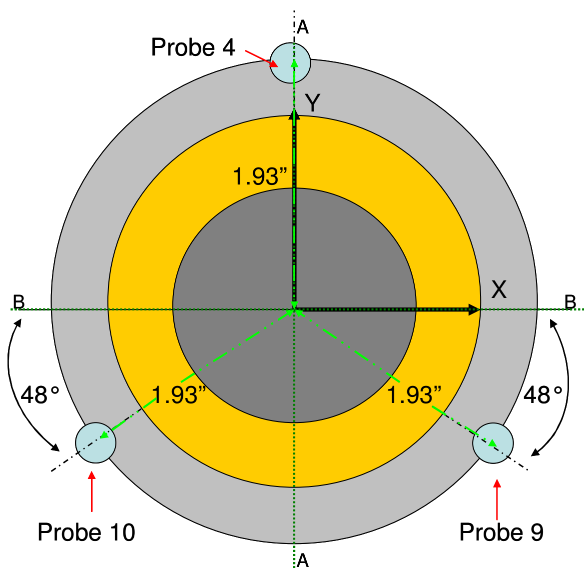

Figure 90: Layout geometry of eddy current sensors on the slave thrust bearing support

The horizontal and vertical positions of each probe relative to the center of the bearing are calculated. The positions on the x-y coordinate system are shown in Table 17.

Table 17: Vertical and horizontal positions of proximity probes on slave thrust bearing support from bearing center

	X	Y
Probe 4	0 mm	49.02 mm (1.93 in)
Probe 10	-32.77 mm (-1.29 in)	-36.46 mm (-1.44 in)
Probe 9	32.77 mm (1.29 in)	-36.46 mm (-1.44 in)

The equation for the plane of the rotor thrust disk relative to the slave thrust bearing face can now be found. Both the thrust bearing face and the rotor thrust disk are

assumed to be rigid flat planes. The three proximity probe outputs are used to identify three points on the plane of the thrust disk as shown in Figure 91.

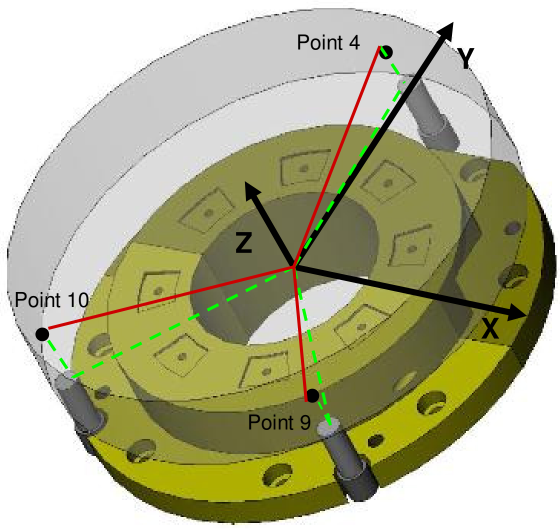

Figure 91: Depiction of the three points measured with the proximity probes on the test thrust bearing thrust disk face

These three points on the thrust disk are further defined in Table 18.

Table 18: Coordinates of the three proximity probe points

	Point Coordinates (x,y,z)	
Probe 4	(0, 49.02, Z_4) mm	(0, 1.93, Z_4) in
Probe 10	(-32.77, -36.46, Z_{10}) mm	(-1.29, -1.44, Z_{10}) in
Probe 9	(32.77, -36.46, Z_9) mm	(1.29, -1.44, Z_9) in

These three points can next be used to generate two vectors located on the surface of the plane. Equation (3.1) and (3.2) show these two vectors.

$$\vec{V}_{410} = \text{Point 10 - Point 4} = \langle -32.77, 85.45, Z_{10} - Z_4 \rangle \text{ mm} \qquad \textbf{(3.1)}$$

$$\vec{V}_{49} = \text{Point 9 - Point 4} = \langle 32.77, -85.45, Z_9 - Z_4 \rangle \text{ mm} \qquad \textbf{(3.2)}$$

Where

$\vec{V}_{410}$ = Vector from point 4 to point 10 in the thrust disk plane

$\vec{V}_{49}$ = Vector from point 4 to point 9 in the thrust disk plane

Z_4, Z_9, Z_{10} = Z coordinate of probe 4, 9, or 10

The two generated vectors are used to create a vector normal to the plane by taking the cross product of the two vectors.

$$\vec{\mathrm{N}} = \vec{V}_{410} \text{ x } \vec{V}_{49}$$
$$\vec{\mathrm{N}} = <85.45(\mathrm{Z}_{10} \text{ -Z}_9),\ \text{-}65.53\mathrm{Z}_4 + 32.77\mathrm{Z}_{10} + 32.77\mathrm{Z}_9,\ 220.55> \text{ mm} \quad \textbf{(3.3)}$$

Where

$\vec{\mathrm{N}}$ = Normal vector to the thrust disk plane

A generic vector is generated from the first point and a generic point located on the plane of the thrust disk (*x,y,z*). Equation (3.4) shows the formula for this point.

$$\vec{V}_{generic} = \text{Generic Point - Point 4} = <\text{x, y+32.77, z- } \mathrm{Z}_4 > \text{mm} \quad \textbf{(3.4)}$$

Where

$\vec{V}_{generic}$ = Vector from point 4 to a gneric point (x,y,z) in the thrust disk plane

Finally, by taking the dot product of the normal vector and the generic vector the equation of the thrust disk plane can be determined.

$$\vec{\mathrm{N}} \cdot \vec{V}_{generic} = 0$$
$$85.45(\mathrm{Z}_{10} - \mathrm{Z}_9)x + (-65.53\mathrm{Z}_4 + 32.77\mathrm{Z}_{10} + 32.77\mathrm{Z}_9)y + 220.55z \ ... \quad \textbf{(3.5)}$$
$$... +(-12\mathrm{Z}_4 + 42.27\mathrm{Z}_{10} + 42.27\mathrm{Z}_9) = 0$$

This equation can ultimately be reduced to the more useful, final form.

$$Z(x,y) = M_{1slave}x + M_{2slave} + Z_{cslave} \quad \textbf{(3.6)}$$
$$Z(x,y) = 9.85(\mathrm{Z}_9 - \mathrm{Z}_{10})x + (7.55\mathrm{Z}_4 - 3.77\mathrm{Z}_{10} - 3.77\mathrm{Z}_9)y \ ...$$
$$... + (35.11\mathrm{Z}_4 - 4.87\mathrm{Z}_{10} - 4.87\mathrm{Z}_9) = 0$$

Where

M_{1slave} = Slope of the thrust disk plane in the X-axis

M_{2slave} = Slope of the thrust disk plane in the Y-axis

Z_{cslave} = Clearance at the center of the slave thrust bearing

APPENDIX G –

Thrust bearing misalignment about the x and y axis versus center clearance

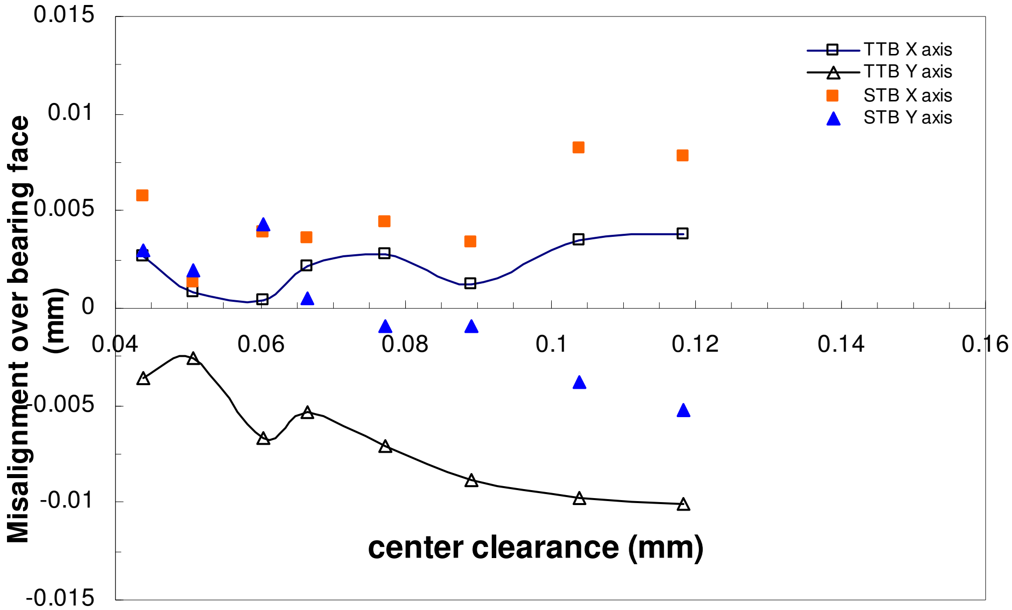

Figure 92: Test and slave thrust bearing face misalignment about the x and y axis versus load (3.45 bar, 7.5 krpm test case)

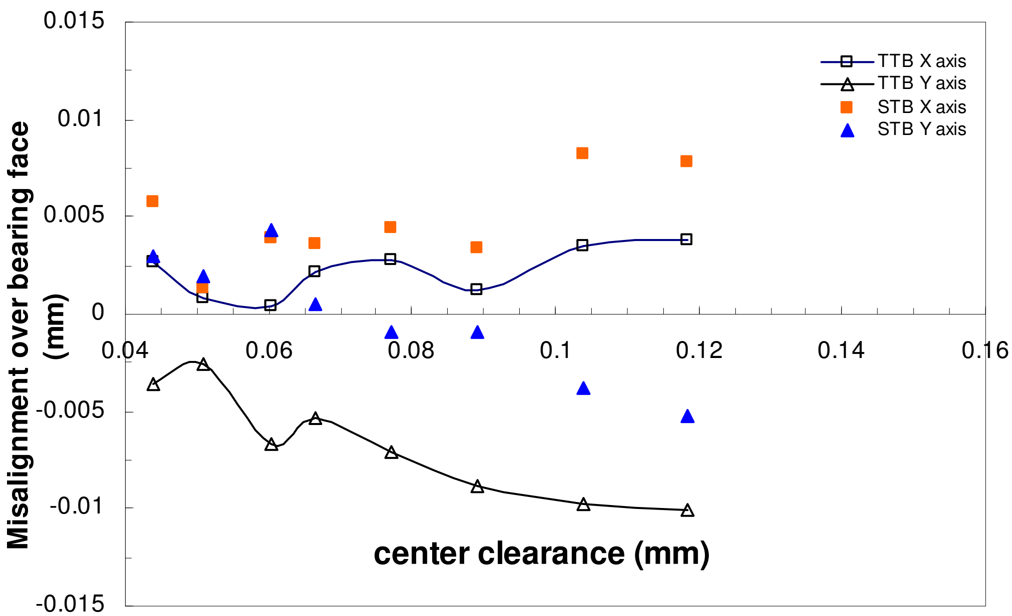

Figure 93: Test and slave thrust bearing face misalignment about the x and y axis versus load (3.45 bar, 12.5 krpm test case)

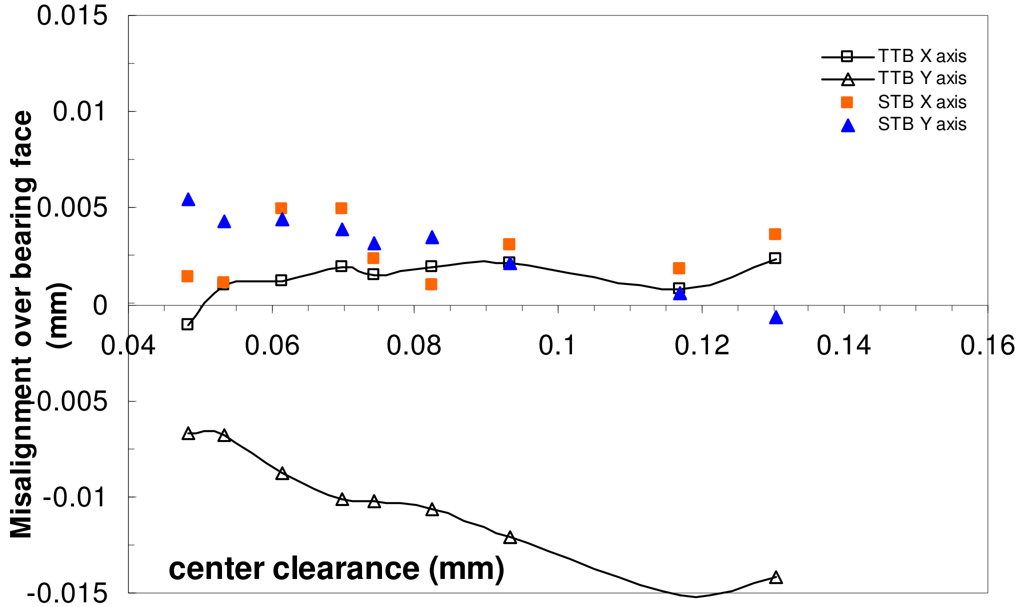

Figure 94: Test and slave thrust bearing face misalignment about the x and y axis versus load (3.45 bar, 17.5 krpm test case)

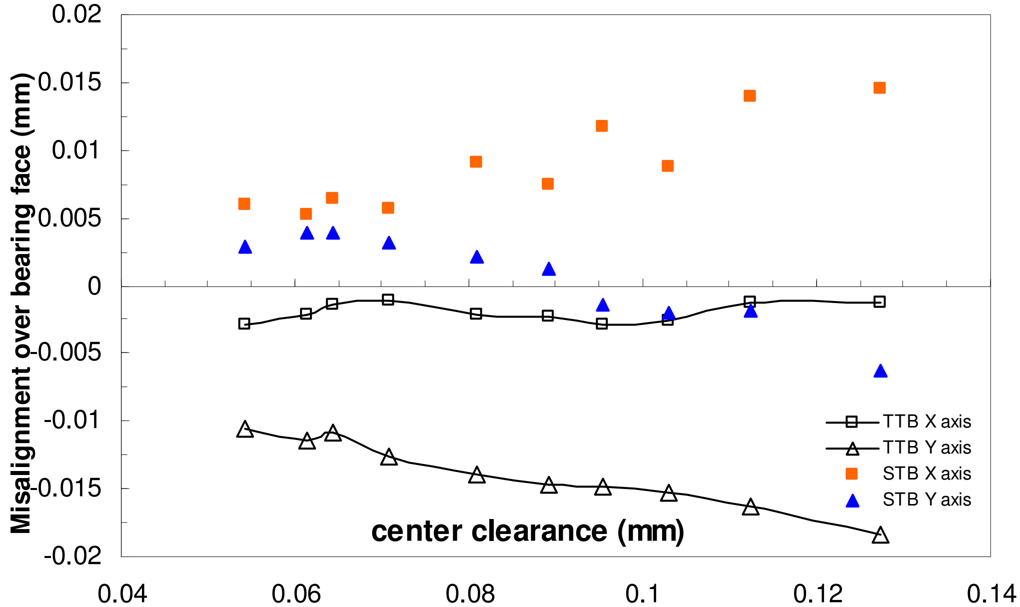

Figure 95: Test and slave thrust bearing face misalignment about the x and y axis versus load (10.34 bar, 7.5 krpm test case)

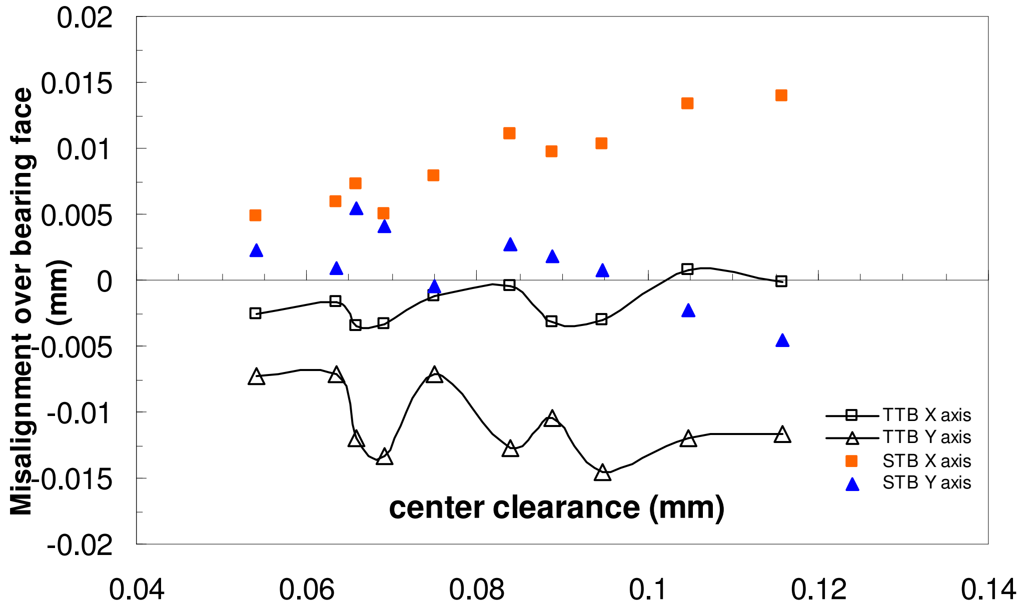

Figure 96: Test and slave thrust bearing face misalignment about the x and y axis versus load (10.34 bar, 12.5 krpm test case)

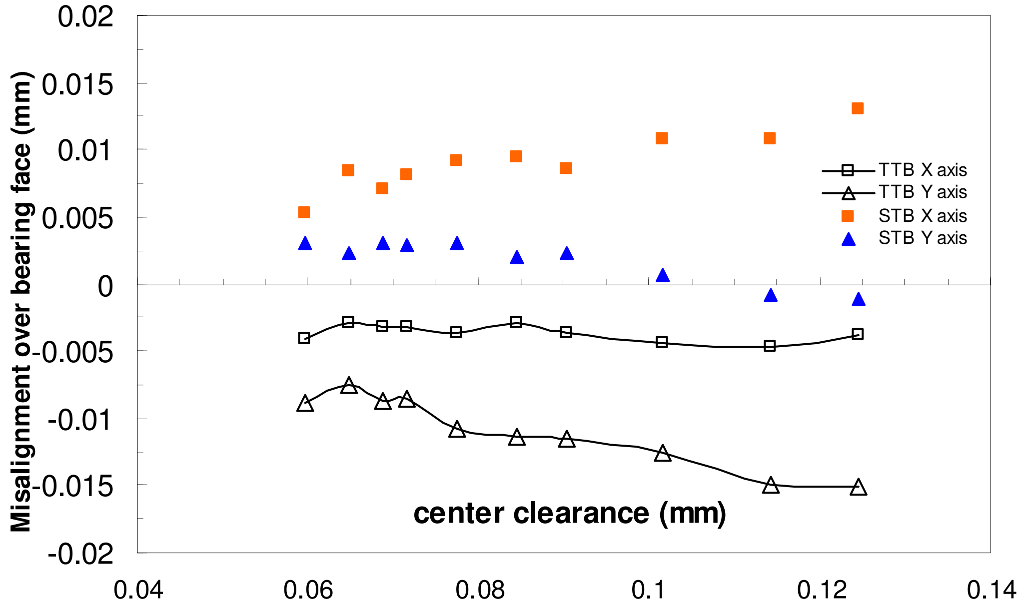

Figure 97: Test and slave thrust bearing face misalignment about the x and y axis versus load (10.34 bar, 17.5 krpm test case)

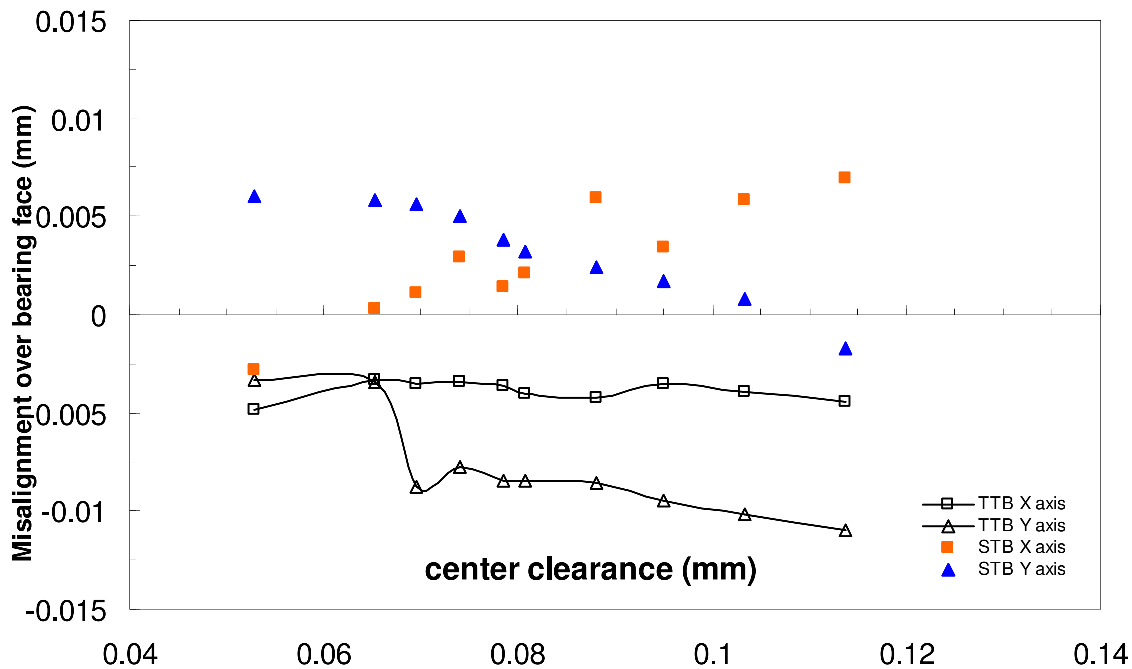

Figure 98: Test and slave thrust bearing face misalignment about the x and y axis versus load (17.24 bar, 7.5 krpm test case)

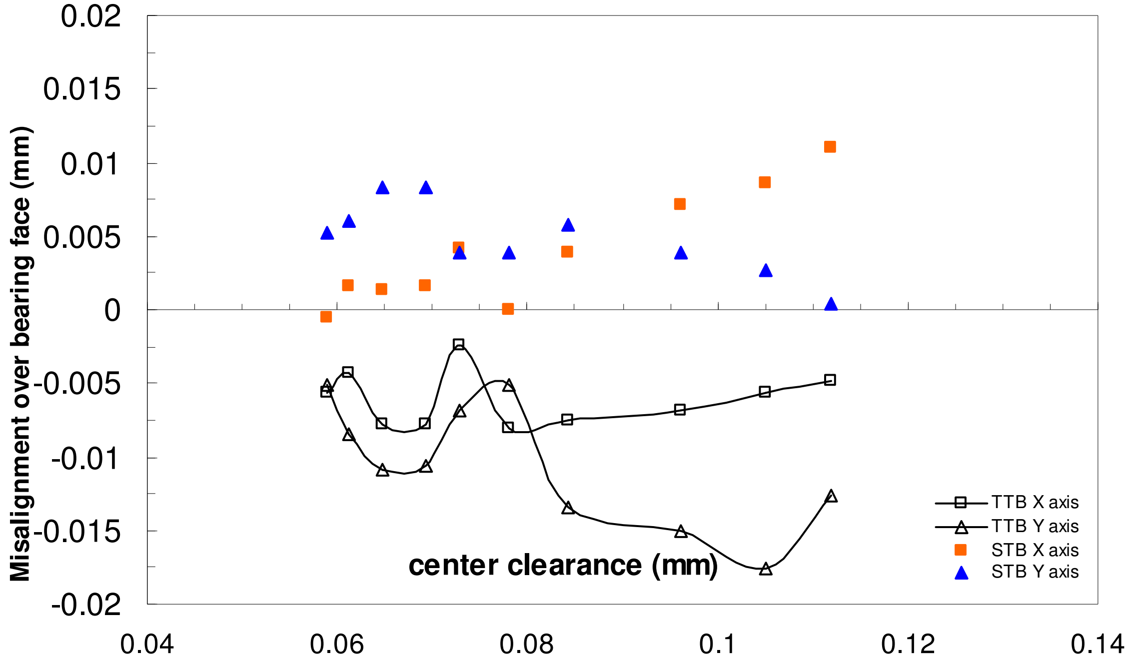

Figure 99: Test and slave thrust bearing face misalignment about the x and y axis versus load (17.24 bar, 12.5 krpm test case)

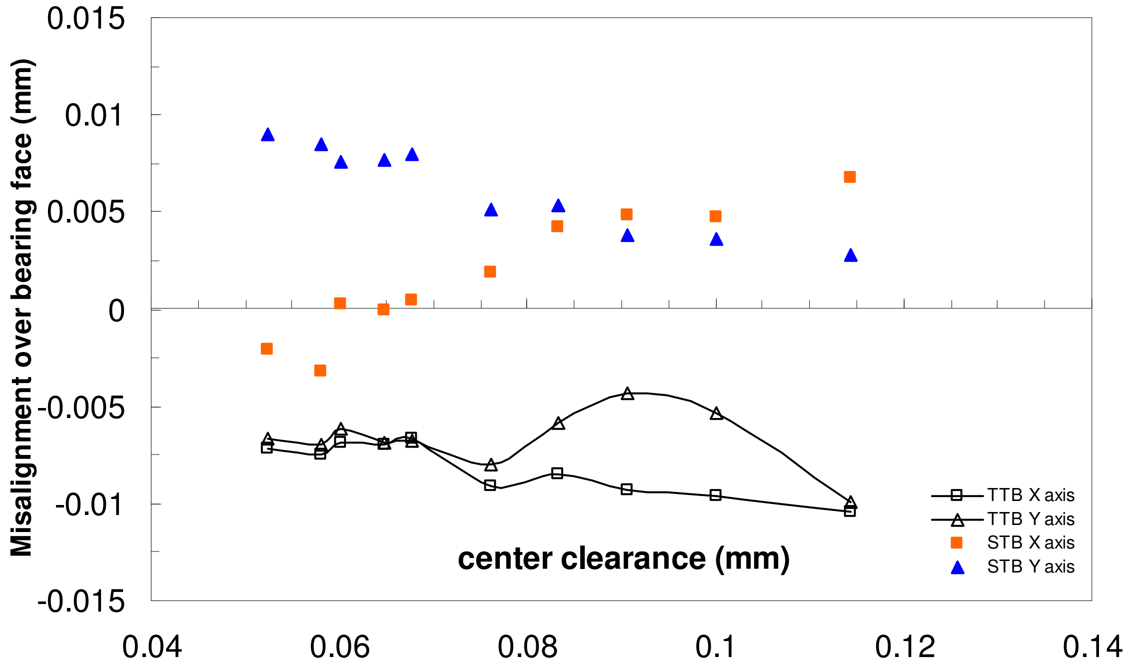

Figure 100: Test and slave thrust bearing face misalignment about the x and y axis versus load (17.24 bar, 17.5 krpm test case)

APPENDIX H –

Uncertainty analysis of measurements

The error estimation to validate the experimental investigation was conducted utilizing the format of Forsberg's [1] uncertainty analysis. Errors can come from two sources (bias and precision). In this analysis, bias error is considered negligible and precision error is assumed to be the major error source. The precision error can come from several sources and must be propagated appropriately. To combine these errors Equation (4.1) [31] is used.

$$E_N = \left[\Sigma\left(\frac{dF(X_1, X_2, ..., X_N)}{dX_N} * E_{XN}\right)^2 \right]^{1/2} \quad \textbf{(4.1)}$$

With this equation, so long as the function and individual variable errors are known, the overall error can be estimated. The measurement uncertainty (σ) can also be included into Equation (4.1) as one half of a summed squared term. Most of these individual errors are known from the error of the instrumentation; however, to determine the error from the calibration of the instrumentation Equation (4.2) [31] must be introduced,

$$SEE = \left[\frac{\Sigma[Y_i - (aX_i - b)]^2}{M - 2} \right]^{1/2} \quad \textbf{(4.2)}$$

to determine the standard error of estimation (SEE). The SEE can then be used similarly to determine standard deviation of the error associated with a given curve fit parameter. The error derived from the SEE that is associated with a given variable is 2*SEE. This error band to either side of the calculated value will include approximately 95% of the possible points. With these two equations the errors of the experimental measurements are defined.

Equation (4.3) was used to define the flow rate.

$$FlowRate = A_{FlowMeter} * V - B_{FlowMeter} \quad \textbf{(4.3)}$$

Where

$A_{FlowMeter} =$ Linear calibration constant of the flow meter

$B_{FlowMeter} =$ Flow meter calibration offset

$V =$ Flow meter output voltage

This equation can then be used with Equation (4.1) to find the expression for overall error.

$$E_{Flowrate} = \sqrt{(V * E_{AFlowMeter})^2 + (A_{FlowMeter} * E_V)^2 + (2 * \sigma_{Flow})^2} \quad \textbf{(4.4)}$$

Where

$E_{FlowMeter} =$ Flow meter error

$E_{AFlowMeter} =$ Error of $A_{FlowMeter}$ term

$E_V =$ Error of flow meter voltage measurment

$\sigma_{Flow} =$ Standard deviation of flow meter reading

This process can be repeated to find the error associated with the load measurement from

$$Load = A_{LoadCell} * V - B_{LoadCell} \quad \textbf{(4.5)}$$

Where

$A_{LoadCell} =$ Linear calibration constant of the load cell

$B_{LoadCell} =$ Load cell calibration offset

$V =$ Load cell output voltage

Applying Equation (4.1) to Equation (4.5) the error expression is

$$E_{Load} = \sqrt{(A_{Load} * E_V)^2 + (2 * \sigma_{Load})^2} \quad \textbf{(4.6)}$$

Where

$E_{Load} =$ Load cell error

$E_V =$ Error of load cell voltage measurment

$\sigma_{Load} =$ Standard deviation of flow meter reading

Finally the error associated with the differentiation estimation of the stiffness can be determined using

$$E_{dF/dZ} = \sqrt{E_A^2 + E_B^2 + E_C^2} \quad \textbf{(4.7)}$$

Where

$Load = A * Z_C^3 + B * Z_C^2 + C * Z_C + D$

$E_N =$ Uncertainty associated with term N

$\mathrm{Z}_C =$ Test thrust bearing center clearance

This equation requires that the error from each term is known; hence, the TableCurve2D software was utilized. This software calculated the error from each of the terms in the polynomial curve fit load expression. These errors were then substituted into Equation (4.7).